PFG

Photogrammetrie Fernerkundung Geoinformation

Journal for Photogrammetry, Remote Sensing and Geoinformation Science

Organ der Deutschen Gesellschaft für Photogrammetrie, Fernerkundung und Geoinformation (DGPF) e. V.

Jahrgang 2013, Heft 3

E. Schweizerbart'sche Verlagsbuchhandlung
(Nägele u. Obermiller) Stuttgart 2013

Deutsche Gesellschaft für Photogrammetrie, Fernerkundung
und Geoinformation (DGPF) e.V.
Gegründet 1909

Die *Deutsche Gesellschaft für Photogrammetrie, Fernerkundung und Geoinformation* (DGPF) e.V. unterstützt als Mitglieds- bzw. Trägergesellschaft die folgenden Dachverbände:

International Society
for Photogrammetry
and Remote Sensing

Deutsche Arbeits-
gemeinschaft für
Mustererkennung e.V.

GeoUnion
Alfred-Wegener-Stiftung

Herausgeber:

Präsident: Prof. Dr. Thomas Kolbe, Technische Universität München, Institut für Geodäsie, GIS und Landmanagement, Lehrstuhl für Geoinformatik, Arcisstraße 21, 80333 München, Germany, Tel. +49-89-289-23888
Geschäftsstelle: Dr. Klaus-Ulrich Komp, c/o EFTAS Fernerkundung Technologietransfer GmbH, Oststraße 2–18, 48145 Münster, Germany, e-mail: klaus.komp@eftas.com
Published by: E. Schweizerbart'sche Verlagsbuchhandlung (Nägele u. Obermiller), Johannesstraße 3A, 70176 Stuttgart, Germany, Tel.: +49-711 351456-0, Fax: +49-711 351456-99, e-mail: mail@schweizerbart.de
Internet: http://www.schweizerbart.de
⊗ Gedruckt auf alterungsbeständigem Papier nach ISO 9706-1994

ISSN 1432-8364
Science Citation Index Expanded (also known as SciSearch®) Journal Citation Reports/Science Edition

Erscheinungsweise: 6 Hefte pro Jahrgang.
Bezugspreis im Abonnement: € 229,– pro Jahrgang. Mitglieder der DGPF erhalten die Zeitschrift kostenlos. Der Online-Zugang ist im regulären Subskriptionspreis enthalten.
Anzeigenverwaltung: E. Schweizerbart'sche Verlagsbuchhandlung (Nägele u. Obermiller), Johannesstraße 3A, 70176 Stuttgart, Germany, Tel.: +49-711 351456-0; Fax: +49-711 351456-99.
e-mail: mail@schweizerbart.de, Internet: http://www.schweizerbart.de
Bernhard Harzer Verlag GmbH, Westmarkstraße 59/59a, 76227 Karlsruhe, Germany, Tel.: +49-721 944020, Fax: +49-721 9440230, e-mail: Info@harzer.de, Internet: www.harzer.de
Printed in Germany by Tutte Druckerei & Verlagsservice GmbH, 94121 Salzweg, Germany.

PFG – Jahrgang 2013, Heft 3
Inhaltsverzeichnis

Editorial

Originalbeiträge

Beitrag aus Wissenschaft und Praxis

Mitteilungen

Zusammenfassungen der „Originalbeiträge“ und der „Beiträge aus Wissenschaft und Praxis“ (deutsch und englisch) sind auch verfügbar unter www.dgpf.de/neu/pfg/ausgaben.htm

PFG 2013 / 3, 0137
Stuttgart, June 2013

Editorial

Das vorliegende „Schwerpunktheft Fernerkundung“ wird zum größten Teil durch Beiträge der gemeinsamen Jahrestagung des Arbeitskreises „Fernerkundung“ der DGfG (Deutsche Gesellschaft für Geographie) und des Arbeitskreises „Auswertung von Fernerkundungsdaten“ der DGPF getragen. Die gemeinsame Jahrestagung wurde am 4. und 5. Oktober 2012 in Bochum unter dem Motto „Fernerkundung – Von der wissenschaftlichen Entwicklung zur Praxisreife“ durchgeführt (www.ak-fernerkundung.de). Der Arbeitskreis Fernerkundung hat sich zum Ziel gesetzt, eine Plattform der angewandten geographischen Fernerkundung insbesondere für den wissenschaftlichen Nachwuchs zu bieten. Das Treffen unter Leitung von Prof. Dr. Carsten Jürgens (Ruhr-Universität Bochum) konnte mit insgesamt etwa 70 Teilnehmern als Erfolg gewertet werden, denn es wurden durchweg aktuelle und forschungsorientierte Beiträge aus den verschiedenen Fernerkundungsstandorten geboten.

Die eingereichten Artikel zur Jahrestagung zeigten insgesamt eine sehr hohe Qualität. Eine Auswahl der Artikel wurde nach einem Reviewprozess für die Veröffentlichung in diesem Schwerpunktheft ausgesucht. Thematisch spannen die eingereichten Artikel nach dem Titel der Arbeitskreistagung, einen breiten Bogen von Themen zur Vegetationsanalyse, Desertifikation und Glaziologie bis zur urbanen Fernerkundung und zum Desaster Monitoring. Die Beiträge aus dem Arbeitskreis behandeln die Themen Habitatkartierung durch SAR-Daten, objektbasierte Klassifizierung urbaner Flächen, objektbasierte und GIS-gestützte Klassifizierung von Grünlandbiotopen, flugzeuggestütztes Laserscanning für ein Waldstrukturmonitoring und fernerkundungsgestützte Auswertung zur Unterstützung humanitärer Hilfe in Flüchtlingscamps.

Neben diesen fünf konnten drei weitere Beiträge gewonnen werden, die das aktuelle Heft thematisch bereichern. Sie decken die folgenden Themenfelder ab: ASTER DTMs für glaziologische Anwendungen in Argentinien, fraktalbasiertes Change Detection mit SAR-Daten und die Detektion und Klassifizierung von Objekten in Punktwolken unter Nutzung von semantischer Information.

Liebe Leser des „Schwerpunktheftes Fernerkundung“, wir hoffen Ihr Interesse geweckt zu haben und wünschen Ihnen viele Anregungen und neue Denkanstöße für Ihre Arbeit durch das Lesen des Heftes.

Carsten Jürgens, Bochum,
Ulrich Michel, Heidelberg
und Horst Weichelt, Brandenburg

 www.schweizerbart.de
DOI: 10.1127/1432-8364/2013/0164 1432-8364/13/0164 $ 0.25

PFG 2013 / 3, 0139–0148
Stuttgart, June 2013

Article

Habitat Mapping from Optical and SAR Satellite Data: Implications of Synergy and Uncertainty for Landscape Analysis

Stefan Erasmi, Göttingen

Keywords: habitat mapping, SAR data, RapidEye, accuracy assessment, landscape metrics

Summary: Satellite based habitat maps are the main source for the analysis of landscape pattern and its effect on species diversity and ecosystem functions. Nonetheless, only few studies systematically investigated the optimal constellation of multi-source satellite input data for habitat mapping and the effect of mapping accuracy on landscape pattern indices and hence on ecological analysis. The present study underlines the importance of a careful selection of input data for land cover type classification and highlights the synergistic potential of optical/SAR data fusion for habitat mapping purposes. With regard to landscape analysis the study reveals the impact of classification accuracy on variation in landscape metrics. This impact is not uniform and not always directly related to classification accuracy but is depending on the nature of landscape metrics. Area metrics show strong variations with the magnitude of variation being much higher than the classification errors whereas variation of diversity and connectivity measures is significantly below the classification error. Finally, it is demonstrated that spatial uncertainty in land cover maps has to be addressed in any landscape analysis at spatial scale.

Zusammenfassung: *Die Habitatkartierung aus Daten optischer und SAR-Satelliten: Synergieeffekte und Unsicherheiten bei der Analyse der Landschaft.* Die Analyse der Zusammenhänge zwischen Landschaftsmustern und Artenvielfalt bzw. Ökosystemfunktionen im Allgemeinen ist in vielen Fällen auf satellitenbasierte Habitatkartierungen gestützt. Hierbei wird aber nur in wenigen Fällen untersucht, welche Sensoren und Aufnahmezeitpunkte am besten geeignet sind. Darüber hinaus wird in den meisten Fällen nicht berücksichtigt, welche Auswirkungen die Klassifikationsgenauigkeit auf die Berechnung von Landschaftsmaßen und damit auf die Auswertung ökologischer Zusammenhänge haben kann. In diesem Zusammenhang hebt der vorliegende Beitrag die Wichtigkeit und Notwendigkeit der sorgsamen Auswahl von Satellitendaten für Landbedeckungskartierungen hervor und unterstreicht das Potential der Fusion von optischen und SAR-Daten für qualitative Fernerkundungsauswertungen. Die Ergebnisse machen den Einfluss der Klassifikationsgenauigkeit auf die Berechnung von Landschaftsmaßen (landscape metrics) deutlich. Dieser Einfluss ist nicht einheitlich sondern von den Eigenschaften der Maße abhängig, wobei flächenbezogene Indikatoren einer stärkeren Schwankung unterworfen sind als Konnektivitäts- und Diversitätsmaße. Insgesamt unterstreichen die Ergebnisse die Notwendigkeit der Berücksichtigung von Unsicherheiten in den Datengrundlagen bei der räumlich expliziten Landschaftsanalyse.

1 Introduction

Human-dominated landscapes are characterised by complex mosaics of agricultural, semi-natural and natural habitats. Several studies have shown that landscape heterogeneity affects species diversity and ecosystem functions, such as pollination (e.g. Westphal et al. 2006, Tscharntke et al. 2012). Landscape complexity in this context is routinely quantified by measures of landscape composition and configuration (landscape metrics). Remote sensing based land cover and habitat

www.schweizerbart.de
DOI: 10.1127/1432-8364/2013/0165
1432-8364/13/0165 $ 2.50

maps provide the base for the calculation of those landscape metrics and have been widely used for ecological studies that account for spatial scale as an indicator for ecological diversity (e.g. Gillespie et al. 2008, Perovic et al. 2010). The statistical background and behaviour of landscape metrics is well documented (Riitters et al. 1995, Neel et al. 2004). Less attention has been paid to the spatial uncertainty of the satellite maps underlying the landscape metrics calculation. Uncertainty in this context can be a function of the classification scheme, the spatial/thematic scale and the classification accuracy and has been subject to investigation in many theoretical studies based on synthetic data (e.g. Buyantuyev & Wu 2007, Langford et al. 2006, Wickham et al. 1997, Saura 2002). However, in a recent study Lechner et al. (2012) reported that only 1 out of 59 studies in landscape ecology accounted for the effect of classification accuracy on landscape metrics and hence on ecological analyses.

In this study, a multi-sensor optical and SAR satellite dataset (RapidEye, RADARSAT-2, TerraSAR-X) is evaluated for its ability to map land cover type with a focus on functional habitat types (semi-natural habitats) for ecological studies. The quality of land cover maps is documented in terms of classification accuracy and variation in accuracy measures. The synergy of optical and SAR data for mapping land cover is evaluated by means of classification accuracy and relative importance of input variables. In a second step, the effect of classification accuracy on variations in landscape metrics is tested. Here, the author follows the hypothesis of Langford et al. (2006) and Lechner et al. (2012) that uncertainty in land cover maps induces errors in landscape pattern analyses.

2 Data

The study area is located in the vicinity of the UNESCO-biosphere reserve "Schorfheide-Chorin" in eastern Germany, about 50 kilometres north of Berlin. It is characterized by sander areas and moraines which are representative for the glacially formed lowlands of north-eastern Germany. The cultural landscape is dominated by intensive agricultural production fields (cropland and grassland) that are flanked by many small to large lakes, fens and mires. Besides intensive agriculture, there are considerable areas of extensive cultivation and semi-natural habitats.

2.1 *Field Data*

Land use type was mapped in a field campaign in 2009 in 5 different land use clusters comprising more than 3000 polygons and covering a total area of 22,891 ha. Additionally, information on crop type and productive grassland were available for the investigation period (2011) from the agricultural ministry of the federal state of Brandenburg. These two data sources were merged to a comprehensive ground truth dataset for our investigation. In total, the land cover is represented by a two-level classification system including 6 general land use types at the first level and 18 habitat subtypes at the second level. However, earlier investigations (Erasmi et al. in press) have shown that some of the thematic classes at the sub-level are not well represented by the available satellite data. Furthermore, not all of the subtypes are relevant for habitat and biodiversity mapping within the present case study. This is why in this study the number of subtypes was aggregated to the 9 classes grassland (managed), semi-natural habitats (mainly extensively grassland, fallow land and wetland), bushland (also including trees outside forest, hedges, scrups), water, settlements and four types of cropland (cereals, corn, rapeseed, other crops).

Following McCoy (2005) and taking into account the resolution (5 m) of the satellite images and the positional accuracy of the remote sensing data and the field data, the minimum mapping unit (MMU) was determined with 500 m^2. In order to avoid mixed pixels and improve spectral separability, only the core areas of fields were analysed using a margin zone of 10 m for all objects. After applying the MMU and core area criteria and further taking into account the intersection of the coverage of the different satellite data sources, a total of 1581 patches remained for the analysis.

2.2 *Satellite Data*

In total, six RapidEye level 1B (RE1 – RE6), six TerraSAR-X stripmap (dual polarization) (TS1 – TS6) and four RADARSAT-2 scenes (fine beam Quad polarization) (RS1 and RS2) were successfully acquired during the growing season 2011. Fig. 1 shows extracts of colour composites for all satellite sensors together with an overview of the classification scheme. Fig. 2 illustrates the temporal distribution of the data acquisitions for all three sensors along the growing period from April to mid of August 2011. Due to weather constraints, no RapidEye acquisitions were possible after 29th June 2011. Heavy rainfall on 4th July also impacted the X-Band SAR image from TerraSAR-X and the acquisition could not be used for further investigations.

The processing of the RapidEye data included rigorous orthorectification after Toutin (2004), co-registration, atmospheric correction (ATCOR) and calculation of the normalized difference vegetation index (NDVI). All processing was done using PCI Geomatica 10.3 software (PCI 2013). The output is a dataset of six spectral parameters (blue, green, red, Red-Edge, NIR, NDVI) at 5 m spatial resolution for each acquisition. However, for analysis, only four parameters were used (green, Red-Edge, NIR, NDVI) to minimize redundancy in the input variables. RADARSAT-2 single look complex (SLC) data were filtered using the SCL Gaussian DE MAP Filter (Nezry & Yakam Simen 1999). Filtering was followed by a "Pauli coherent decomposition" of the fully polarimetric SLC dataset in terms of elementary scattering mechanisms (Cloude & Pottier 1996). Geometric and radiometric calibration (sigmaθ, dB) together with mosaicking of a pair of two adjacent scenes resulted in a dataset of six polarimetric layers (HH, HV, VV, Pauli1, Pauli2, Pauli3) at 5 m spatial resolution for each acquisition period (RS1 and RS2, Fig. 2).

TerraSAR-X SLC data were processed using a De Grandi multitemporal filter (deGrandi et al. 1997). Together with multilooking, co-registration and radiometric calibration, two filtered polarization layers (HH, HV) at 5 m

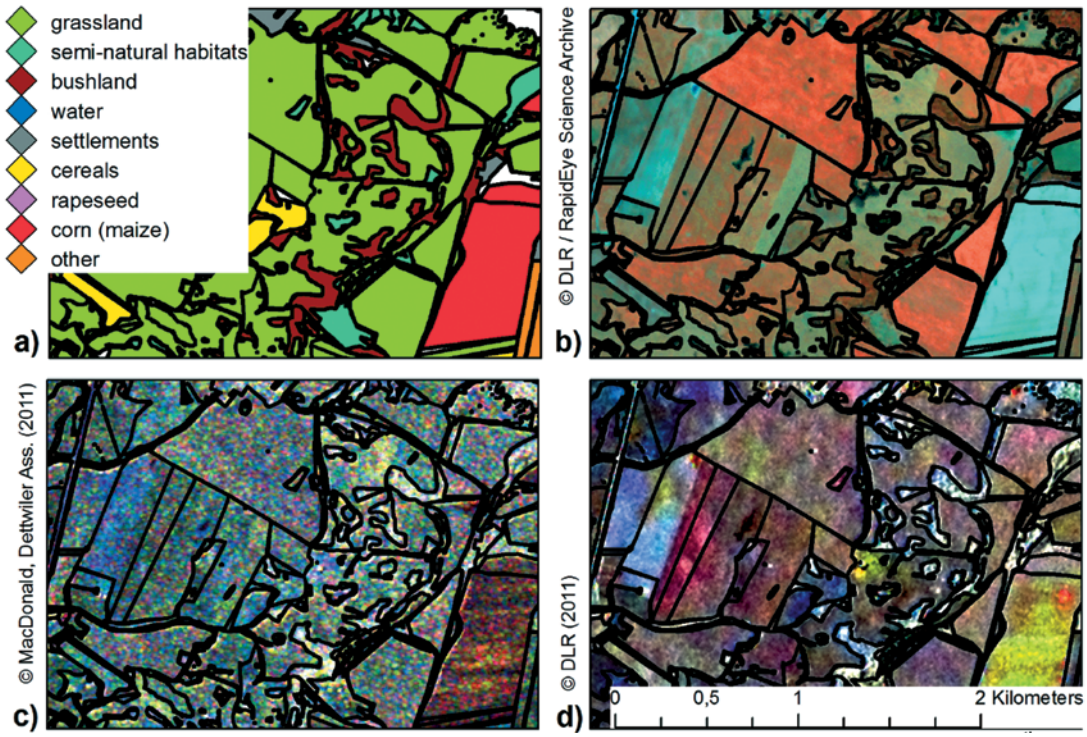

Fig. 1: Overview of data sources (a) ground truth, (b) RapidEye image (NIR, RE, G, 26th May 2011), (c) RADARSAT-2 image (VV,VH,HH; 20th May 2011), (d) TerraSAR-X image (17th August, 21st May, 7th April 2011).

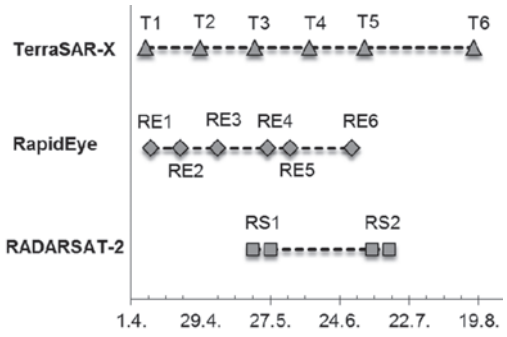

Fig. 2: Temporal profile of acquisitions for RapidEye and RADARSAT-2 and TerraSAR-X data.

spatial resolution were produced for each acquisition date. All SAR processing was done using ENVI/SarScape4.4 ® software.

3 Methods

3.1 *Image Classification*

The classification concept builds on the object (or patch) as the smallest entity. This means that each set of parameters from the optical and/or SAR data is examined at the patch-level of the existing ground truth base map. This ensures that every single object in the ground truth data base is assigned to a single land use type and within-field heterogeneity or mis-assignments are minimized. In the present study, spatial statistics (mean) were calculated at the patch level for each spectral and polarimetric parameter using standard GIS software (ESRI 2013). The outcome was a database of 46 independent variables that built the independent variables for the classifier. The variables were grouped by date of acquisition (n = 13) and by sensor (n = 3). In a first run, the information content of the variables was systematically evaluated using all possible combinations of acquisition dates for a single sensor system (n = 89). In the second run, only the best sensor-specific combinations of input variables were tested for synergy effects with the other two sensors systems. The precondition for the selection in the second run was based on the analysis of the quartiles of data distribution for all land cover types where only those classifications were chosen that are in the upper 10 %-quartile for at least two land cover categories. Out of this subset (n = 16), all possible bi-sensoral combinations (n = 77) between the three sensor systems were evaluated.

All classifications were run using a classification and regression tree (CART) algorithm (Breiman et al. 1984) in SPSS ® Version 20.0. Training data were selected from the ground truth dataset using a random split-sample validation approach with 30 % training and 70 % validation samples. Accuracy of the classification result was accounted for by calculating the overall accuracy assessment (OAA) as well as producer's accuracy (PA) and Cohen's kappa coefficient. Additionally, in order to evaluate the best predictors for every single classification, the normalized importance factor (NI) was computed (Erasmi et al. in press). The NI is based on the importance of each independent variable (input channel) for the regression tree classifier, weighted over the number of classification attempts where the variable was used:

$$NI_p = \sum_{i=1}^{n} \frac{I_{p,i}}{n} \quad (1)$$

where

NI_p = normalized importance of independent variable p
$I_{p,i}$ = importance of parameter p in classification i
n = total number of classifications with parameter p

3.2 *Landscape Metrics*

Based on the classification results a number of selected landscape metrics were computed. The subset is oriented towards a comparison of different groups of metrics and their sensitivity to classification accuracy of the underlying land cover maps. The chosen subset includes area metrics (percentage of land cover type: PLAND), shape metrics (perimeter area ratio: PARA), diversity metrics (Shannon's diversity: SDI; Shannon's eveness: SEI; Dominance) as well as connectivity metrics (landscape division index: LDI). For a comparison

and explanation of all metrics, see e.g. RIITTERS et al. (1995). Area, shape and connectivity metrics were calculated at the class level for four habitat types only. Diversity metrics can only be computed at the landscape level and made use of all available land cover types. All landscape metrics were calculated with V-LATE 2.0 beta for ArcGIS 10.0 (ZGIS 2013). Variability of landscape metrics values with regard to the entity of classification attempts was assessed by computing the normalized deviation of the landscape index values in relation to the metrics value of the reference data, $d_{p,i}$:

$$d_{p,i} = \frac{LI_{p,i}}{LI_{ref}} \quad (2)$$

where

$d_{p,i}$ = normalized deviation of landscape index p for classification i
$LI_{p,i}$ = value of landscape index p for classification result i
LI_{ref} = landscape index value for reference classification

In order to avoid pseudo-variation in the landscape metrics due to inadequate input parameters (here: classification results), only classified images with an OAA of 75 % and higher were considered for landscape analysis. The similarity of the input data was further evaluated using a non-parametric hypothesis test for statistical dependence based on the tau coefficient (Kendall rank correlation). The output proved that, based on a significant difference at p = 0.01, all classified images were similar to the reference dataset (n = 1580).

4 Results

4.1 *Classification and Accuracy Assessment*

Land cover classifications were run for all possible single-sensor combinations with regard to the date of acquisition. This yielded in a total of 57 classifications for RapidEye data (with one to six acquisition dates), 29 combinations for TerraSAR-X data (with on to five acquisitions) and three attempts for RADARSAT-2 data (single or bi-temporal acquisition). The OAA for all single-sensor combinations is given in Fig. 3. This graphical overview illustrates the considerable variability of OAA within a sensor-group and between sensor-systems. The CART-ID in Fig. 3 refers to a set of single-time to multi-temporal image combinations for the three sensor systems (see Fig. 2). The complexity of the input dataset for each sensor increases with the rank of the CART-ID. The results for RapidEye classifications show a general increase of OAA with increasing complexity of the input data (= number of acquisitions). However, highest OAA is achieved for a bi-temporal configuration using acquisitions RE3 and RE4 (beginning and end of May; CART-ID 15; OAA = 82.78 %). TerraSAR-X data perform significantly worse compared to RapidEye in terms of OAA. Best results were reached with a combination of four out of five acquisitions covering the whole investigation period from beginning of April until mid of August (CART-ID 82: T1,-2,-3,-5; OAA = 73.45 %). OAA values for RADARSAT-2 classifications are in the same magnitude as TerraSAR-X but with considerable lower OAA for the best classification result (mono-temporal, CART-ID 86: RS1; OAA = 66.83 %).

The second run of classifications aimed at the optimization of the previous results with regard to OAA and PA. This was accomplished using only selected bi-sensoral combinations of input datasets as described in the methods section. The graphical summary of

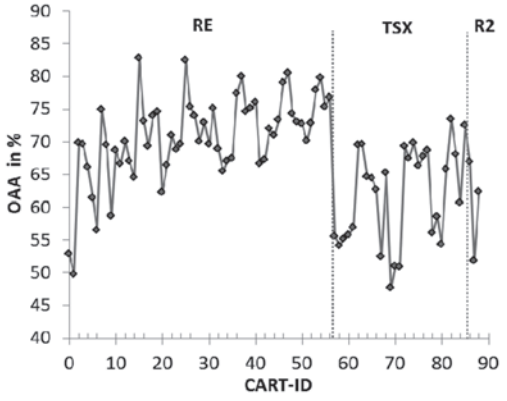

Fig. 3: Overall accuracy assessment (OAA) for single-sensor band combinations (RE = RapidEye, TSX = TerraSAR-X, R2 = RADARSAT-2).

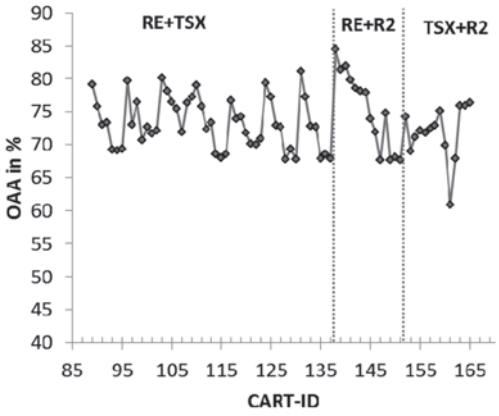

Fig. 4: Overall accuracy assessment (OAA) for bi-sensoral parameter combinations (RE = RapidEye, TSX = TerraSAR-X, R2 = RADARSAT-2).

OAA values for all 77 tested combinations is given in Fig. 4. Highest OAA for RapidEye and TerraSAR-X combinations is achieved for a combination of the best single-sensor datasets (CART-ID 131: RE3,-4,T1,-2,-3,-5; OAA = 81.13 %). However, the OAA is below the value for the RapidEye single-sensor classification. The variability of OAA for all RapidEye-/TerraSAR-X-attempts is lower compared to single-sensor classifications. RapidEye and RADARSAT-2 acquisitions yielded the highest OAA for all bi-temporal combinations. Again, the best result is achieved using the best single-sensor datasets (CART-ID 138: RE3,4,RS1; OAA = 84.53). In this case, the OAA increased more than 3 % compared to the highest single-sensor OAA. TerraSAR-X and RADARSAT-2 performed best for a combination of both RADARSAT-2 acquisitions together with the best single-sensor TerraSAR-X dataset (CART-ID 165: T1,-2,-3,-5, RS1,-2; OAA = 76.41 %).

The statistics of the producer's accuracy (PA) for all land cover types together with OAA for single-sensor and bi-sensoral classification configurations are summarized in Tab. 1. The variability of the PA is documented by the spread (minimum, maximum, coefficient of variation (*cv*)) and further characterized by the upper 10 %-quartile of the distribution function for the PA values. The lowest *cv* values for single-sensor observations are found for the class "grassland" (*cv* = 6.32 %). All other classes show considerably higher *cv* values even in cases where the 10 %-quartile is higher than 90 % (see classes "water", "bushland", "rapeseed", "corn" in Tab. 1). This is in accordance with the full data range of those classes and a minimum of 0 % for the classes "water", "rapeseed", "corn" and "other crops".

Bi-sensoral classification runs, in general, show lower variability with a *cv* for three classes below 10 % ("grassland", "bushland", "cereals"). Only two classes ("water", "other crops") could not be distinguished in at least one of the classification attempts. In both cases, "semi-natural habitats" perform under average. However, the variation of the accuracy significantly decreases with bi-sensoral approaches (21.68 % to 13.63 %). The comparison of the OAA statistics shows a substantial enhancement of the classification quality with a decrease of the *cv* from 11.93 % to 5.95 % and a remarkable increase in the mean OAA (67.46 % to 73.36 %) as well as the 10 %-quartile (76.15 % to 79.25 %).

Another focus within the systematic evaluation of the information content for the dataset of the three sensors was on the determination of the most relevant independent variables for mapping habitat type in the study area. The normalized importance factor (*NI*) provides an estimate of the importance of each independent variable (input channel) for the regression tree classifier. Fig. 5 presents a summary of the *NI* for 25 out of 46 variables. Highest *NI* is observed for input channel two (green light) of RapidEye acquisition no. six (29th June) followed by channel 4 (Red-Edge) of RE4 and RE3 (26th May and 06th May). RADARSAT-2 variables are amongst the top ten highest NI values (mid of May, VV and HH polarized) and further spread throughout the whole chart. In contrast, TerraSAR-X variables are only present at the end of the list with two HH-polarized layers from end of April (T2) and mid of May (T3). The number of CART-runs (*n*) in Fig. 5 gives guidance towards the overall relevance of the variables with high *NI* values. The highest *n* values are connected to the RapidEye acquisitions RE3 and RE4. This is a consequence of the high PA and OAA values for RapidEye classifications including these two scenes. Hence, the maximum number of *n* = 63 CART-runs (RE/TS or RE/RS) is realized.

Tab. 1: Statistics of producer's accuracy (PA) for all land cover types and overall accuracy assessment (OAA) for single-sensor and bi-sensoral classification configurations.

	Land cover type	Min	Max	Mean	Upper 10%-Quartile	Coefficient of Variation
PA single-sensor	Grassland	64.72	95.75	83.89	89.04	6.32
	Semi-natural habitats	16.10	71.42	52.04	64.17	21.68
	Water	0.00	99.92	66.50	99.32	55.54
	Bushland	52.66	93.14	80.62	92.09	14.60
	Settlements	3.83	82.42	42.81	69.23	55.10
	Cereals	45.36	90.39	71.10	83.33	14.30
	Rapeseed	0.00	94.72	41.97	92.42	77.42
	Corn (maize)	0.00	95.01	65.53	90.44	37.67
	Other crops	0.00	64.62	21.53	55.75	92.17
	Overall Accuracy	47.69	82.78	67.46	76.15	11.93
PA bi-sensoral	Grassland	83.43	94.67	89.18	93.09	2.87
	Semi-natural habitats	34.29	71.84	58.71	66.18	13.63
	Water	0.00	99.57	63.07	99.52	53.63
	Bushland	71.32	93.99	87.45	92.55	6.50
	Settlements	14.41	71.04	62.94	70.36	20.22
	Cereals	71.52	92.58	80.55	87.00	5.91
	Rapeseed	5.65	93.94	34.53	78.70	71.34
	Corn (maize)	42.65	95.40	77.36	95.01	19.40
	Other crops	0.00	50.93	13.88	38.98	109.54
	Overall Accuracy	60.83	84.53	73.36	79.25	5.95

4.2 *Landscape Metrics and Uncertainty Assessment*

The land cover maps provided the base for the computation of landscape metrics at class and landscape level. As described earlier in the methods section, only classified images (single-sensor and bi-sensoral) with an OAA of at least 75 % were considered for analysis ($n = 42$).

The results of the landscape analysis for the study site are summarized in Tab. 2. The shape metrics at class level in general show low variation except for the class "rapeseed". Compared to this, the area metrics at class level indicate moderate to high variation with *cv* values ranging from 7.94 % to 24.46 %. Class connectivity metrics are in a close range around the reference map and landscape metrics show low to moderate variation in terms of the *cv*.

The main findings from the summary statistics are confirmed by a closer look at the data distribution for selected metrics at class and landscape level. In Fig. 6, the normalized deviation ($d_{p,i}$) is computed for "semi-natural habitat" class metrics (PARA, PLAND, LDI) compared to diversity metrics at landscape level. The graphs illustrate the high variation of area metrics (PLAND) compared to the connectivity and diversity metrics (SDI, SEI, Dominance).

The dissimilarity in sensitivity is mostly explained by the nature of the metrics itself. E.g., PLAND is directly and exclusively depending on changes in land cover composition that are caused by variations in classification results.

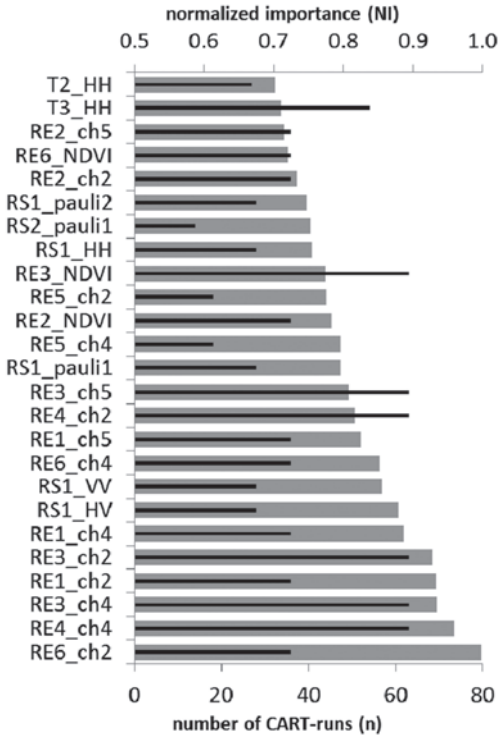

Fig. 5: Normalized importance factor (*NI*) of spectral and polarimetric parameters for all bi-sensoral classifications. A value of 1.0 means that the parameter shows highest relative importance (100 %) in all CART-runs (thin black lines = *n*, grey bars = *NI*).

On the other hand, diversity metrics like SDI are less sensitive to changes in landscape composition and configuration because they are focused on the occurrence of land cover types more than on the areal extent.

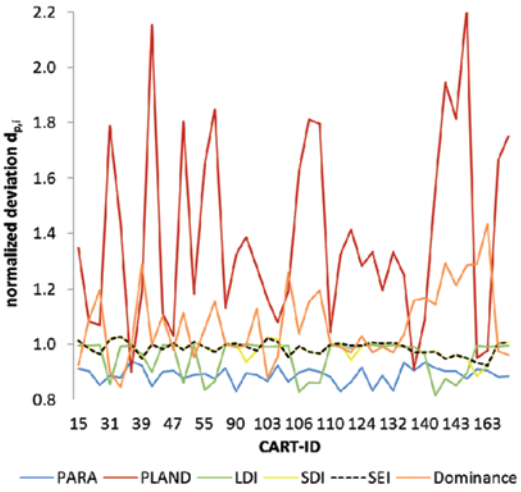

Fig. 6: Normalized deviation ($d_{p,i}$) of class metrics for semi-natural habitats and landscape metrics for all classifications with OAA higher 75 % (n = 42) (PARA = perimeter area ratio, PLAND = percentage of land cover type, LDI = landscape division index, SDI = Shannon's diversity, SEI = Shannon's eveness).

Tab. 2: Statistics (normalized deviation, $d_{p,i}$) describing the variation of the landscape metrics at class and landscape level for selected habitat types in relation to ground truth data.

Level	Group	Metric	Min	Max	Mean	Coefficient of variation
Class level	Shape	PARA_grassland	1.06	1.23	1.15	3.10
		PARA_semi-natural	0.83	0.94	0.89	3.13
		PARA_bushland	0.91	1.02	0.98	2.54
		PARA_rapeseed	0.77	2.66	1.19	46.33
	Area	PLAND_grassland	0.92	1.34	1.12	7.94
		PLAND_semi-natural	0.90	2.21	1.39	24.46
		PLAND_bushland	1.19	2.50	1.65	21.65
		PLAND_rapeseed	0.43	1.07	0.93	12.88
	Connectivity	LDI_grassland	0.998	1.001	1.00	0.05
		LDI_semi-natural	0.81	1.00	0.95	6.55
		LDI_bushland	0.98	1.00	0.99	0.63
		LDI_rapeseed	0.95	1.01	0.99	1.23
Landscape level	Diversity	Shannon's Diversity	0.89	1.03	0.98	2.97
		Shannon's Eveness	0.92	1.03	0.99	2.44
		Dominance	0.85	1.43	1.07	12.31

5 Discussion and Conclusions

The results of the land cover classifications confirm the general ability of optical high temporal and spatial resolution satellite data (RapidEye) for mapping and monitoring habitat types in a heterogeneous agricultural landscape. The accuracy of mapping considerably increases with the availability of multi-temporal datasets for the growing period. High accuracy could already be obtained with bi-temporal observations, where acquisitions at an early stage during the growing season yielded highest accuracy. The *NI*-index demonstrates the high impact of the spectral and temporal domain of the RapidEye time series. In particular, it stresses the relevance of the Red-Edge channel of the RapidEye system for mapping vegetated surfaces. Compared to this, the results of RADARSAT-2 and TerraSAR-X single-sensor classifications are significantly worse. Bi-sensoral combinations of optical and SAR-data yielded satisfying accuracy, where RADARSAT-2 polarimetric data outperform the TerraSAR-X time series with regard to its potential for synergistic optical/SAR habitat type mapping. However, the documented potential of optical-SAR fusion is clearly directed towards the availability of SAR data in mid-latitude regions with frequent weather constraints.

The landscape analysis in terms of class and landscape metrics shows diverse patterns of uncertainty that can be addressed by different groups of metrics. In general, the results show that area based metrics, e.g. percentage of land cover class, are most sensitive to classification accuracy and variability of mapping results. The magnitude of variation for those metrics is much higher than the classification errors. The same problem has been reported by Langford et al. (2006). Shape and connectivity measures at class level seem to be more resistant to changes in landscape composition and configuration. The same applies for diversity metrics at landscape level that are less affected by landscape composition which is in accordance with findings by Altamirano et al. (2012).

The results demonstrate that the choice of satellite sensor systems and acquisition periods essentially impact the result of habitat type mapping and hence directly influence any study that aims at quantifying the composition and configuration of landscapes for biological conservation issues. As shown here, variations in landscape metrics are the result of only slight changes in input variables for land cover classification approaches. The same problem arises, when different classification algorithms are used to map a landscape from identical input data as shown in Mas et al. (2010) or when spatial or thematic resolution is not a constant in the model (Baldwin et al. 2004, Buyantuyev & Wu 2007). On the other hand, there are groups of landscape metrics that are not affected by changes in landscape composition as reported also by Wickham et al. (1997). Therefore, comparison of landscape metrics for different regions or for temporal change analysis always has to account for the accuracy of the underlying land cover map and for the sensitivity of the landscape metrics to land cover variations.

Acknowledgements

RapidEye data are provided by the RapidEye Science Archive (RESA) of the German Aerospace Center (DLR) within the project RESA-451. RADARSAT-2 data are provided by the Canadian Space Agency (CSA) and MacDonald, Dettwiler and Assoc. Ltd. under contract no. SOAR-5040. TerraSAR-X data are made available from DLR under contract no. LAN0901.

References

Altamirano, A., Miranda, A. & Jimenez, C., 2012: Uncertainty of landscape indices for spatial structure analysis. – Bosque **33** (2): 171–181.

Baldwin, D.J., Weaver, K., Schnekenburger, F. & Perera, A.H., 2004: Sensitivity of landscape pattern indices to input data characteristics on real landscapes: implications for their use in natural disturbance emulation. – Landscape Ecology **19** (3): 255–271.

Breiman, L., Friedman, J.H., Olshen, R.A. & Stone, C.J., 1993: Classification and regression trees. – Chapman & Hall, New York, USA.

Buyantuyev, A. & Wu, J., 2007: Effects of thematic resolution on landscape pattern analysis. – Landscape Ecology **22** (1): 7–13.

Cloude, S.R. & Pottier, E., 1996: A review of target decomposition theorems in radar polarimetry. – IEEE Transactions on Geoscience and Remote Sensing **34** (2): 498–518.

Erasmi, S., Riembauer, G. & Westphal, C., in press: Mapping habitat diversity from multitemporal Rapid-Eye and RADARSAT-2 data in Brandenburg, Germany. – Borg, E. (ed.): RapidEye Science Archive. – Gito, 20.–22. March 2013, Neustrelitz, Berlin.

ESRI, 2013: www.esri.com (19.2.2013).

Gillespie, T.W., Foody, G.M., Rocchini, D., Giorgi, A.P. & Saatchi, S., 2008: Measuring and modelling biodiversity from space. – Progress in Physical Geography **32** (2): 203–221.

de Grandi, G., Leysen, M., Lee, J. & Schuler, D., 1997: Radar reflectivity estimation using multiple SAR scenes of the same target: technique and applications. – Geoscience and Remote Sensing, 1997, IGARSS '97. Remote Sensing – A Scientific Vision for Sustainable Development. – 1997 IEEE International **2:** 1047–1050.

Langford, W.T., Gergel, S.E., Dietterich, T.G. & Cohen, W., 2006: Map misclassification can cause large errors in landscape pattern indices: Examples from habitat fragmentation. – Ecosystems **9** (3): 474–488.

Lechner, A.M., Langford, W.T., Bekessy, S.A. & Jones, S.D., 2012: Are landscape ecologists addressing uncertainty in their remote sensing data? – Landscape Ecology **27** (9): 1249–1261.

Mas, J.-F., Gao, Y. & Navarrete Pacheco, J.A., 2010: Sensitivity of landscape pattern metrics to classification approaches. – Forest Ecology and Management **259** (7): 1215–1224.

McCoy, R.M., 2005: Field methods in remote sensing. – Guilford Press, New York.

Neel, M.C., McGarigal, K. & Cushman, S.A., 2004: Behavior of class-level landscape metrics across gradients of class aggregation and area. – Landscape Ecology **19** (4): 435–455.

Nezry, E. & Yakam Simen, F., 1999: A family of distribution-entropy MAP speckle filters for polarimetric SAR data, and for single or multichannel detected and complex SAR images. – CEOS SAR Workshop (ESA SP-450): 219–223.

PCI, 2013: PCI Geomatics Incorporated. – www.pcigeomatics.com (19.2.2013).

Perovic, D.J., Gurr, G.M., Raman, A. & Nicol, H.I., 2010: Effect of landscape composition and arrangement on biological control agents in a simplified agricultural system: A cost-distance approach. – Biological Control **52** (3): 263–270.

Riitters, K.H., O'Neill, R.V., Hunsaker, C.T., Wickham, J.D., Yankee, D.H., Timmins, S.P., Jones, K.B. & Jackson, B.L., 1995: A factor analysis of landscape pattern and structure metrics. – Landscape Ecology **10** (1): 23–39.

Saura, S., 2002: Effects of minimum mapping unit on land cover data spatial configuration and composition. – International Journal of Remote Sensing **23** (22): 4853–4880.

Toutin, T., 2004: Review article: Geometric processing of remote sensing images: models, algorithms and methods. – International Journal of Remote Sensing **25** (10): 1893–1924.

Tscharntke, T., Tylianakis, J.M., Rand, T.A., Didham, R.K., Fahrig, L., Batáry, P., Bengtsson, J., Clough, Y., Christ, T.O., Dormann, C.F., Ewers, R.M., Fründ, J., Holt, R.D., Holzschuh, A., Klein, A.M., Kleijn, D., Kremen, C., Landis, D.A., Laurance, W., Lindenmayer, D., Scherber, C., Sodhi, N., Steffan-Dewenter, I., Thies, C., van der Putten, W.H. & Westphal, C., 2012: Landscape moderation of biodiversity patterns and processes – eight hypotheses. – Biological Reviews **87** (3): 661–685.

Westphal, C., Steffan-Dewenter, I. & Tscharntke, T., 2006: Bumblebees experience landscapes at different spatial scales: possible implications for coexistence. – Oecologia **149** (2): 289–300.

Wickham, J.D., ONeill, R.V., Riitters, K.H., Wade, T.G. & Jones, K.B., 1997: Sensitivity of selected landscape pattern metrics to land-cover misclassification and differences in land-cover composition. – Photogrammetric Engineering and Remote Sensing **63** (4): 397–402.

ZGIS, 2013: Universität Salzburg, Department of Geoinformatics. – www.zgis.at (19.2.2013).

Address of the Author:

Dr. Stefan Erasmi, Cartography, GIS & Remote Sensing Department, Institute of Geography, Georg-August-University Göttingen, Goldschmidtstraße 5, D-37077 Göttingen, Germany, e-mail: serasmi@uni-goettingen.de

Manuskript eingereicht: November 2012
Angenommen: Februar 2013

PFG 2013 / 3, 0149–0161
Stuttgart, June 2013

Article

Object Features for Pixel-based Classification of Urban Areas Comparing Different Machine Learning Algorithms

Nils Wolf, Bochum

Keywords: urban remote sensing, machine learning, object-based feature extraction, spatial-spectral classification

Summary: Image segmentation is a means to extract valuable spatial descriptors from urban remote sensing images. These descriptors (object features) can be concatenated at the pixel level to the spectral feature vector. Resulting spatial-spectral input spaces become more complex, but it is assumed that they offer in conjunction with appropriate classification techniques a better discrimination of classes. Comparing different supervised learning algorithms, this study empirically evaluates the value of adding object-based features into per-pixel classification. The considered algorithms are decision tree, decision tree ensembles (bagging and random forest), support vector machines (linear and rbf kernel), and k-nearest neighbour. The pixel level is suggested as the preferable domain for accessing object features in order to facilitate unbiased training, tuning and testing of algorithms within an implemented nested cross-validation scheme. Different case studies of urban remote sensing are considered to conduct the experiments, namely building detection with hyperspectral data (CASI) and aerial photography (Leica RC30), the mapping of pools, turf grass and non-turf vegetation in an urban tourist area using WorldView-2 panchromatic data, urban land cover classification using a hyperspectral benchmark dataset (ROSIS) and the classification of urban tree species (CASI). The results show that spatial features derived from segmentation levels have a great value for these applications. Concerning the algorithm performance, decision tree ensemble and support vector machine approaches yield in overall better results than decision tree and k-nearest neighbour.

Zusammenfassung: *Objektmerkmale für die pixelbasierte Klassifizierung urbaner Räume: ein Vergleich von Algorithmen des maschinellen Lernens.* Die Bildsegmentierung ermöglicht es, aus urbanen Fernerkundungsszenen wichtige räumliche Deskriptoren zu extrahieren. Diese Deskriptoren (Objektmerkmale) können auf Pixelebene mit dem spektralen Merkmalsvektor kombiniert werden. Resultierende räumlich-spektrale Merkmalsräume sind komplexer, aber es wird vermutet, dass sie in Verbindung mit angemessenen Klassifizierungstechniken eine bessere Trennung von Klassen ermöglichen. Im Vergleich verschiedener überwachter Lernalgorithmen untersucht diese Studie empirisch den Wert von objektbasierten Merkmalen für die pixelbasierte Klassifizierung. Die untersuchten Algorithmen sind decision tree, decision tree ensembles (bagging und random forest), support vector machines (linear und rbf kernel) und k-nearest neighbour. Die Pixelebene ist dabei als bevorzugte Domäne für das unverzerrte Trainieren, Tunen und Testen der Algorithmen innerhalb einer verschachtelten Kreuzvalidierung anzusehen. Für die Durchführung der Experimente werden verschiedene Fallstudien urbaner Fernerkundung berücksichtigt, namentlich Gebäudedetektion sowohl mit Hyperspektralscanner-Daten (CASI) als auch Luftbildern (Leica RC30), Kartierung von Swimmingpools, Rasenflächen und Baum-/Strauchvegetation in einer touristisch geprägten urbanen Region mit panchromatischen WorldView-2 Daten, Klassifizierung urbaner Landbedeckung mit einem hyperspektralen Benchmark-Datensatz (ROSIS) und die Klassifizierung urbaner Baumarten (CASI). Die Ergebnisse zeigen, dass die aus Segmentierungsebenen extrahierten räumlichen Merkmale für diese Anwendungsbeispiele einen bedeutenden Mehrwert haben. Hinsichtlich des Algorithmenvergleichs lieferten decision tree ensembles und support vector machines übergreifend deutlich genauere Ergebnisse als decision tree und k-nearest neighbour.

www.schweizerbart.de
DOI: 10.1127/1432-8364/2013/0166
1432-8364/13/0166 $ 3.25

1 Introduction

Classification is a common processing step to convert image data into tangible information and its practice in remote sensing is well established for a wide range of applications (Lu & Weng 2007). A particular problem in urban remote sensing is the spectral diversity (Herold et al. 2003) and the spatial complexity of this environment, which complicates decoding of the spectral signals. This is especially valid for studies mapping inner cities or targeting specific materials and objects. The complexity relates to the various artificial and natural surfaces and, moreover, to the presence of vertical structures and non-horizontal surfaces which cast shadows and effect the angular distribution of reflected light. This finally limits analysis approaches which solely rely on the pixelwise interpretation of the spectral values. In fact, these approaches treat an image as being an unordered list of spectral measurements and neglect the spatial structure of these measurements. This is the reason why there is wide consensus that spatial information considered in image analysis can be advantageous and thus, various methods have been developed and applied, for example those based on textural, morphological or object features (Lu & Weng 2007, Palmason et al. 2005, Tarabalka et al. 2010).

From about the year 2000 onwards, the object-based paradigm has gained increasing attention (Blaschke 2010), with a research focus on knowledge-driven approaches (Baatz & Schäpe 1999, Benz et al. 2004, Blaschke et al. 2008, Burnett & Blaschke 2003). As a consequence, supervised classification algorithms and comparison studies, which were well established in the pixel-based context, e.g. Huang et al. (2002) and Waske et al. (2009), have been rarely studied under the object-based paradigm. This is surprising because it can be advantageous or a complementary approach to complex classification problems where the knowledge representation and organization becomes difficult and loses its operational strengths of transparency and transferability, i.e. the independence of a scene.

Only recently, an increased interest in supervised object-based approaches employing state of the art machine learning algorithms can be observed. For example, Duro et al. (2012) compared the decision tree, support vector machine and random forest classifiers by mapping broad land cover categories in an agricultural landscape using SPOT HRG imagery and found out that random forests and support vector machines perform significantly better than decision trees. Novack et al. (2011) compared decision trees, regression trees, random forests and support vector machines for urban land cover classification using WorldView-2 as well as simulated QuickBird data and concluded that in overall random forests provided the best results and support vector machines the worst. However, one general problem of the application of supervised methods in the object domain is the fact that objects, unlike pixels, are of non-uniform size and distribution and, moreover, that they constitute a generalization of a raster image, i.e. they are even more than pixels affected by thematic uncertainties and ambiguities. Both has an impact on the representation of data samples, i.e. labelled cases used for training, tuning and testing which can misdirect the optimization procedures of algorithms and violate premises of statistically rigorous accuracy assessments (Stehman & Czaplewski 1998).

Having said this, the current paper presents five case studies in which object-based features are used in a pixel-based framework in order to apply and compare a number of non-parametric supervised machine learning algorithms. Object feature layers are extracted from multiple segmentation levels and then stacked as additional raster layers to the original input image. In this way, the spectral feature vector of each pixel is linked to a feature vector that carries spatial information. Using a nested cross-validation scheme, it is investigated whether the resulting *spatial-spectral* input spaces yield higher classification accuracies than the conventional *spectral* input spaces. The algorithms under consideration are decision trees, decision tree ensembles (bagging and random forest), support vector machines (linear and radial basis function kernels), and – to provide a low-cost benchmark – k-nearest neighbour.

2 Materials and Methods

2.1 *Case Studies: Data and Application*

Building detection with CASI hyperspectral data

Hyperspectral data of Bochum, Germany, were acquired on 5th July 2011 with the Compact Airborne Spectrometry Imager (CASI) mounted on an aircraft. The data are available with 1 m/pixel geometric resolution and 72 continuous bands in the range from 380 nm to 1050 nm. A 1341 ha test site (1381 × 9714 pixels) was chosen that covers different urban structures, including high-density block development, industrial and commercial areas, terraced houses, perimeter block development as well as parks and allotments. Using simple random sampling, 2000 pixels have been selected and labelled (*building* or *background*) by intersection with an official roof area cadastre map.

Building detection with colour aerial photography (Leica RC30)

The building detection was also conducted using aerial photography. The images were taken during a flight campaign on 2nd April 2009 with the analogue Leica RC30 camera (film, 400 nm – 1000 nm, colour filter) and later digitalized with a photogrammetric scanner to RGB layers in 10 cm/pixel resolution. To reduce the data volume, the pixel size was degraded to 40 cm. The 1341 ha test site (3,452 × 24,285 pixels) and the procedure to generate labelled sample data are identical to the CASI-based application (cp. above).

Mapping of pools, turf and tree/shrub vegetation with WorldView-2 (WV-2) panchromatic data

A WV-2 satellite scene of the vicinity of Sotogrande, Andalusia, Spain, recorded on 16th July 2010, was available. The data were used to map *swimming pools*, *turf grass* and *trees/shrubs*. The remaining area was considered as *background*. The chosen test site (502 ha subset, ≈ 20 million pixels) represents a high-quality, low-density tourist and residential area, dominated by large private properties with large garden area, most of them include a swimming pool. These urban-tourist zones most notably along the Spanish Mediterranean coast are particularly vulnerable to water shortages induced by climate change. Mapping water-intensive landscape features like pools and irrigated garden vegetation, especially turf, provides an important input for water consumption studies (Hof & Schmitt 2011). Labelled information was available from a visual interpretation of 2059 randomly distributed pixels. For the experiments, only the panchromatic band (0.5 m/pixel, 463 nm – 800 nm spectral range) was chosen in order to test the value of spatial information layers in a context where spectral information is limited.

Urban land cover classification with ROSIS hyperspectral data

Data with 115 spectrally continuous bands in the 430 nm – 860 nm spectrum were recorded (8th July 2002) by the Reflective Optics System Imaging Spectrometer (ROSIS) over Pavia, Italy. Two image subsets (together 715 × 1096 pixels, 102 ha) with 1.3 m/pixel spatial resolution and 102 bands (after removal of noisy bands) were available, covering the city centre. Nine classes, namely *water*, *trees*, *asphalt*, *bricks*, *bitumen*, *tiles*, *shadows* and *meadows* are considered for the experiment. The labelled data sample consists of 99,114 pixels which have been converted from sample polygons (nonprobability sampling). The ROSIS image is a well-known, publicly available benchmark dataset (Palmason et al. 2005, Tarabalka et al. 2010). It was chosen because it provides a good source for transparent algorithm benchmarking beyond the scope of a single study.

Tree species classification with CASI hyperspectral data

The imagery used here is another subset of the CASI data recorded during the flight campaign on 5th July 2011 over the city of Bochum. Labelled information was generated using an official tree cadaster of the local planning authorities. It provides the locations and the spe-

cies information of trees in public space, e.g. on cemeteries, sports facilities, parks or along streets. In a defined 1471 ha subset (1470 × 6242 pixels), the cadaster was filtered to remove sparse species, maintaining only the eight most frequent ones which sum up to 400 trees. They are: *Acer platanoides* (28 cases), *Acer pseudoplatanus* (171), *Acer saccharinum* (43), *Aesculus x carnea "Briotii"* (33), *Betula pendula* (29), *Crataegus x lavallei* (17), *Platanus x acerifolia* (40) and *Tilia tomentosa* (39).

2.2 *Machine Learning*

This paper deals with supervised learning which is among several machine learning paradigms, like unsupervised, active and reinforcement learning, arguably the most relevant one in terms of impact on practical applications. The basic notion of supervised learning is the approximation of a target function f: $X \rightarrow Y$ based on observational or sample data (x_1, y_1), (x_2, y_2), …, (x_n, y_n), with x being a p-dimensional input vector and y an outcome. X and Y denote the complete set of possible input and output data and remaining unknowns, likewise f. Learning tasks can be categorized into regression leading to continuous output, and classification leading to discrete output. The empirical experiments and the following introductory descriptions address the classification case. The algorithms are implemented within the statistical programming environment *R* (R Core Team 2012) and its contributed packages. An overview of the algorithms with the related *R* packages, functions, parameters and key references (for implementation details) is given in Tab. 1.

Decision Tree (DT)

DTs recursively partition the input space by axis-parallel splits into a set of rectangular areas, aiming thereby at grouping data points with the same class. The implementation used in this work is based on classification and regression trees (CART) by Breiman (1984). Following a greedy problem solving heuristic, trees begin with a root node where the locally best univariate binary split is selected. The selection relies on an exhaustive search through all variables and possible thresholds regarding a defined measure which quantifies the reduction in class impurity obtained by a particular split. Then, the child nodes are considered themselves as the new roots and the process iterates until pure end nodes, the leaves, are reached. The impurity measure used in this study is the Gini index (Breiman 1984):

$$G = \sum_{i=1}^{c} P(\omega_i)(1 - P(\omega_i)) \quad (1)$$

Tab. 1: Overview of algorithms and their implementation and calibration (DT = Decision Tree, BAG = Bagging, RF = Random Forest, SVM = Support Vector Machines, rbf = radial basis function, KNN = k-Nearest Neighbour).

Algorithm	R package/*function* key reference	Fixed parameter	Tuning parameter
DT	rpart / *rpart*() (Therneau & Atkinson 1997)	n/a	$cp = \{2^{-10}, 2^{-9},..., 2^{-1}\}$
BAG	randomForest / *randomForest*() (Svetnik et al. 2003)	*ntree* = 500 *mtry* = p	n/a
RF	randomForest / *randomForest*() (Svetnik et al. 2003)	*ntree* = 500 $mtry = \lceil\sqrt{p}\rceil$	n/a
SVM rbf	kernlab / *ksvm*() (Karatzoglou et al. 2004)	*kernel* = "rbfdot"	$C = \{5^{-2}, 5^{-1},..., 5^{7}\}$ $\sigma = \{5^{-7}, 5^{-6},..., 5^{-1}\}$
SVM linear	kernlab / *ksvm*() (Karatzoglou et al. 2004)	*kernel* = "vanilladot"	$C = \{5^{-2}, 5^{-1},..., 5^{7}\}$
KNN	class / *knn*() (Venables & Ripley 2002)	n/a	$k = \{2^{0}, 2^{1},..., 2^{4}\}$

with $P(\omega_i)$ being the relative frequency of the ith class out of c classes in the node. The impurity reduction G_{gain} of a particular split is derived by comparing the impurity of the current root node G_{root} with its child nodes G_{left} and G_{right}:

$$G_{gain} = G_{root} - (G_{left} + G_{right}). \quad (2)$$

The variable-threshold combination with the highest G_{gain} is chosen to split the data. Trees, as described so far, are fully grown in the sense that they branch out until pure end nodes are reached. Thereby, they overfit the training data (performing 100 % accurate on it) and miss generality when it comes to the prediction of unseen data. To restrict the complexity of trees, several *pruning* approaches exist. The one used in this study is based on the complexity cost *cp* (Therneau & Atkinson 1997), here defined by a tuning range (Tab. 1).

Bagging (BAG) and Random Forest (RF)

BAG is an ensemble method proposed by Breiman (1996). It uses bootstrap replicates (Efron & Tibshirani 1994) of the data in order to generate multiple versions of a classifier, here unpruned DTs as described in the previous section. The predictions of the trees are then aggregated by plurality votes. Fully grown decision trees can be considered as being very suited for this aggregation. They overfit the training data and guarantee thereby variance among the outcomes, which is in this case a desired feature.

RF builds upon the concept of BAG, but additionally incorporates the basic notion of random subspaces (Ho 1998). It differs in that the best split at each tree node is obtained from random subspaces with a defined dimensionality $< p$, for x^p. Here, the dimensionality of random subspaces *mtry* is set to $\lceil \sqrt{p} \rceil$. The number of trees, *ntree*, for BAG and RF is set to 500.

Support Vector Machines (SVM linear and SVM rbf)

The main notion of SVMs is to define the optimal hyperplane in the input space which separates data points of two classes, by convention $y \in (-1, 1)$. The optimization attempts to fix the empirical error on the training data and to maximize the margin between the hyperplane and the closest data points from each class. This follows the intuition that a fat margin decreases the risk of misclassifying unseen patterns (Vapnik 1998).

The separating hyperplane H is defined as $w \cdot x + b = 0$, where $x \in \mathbf{R}^p$ is any point on the plane, $w \in \mathbf{R}^p$ is the normal vector, i.e. in X orthogonal to the hyperplane, and $b \in \mathbb{R}$ is the bias.

The distance between the H and the coordinate system's origin can be expressed by $|b|/||w||$, with $||w||$ being the Euclidian norm of w. The data points of both classes closest to H are the so-called support vectors and their locations are defined to be on the hyperplanes $H_1 : w \cdot x + b = 1$ and $H_2 : w \cdot x + b = -1$, with H_1 and H_2 being parallel to H, hence sharing the same normal w. Their distances to the origin are given by $|1 - b|/||w||$ and $|-1 - b|/||w||$ respectively. The distances of H_1 and H_2 to H are equally $1/||w||$ and the margin, the distance between H_1 and H_2, is $2/||w||$.

The optimization problem now aims at finding H with the maximum margin by minimizing $||w||^2$, subject to the constraint that no data point lays in the margin area. This is termed *soft margin*. However, often the constraints are weakened to reduce the complexity and increase the generalization capacity of the solution. This is done by introducing a slack variable $\xi \geq 0$ that penalizes the misclassification of data points. The impact of ξ on the solution is controlled by the cost parameter C. The constrained optimization problem can be summarized as follows:

$$minimize \left[\frac{1}{2} \|w\|^2 + \frac{C}{n} \sum_{i=1}^{n} \xi_i \right] \quad (3)$$

$$subject\ to \begin{cases} w \cdot x + b \geq +1 - \xi_i \text{ if } y_i = +1 \\ w \cdot x + b \leq -1 - \xi_i \text{ if } y_i = -1 \end{cases} \quad (4)$$

The C parameter allows treating outliers, in remote sensing for example the spectral signal of a sparse material, and noise, e.g. mislabelled ground truth pixels. However, the still linear approach requires an adaptation unless the noise but the underlying processes, e.g. ra-

diative transfer, cause problems because of the non-linearity of the system $X \rightarrow Y$. Then the input data can be mapped by a kernel function to a higher dimensionality, where it is more likely to follow a linear distribution that suits a hyperplane which represents a linear decision boundary. The mapping is defined by a kernel function $k(x_i, x_j) = \langle \phi(x_i) \,|\, \phi(x_j) \rangle$ which returns the dot product of two data points x_i and x_j, given a defined projection $\phi : X \rightarrow Z$ with the data points appearing only inside dot products with other points, this method allows to let the algorithms operate in X instead of Z space, which is commonly referred to as the *kernel trick* (Schölkopf & Smola 2002) because it saves computational costs. Often applied kernels are polynomial, sigmoid and Gaussian radial basis function (rbf). The rbf kernel is used in this study, which is defined as:

$$k(x_i, x_j) = \exp(-\sigma \|x_i - x_j\|^2), \sigma \in \mathbf{R}^+ \quad (5)$$

with σ controlling the width of the Gaussian rbf. Both C and σ are parameters that have to be set by the user.

In this study, C and σ have been defined by a tuning grid (SVM rbf) or range (SVM linear) (Tab. 1). Furthermore, by default, all data is scaled prior to model generation to avoid that features with greater numeric range dominate those with smaller ranges. In order to extend from binary to multiclass cases with $c > 2$ classes, the *one-against-one* cascade is used, in which $c(c-1)/2$ binary models are trained to predict the final class by voting. For a comprehensive tutorial on support vector machines, which also outlines how to solve the constrained optimization problem (1)(2), the reader is referred to Burges (1998).

k-Nearest Neighbour (KNN)

KNN can be considered as a benchmark for more sophisticated approaches because it has a simple intuition and low computational demands. KNN does rather memorize than learn data. It relies on the closeness of still unclassified data to the k closest training data points in the input space. To measure closeness typically Euclidian distance is used. If $k > 1$, majority voting determines the final class.

2.3 *Object Feature Extraction*

Using eCognition software, a routine for object-based feature extraction has been developed which generates three segmentation levels from its input layers. Then, on each level, a defined set of object features layers (see Fig. 1 and Tab. 2 for examples) is computed and finally exported into a raster format for layer stacking and subsequent analysis. The set comprises features describing the objects' geometry and also those referring to the pixel

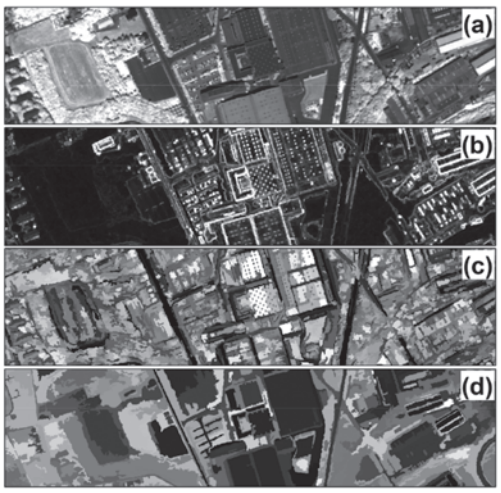

Fig. 1: Examples of spectral and spatial features: (a) CASI band #49 (831 nm) at pixel level; (b) *Mean difference to neighbours layer 1* (CASI band #11, 466 nm) at object level scale 20; (c) *Density* at object level scale 100; (d) *Standard deviation layer 4* (CASI band #49, 831 nm) at object level scale 500.

Tab. 2: Object features (see Trimble 2012 for details).

Features based on layer values (calculated per input layer)	Features based on object geometry
• Mean	• Area
• Standard deviation	• Border length
• Mean difference to neighbours	• Length
• GLCM (Gray Level Co-occurrence Matrix) homogeneity (all directions)	• Width
	• Density
	• Rectangular fit
	• Roundness
	• Shape index
	• Border index

values of the input layers to be calculated per input layer. The routine is applied for all images, whereas in the case of the hyperspectral datasets only four bands representing the blue, green, red and near-infrared range were considered as input layers in order to reduce data volume and redundancy. The number of object feature layers extracted per image can be obtained from Tab. 3.

To generate segmentation levels, multiresolution segmentation (Baatz & Schäpe 2000) was used. It is a region merging technique which has a scale parameter to control spectral and spatial heterogeneity constraints and thereby also the average objects' size. The definition of scale parameters was only based on a quick visual check without paying particular attention to the segmentation accuracy in terms of meaningful objects that represent geo-objects (Castilla & Hay 2008) which is a time-consuming process. The purpose of the visual check is ensuring that the fine level captures the detailed content of the scene while the coarse level should roughly represent the large structures in the image like crop fields and urban structure types. The finally selected scale parameters can be obtained from Tab. 3. Other segmentation parameters were kept as default (*shape*: 0.1; *compactness*: 0.5*;* equal *layer weights*).

2.4 *Evaluation Procedure*

With six algorithms (Tab. 1) and two input spaces, altogether twelve *algorithm-input space* constellations were empirically tested. Their performance was assessed within a nested cross-validation scheme which repeatedly generates training and test datasets from the available labelled set. This scheme enables the efficient use of typically sparse labelled data and ensures that both train and test sets come from the same distribution (Efron & Tibshirani 1994). The Cohen's kappa coefficient (κ) was used as accuracy measure (Congalton & Green 1999).

The nested approach (Fig. 2) was chosen because some algorithms require some test data for parameter tuning (Tab. 1) and these data instances should not be involved in the actual testing. Referring to Fig. 2, tuning parameters are tested with an inner cross-validation CV_i (5 cycles) that generates its CV_i *train sets* and CV_i *test sets* from the CV_o *train set*. Results of the *l* parameter setting candidates (Tab. 1) are compared and the best setting is used to parameterize a model for training on CV_o *train set* and testing on CV_o *test set* within the outer loop (10 cycles). For validating both the inner and the outer loop k-fold cross-validation was chosen. Only for the ROSIS dataset, where labelled data is plentiful (Tab. 3), 10-times random subsampling was chosen for the outer

Tab. 3: Overview of the experiments.

Case study		Object-based feature extraction		Input space (dimension)		Sample size (labelled pixels)
Mapping task	**Image**	**Segmentation scale range**	**No. of object feature layers**	***Spectral* (no. of bands)**	***Spatial-spectral***	
Building detection	CASI	{20, 100, 500}	75 (25 per level)	72	147	2000
Building detection	Leica RC30	{10, 50, 250}	63 (21 per level)	3	66	2000
Mapping of pools, turf and tree/shrub vegetation	WV-2 Pan	{20, 100, 500}	39 (13 per level)	1	40	2059
Urban land cover classification	ROSIS	{20, 100, 500}	75 (25 per level)	102	177	99,114
Tree species classification	CASI	{20, 100, 500}	75 (25 per level)	72	147	400

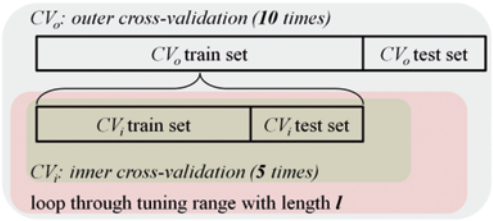

Fig. 2: Nested cross-validation.

loop. This scheme draws in each cycle equally 50 training pixels per class, while the remaining part is for testing.

With respect to data variance, the classification models are trained and tested on the same partitions of the data by passing them in parallel through the nested process. Algorithms without tuning parameters simply skip the inner cross-validation.

3 Results and Discussion

An overview of the results is given by Fig. 3 which shows the distribution of κ coefficients obtained through the ten outer cross-validation cycles. Tab. 4 summarizes the cycles by listing the arithmetic mean. In addition, for each case study the best performing classification model was chosen for the presentation of error matrices and associated overall accuracies (OA) as well as producer's and user's accuracies (Tabs. 5–9). The error matrices were summed up from the outer crossvalidation cycles.

Comparing the results with respect to the input space shows that for all case studies almost all algorithms could benefit from the addition of spatial features. Given a particular algorithm, most improvements are quite distinct, indicated by an increased κ with non-overlapping interquartile ranges (Fig. 3). The less distinct cases with overlapping interquartile ranges concern DT, RF and KNN in conjunction with the CASI-based building detection case study. In contrast, no superiority of one input space over the other was obtained for KNN in conjunction with the WV-2 data which provides the mapping of pools, turf and tree/shrub vegetation. For KNN in conjunction with the RC30-based building detection, the spatial-spectral input space produced even significantly worse result. Overall, a relatively poor performance of the KNN in the spatial-spectral input spaces can be noticed. Possibly, this is because object-based features can have different value ranges which impacts on distance measuring in Euclidian space. In con-

Tab. 4: Cross-validation arithmetic mean (κ). The cell colours are defined by a linear red-to-green gradient which spans per case study from the minimum to the maximum κ value.

Input space	Algorithm	Arithmetic mean (κ)				
		CASI (buildings)	RC30	WV-2	ROSIS	CASI (trees)
Spectral	DT	0.407	0.210	0.559	0.838	0.416
	BAG	0.465	0.250	0.530	0.923	0.525
	RF	0.484	0.230	0.545	0.937	0.499
	SVM rbf	0.531	0.269	0.552	0.964	0.585
	SVM linear	0.420	0.219	0.534	0.964	0.543
	KNN	0.449	0.283	0.492	0.952	0.280
Spatial-spectral	DT	0.496	0.322	0.618	0.934	0.611
	BAG	0.556	0.446	0.719	0.971	0.738
	RF	0.565	0.452	0.717	0.974	0.766
	SVM rbf	0.604	0.535	0.700	0.992	0.703
	SVM linear	0.565	0.477	0.694	0.992	0.684
	KNN	0.478	0.147	0.477	0.970	0.580

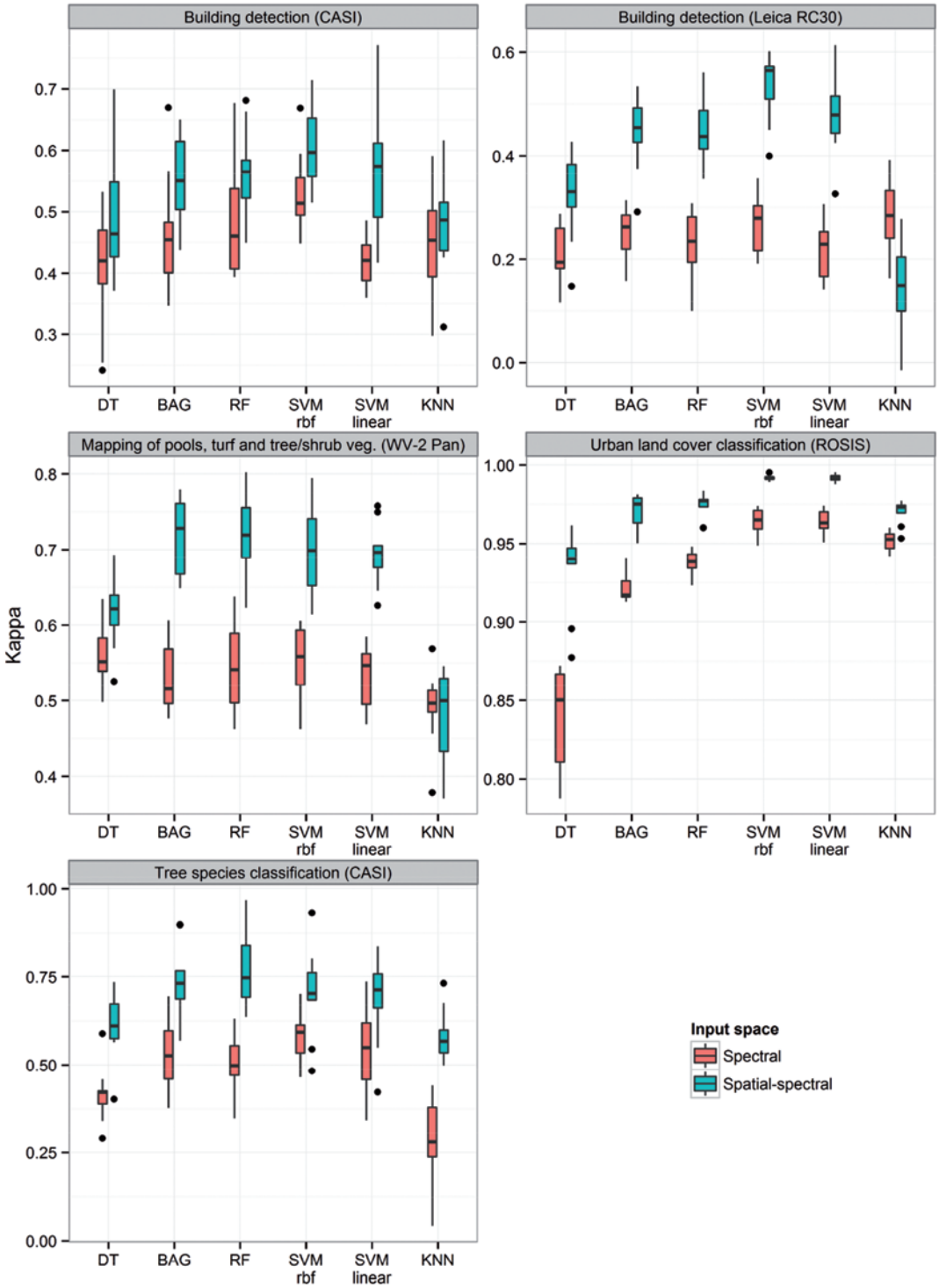

Fig. 3: Cross-validation boxplots (κ). The whiskers extend to the extreme data point which is no more than 1.5 times the interquartile range from the box. The points show outliers.

Tab. 5: Building detection with CASI data (SVM rbf).

Reference	**Roof**	**Background**
Prediction		
Roof	**311**	173
Background	94	**1422**
Producer	76.79	89.15
User	64.26	93.80
Overall	86.65	

Tab. 6: Building detection with RC30 data (SVM rbf).

Reference	**Roof**	**Background**
Prediction		
Roof	**236**	114
Background	169	**1481**
Producer	58.27	92.85
User	67.43	89.76
Overall	85.85	

trast, the results in the spectral input space were competitive with good results for both building detection and the ROSIS-based urban land cover classification case studies.

Comparing the performance of different algorithms in conjunction with the spatial-spectral input space, the results vary across the case studies (Tab. 4). For the CASI-based building detection, SVM rbf achieved the best result (κ 0.604, OA 86.65 %, Tab. 5), followed by SVM linear and RF. The results are encouraging if one takes into account that no additional elevation information, e.g. lidar or stereo models, was used and with respect to the difficult study area which includes heterogeneous, dense urban structures with different land uses and roof types. Possibly, a higher quantity and quality (small positional and thematic mismatch between the roof and the cadastre reference) of training data as well as a postprocessing of the results could improve the results.

For the RC30-based case study, again the SVM rbf algorithm yielded the best results (κ 0.535, OA 85.85 %, Tab. 6), followed by SVM linear and RF.

Other than for the building detection cases, the decision tree ensemble approaches (RF: κ 0.717, BAG: κ 0.719) outperformed the support vector machine approaches (SVM rbf: κ 0.700, SVM linear: κ 0.694) for the mapping of *pools*, *turf* and *trees/shrubs* with panchromatic WV-2 data. The error matrix (Tab. 7) shows high producer's and user's accuracies (> 83 %) for *pools* and *trees/shrubs*, but lower producer's accuracy (65.75 %) for *turf* which is in particular due to confusion with the *background* class. Possibly, paved areas like parking lots show similar geometrical and textural properties and cannot be differentiated by the limited spectral information. In this context, much improvement could be expected from the the inclusion of the eight multispectral bands of WV-2 (Wolf et al. 2012).

Tab. 7: Mapping of pools, turf and trees/shrubs with WV-2 data (BAG).

Reference	**Pool**	**Turf grass**	**Tree/ Shrub**	**Back-ground**
Prediction				
Pool	**36**	0	2	3
Turf grass	0	**144**	5	21
Tree/shrub	4	7	**684**	129
Background	2	68	102	**852**
Producer	85.71	65.75	86.25	84.78
User	87.80	84.71	83.01	83.20
Overall	83.34			

For the ROSIS-based application, the nine urban land cover classes have been best predicted by SVM rbf and SVM linear, achieving particular high agreement with the reference (both κ 0.992). However, true mapping accuracy can be expected to be much lower due to the non-random clustered distribution of the reference, which does not represent the image in its entirety. In comparison to the previous research on this benchmarking dataset (Palmason et al. 2005, Tarabalka et al. 2010), the obtained results show an improvement in terms of OA and producer's/user's accuracies (Tab. 8).

The classification of urban tree species using hyperspectral data was best achieved by RF (κ 0.766, OA 82.25 %). The producer's accuracies range from 72 % (*Acer platanoides*) to 100 % (*Tilia tomentosa*) and the user's accuracies from 41 % (*Crataegus x lavallei*) to 92 % (*Acer pseudoplatanus*) (Tab. 9).

Summarizing the algorithm performances, it can be noted that support vector machine as well as tree ensemble approaches provided reliable solutions even for quite diverse mapping scenarios (in terms of sensors, classes and labelled information), whereas decision tree and nearest neighbour were not competitive. This strengthens the statements of previous research studies reporting on good performances of support vector machine and random forest approaches for high dimensional problems (Duro et al. 2012, Huang et al. 2002, Waske et al. 2009). Comparing both tree ensemble methods, RF achieved in four of five case studies the higher κ. The difference is only marginal, but aligns with Breiman (2001) who states the theoretical and empirical superiority of RF. Among the support vector machine kernels, rbf provided better results in four of five case studies.

Tab. 8: Urban land cover classification with ROSIS data (SVM rbf).

Reference	**Water**	**Trees**	**Asphalt**	**Bricks**	**Bitumen**	**Tiles**	**Shadows**	**Meadows**	**Soil**
Prediction									
Water	**465272**	0	0	0	0	0	0	0	0
Trees	0	**35560**	302	0	2	0	0	5	2
Asphalt	0	1848	**12944**	0	122	0	0	0	0
Bricks	0	0	0	**25320**	71	256	23	289	0
Bitumen	0	0	17	6	**49710**	57	0	15	0
Tiles	0	0	0	12	0	**57935**	0	827	0
Shadows	414	0	0	23	3	17	**34266**	14	0
Meadows	0	0	27	19	2	15	0	**282211**	0
Soil	14	2	0	0	0	0	1	19	18998
Producer	99.91	95.05	97.40	99.76	99.60	99.41	99.93	99.59	99.99
User	100.00	99.14	86.79	97.54	99.81	98.57	98.64	99.98	99.88
Overall	99.55								

Tab. 9: Urban tree species classification with CASI data (RF).

Reference	**Ac. pl.**	**Ac. ps.**	**Ac. sa.**	**Ae. ca.**	**Be. pe.**	**Cr. la.**	**Pl. ac.**	**Ti. to.**
Prediction								
Acer platanoides	**18**	10	0	0	0	0	0	0
Acer pseudoplatanus	5	**159**	2	1	3	1	0	0
Acer saccharinum	0	6	**36**	0	0	0	1	0
Aesculus carnea	0	9	0	**24**	0	0	0	0
Betula pendula	0	7	0	0	**22**	0	0	0
Crataegus lavallei	0	10	0	0	0	**7**	0	0
Platanus acererifolia	2	8	0	0	1	0	**29**	0
Tilia tomentosa	0	3	1	0	1	0	0	**34**
Producer	72.00	75.00	92.31	96.00	81.48	87.50	96.67	100.00
User	64.29	92.98	83.72	72.73	75.86	41.18	72.50	87.18
Overall	82.25							

4 Summary and Conclusion

Comparing different machine learning algorithms, the value of adding objects-based features into per-pixel classification was investigated using different urban remote sensing case studies. Based on the experimental results it can be concluded that the addition of these features can improve the classification performance if combined with an appropriate learning algorithm. Especially support vector machines and decision tree ensemble approaches performed well in this context. Moreover, this work presents a framework in which object-based features are accessed on the pixel domain. This can be an advantage for the application of machine learning with respect to unbiased data representation. Moreover, it can be taken into account as an alternative, straightforward option if an integration of the pixel and the object domain is intended, e.g. in case of Tarabalka et al. (2009) and Wang et al. (2004).

Acknowledgement

The author would like to thank Prof. Paolo Gamba of the University of Pavia, Italy, for providing the ROSIS image data along with the labelled reference information.

References

Baatz, M. & Schäpe, A., 1999: Object-Oriented and Multi-Scale Image Analysis in Semantic Networks. – 2nd International Symposium: Operationalization of Remote Sensing, 16–20 August, ITC, Niederlande.

Baatz, M. & Schäpe, A., 2000: Multiresolution segmentation: an optimization approach for high quality multi-scale image segmentation. – Angewandte Geographische Informationsverarbeitung **XII**: 12–23.

Benz, U.C., Hofmann, P., Willhauck, G., Lingenfelder, I. & Heynen, M., 2004: Multi-resolution, object-oriented fuzzy analysis of remote sensing data for GIS-ready information. – ISPRS Journal of Photogrammetry and Remote Sensing **58** (3–4): 239–258.

Blaschke, T., Lang, S. & Hay, G.J., 2008: Object-based image analysis. – 817 p., Springer, Berlin.

Blaschke, T., 2010: Object based image analysis for remote sensing. – ISPRS Journal of Photogrammetry and Remote Sensing **65** (1): 2–16.

Breiman, L., Friedmann, J.H., Olshen, R.A. & Stone, C.J., 1984: Classification and regression trees. – Chapman & Hall, New York, USA.

Breiman, L., 1996: Bagging predictors. – Machine Learning **24** (2): 123–140, New York, USA.

Breiman, L., 2001: Random Forests. – Machine Learning **45** (1): 5–32.

Burges, C.J., 1998: A Tutorial on Support Vector Machines for Pattern Recognition. – Data Mining and Knowledge Discovery **2** (2): 121–167.

Burnett, C. & Blaschke, T., 2003: A multi-scale segmentation/object relationship modelling methodology for landscape analysis. – Ecological Modelling **168** (3): 233–249.

Castilla, G. & Hay, G.J., 2008: Image objects and geographic objects. – Blaschke, T., Lang, S. & Hay, G.J. (eds.): Object-Based Image Analysis. Spatial Concepts for Knowledge-Driven Remote Sensing Applications: 91–110, Springer-Verlag, Berlin.

Congalton, R.G. & Green, K., 1999: Assessing the accuracy of remotely sensed data. – Lewis Publications, Boca Raton, USA.

Duro, D.C., Franklin, S.E. & Dubé, M.G., 2012: A comparison of pixel-based and object-based image analysis with selected machine learning algorithms for the classification of agricultural landscapes using SPOT-5 HRG imagery. – Remote Sensing of Environment **118:** 259–272.

Efron, B. & Tibshirani, R., 1994: An introduction to the bootstrap. – 436 p., Chapman & Hall, New York, USA.

Herold, M., Gardner, M. & Roberts, D.A., 2003: Spectral resolution requirements for mapping urban areas. – IEEE Transactions on Geoscience and Remote Sensing **41** (9): 1907–1919.

Hof, A. & Schmitt, T., 2011: Urban and tourist land use patterns and water consumption: Evidence from Mallorca, Balearic Islands. – Land Use Policy **28** (4): 792–804.

Ho, T.K., 1998: The random subspace method for constructing decision forests. – IEEE Transactions on Pattern Analysis and Machine Intelligence **20** (8): 832–844.

Huang, C., Davis, L.S. & Townshend, J.R.G., 2002: An assessment of support vector machines for land cover classification. – International Journal of Remote Sensing **23** (4): 725–749.

Karatzoglou, A., Smola, A., Hornik, K. & Zeileis, A., 2004: kernlab – An S4 Package for Kernel Methods in R. – Journal of Statistical Software **11** (9): 1–20.

Lu, D. & Weng, Q., 2007: A survey of image classification methods and techniques for improving

classification performance. – International Journal of Remote Sensing **28** (5): 823–870.

Novack, T., Esch, T., Kux, H.J.H. & Stilla, U., 2011: Machine Learning Comparison between WorldView-2 and QuickBird-2-Simulated Imagery Regarding Object-Based Urban Land Cover Classification. – Remote Sensing **3** (10): 2263–2282.

Palmason, J., Benediktsson, J.A., Sveinsson, J. & Chanussot, J., 2005: Classification of hyperspectral data from urban areas using morphological preprocessing and independent component analysis. – IEEE International Geoscience and Remote Sensing Symposium: 176–179.

R Core Team, 2012: R: A Language and Environment for Statistical Computing. – http://www.R-project.org (4.11.2012).

Schölkopf, B. & Smola, A.J., 2002: Learning with kernels. – MIT Press, Cambridge, Massachusetts, USA.

Stehman, S.V. & Czaplewski, R.L., 1998: Design and Analysis for Thematic Map Accuracy Assessment. – Remote Sensing of Environment **64** (3): 331–344.

Svetnik, V., Liaw, A., Tong, C., Culberson, J., Sheridan, R. & Feuston, B., 2003: Random Forest: A Classification and Regression Tool for Compound Classification and QSAR Modeling. – Journal of Chemical Information and Modeling **43** (6): 1947–1958.

Tarabalka, Y., Benediktsson, J.A. & Chanussot, J., 2009: Spectral-Spatial Classification of Hyperspectral Imagery Based on Partitional Clustering Techniques. – IEEE Transactions on Geoscience and Remote Sensing **47** (8): 2973–2987.

Tarabalka, Y., Fauvel, M., Chanussot, J. & Benediktsson, J.A., 2010: SVM- and MRF-Based Method for Accurate Classification of Hyperspectral Images. – IEEE Geoscience and Remote Sensing Letters **7** (4): 736–740.

Therneau, T.M. & Atkinson, E.J., 1997: An introduction to recursive partitioning using the rpart routines. – http://mayoresearch.mayo.edu/mayo/research/biostat/upload/61.pdf (13.11.2012).

Trimble, 2012: eCognition® Developer 8.8. Reference Book. – Trimble Germany GmbH.

Vapnik, V.N., 1998: Statistical learning theory. – Wiley, New York, USA.

Venables, W.N. & Ripley, B.D., 2002: Modern Applied Statistics with S. – **4th** ed., Springer, New York, USA.

Wang, L., Sousa, W.P. & Gong, P., 2004: Integration of object-based and pixel-based classification for mapping mangroves with IKONOS imagery. – International Journal of Remote Sensing **25** (24): 5655–5668.

Waske, B., Benediktsson, J.A., Árnason, K. & Sveinsson, J.R., 2009: Mapping of hyperspectral AVIRIS data using machine-learning algorithms. – Canadian Journal of Remote Sensing **35** (S1): 106–116.

Wolf, N., Hof, A. & Jürgens, C., 2012: Machine learning for the exhaustive evaluation of object-based feature spaces. – GEOBIA **2012:** 267–272.

Address of the Author:

M.Sc. Geography Nils Wolf, Ruhr-Universität Bochum, Geographisches Institut, D-44801 Bochum, Germany, Tel.: +49-234-32-23380, Fax: +49-234-32-14180, e-mail: nils.wolf@rub.de

Manuskript eingereicht: November 2012
Angenommen: März 2013

PFG 2013 / 3, 0163 – 0172
Stuttgart, June 2013

Article

Multisensorale, objektbasierte und GIS gestützte Klassifizierung von Grünlandbiotoptypen im Biosphärengebiet Schwäbische Alb

Patric Schlager, Tübingen, Alfons Krismann, Singen, Kathrin Wiedmann, Heiko Hiltscher, Hohenheim, Volker Hochschild, Tübingen & Klaus Schmieder, Hohenheim

Keywords: Biotopkartierung, Sekundärdaten, Orthophotos, RapidEye, Lidar

Zusammenfassung: Seit den 1990er Jahren werden Fernerkundungssysteme zur Biotoptypenklassifizierung eingesetzt. Zeitgleich wuchs der Bedarf nach aktuellen und hochaufgelösten räumlichen Daten über den Zustand und das Vorkommen wertvoller Habitatstrukturen im Zuge nationaler und internationaler Naturschutzvereinbarungen (NATURA2000 2002, CBD 1992).

Eine automatisierte Biotoptypeninterpretation wurde bislang nur selten bis zur Praxistauglichkeit entwickelt. Probleme ergeben sich bei der Übertragung von Klassifizierungsalgorithmen auf andere Gebiete oder bei der erreichten Klassifizierungstiefe.

Im Rahmen des Projektes „Flächendeckende Biotop- und Nutzungstypenkartierung im Biosphärengebiet Schwäbische Alb mittels Fernerkundungsdaten als Basis für ein Landschaftsmonitoring“ wird eine flächendeckende Biotoptypenkartierung für das Biosphärengebiet Schwäbische Alb durchgeführt. Verwendet werden hierfür multisensorale Fernerkundungsquellen (Orthophotos, RapidEye, Lidar, TerraSAR-X) und vektorielle Daten, vor allem Geobasisdaten aus der amtlichen Katasterverwaltung, des Agrarkontrollsystems InVeKoS, sowie Umweltdaten, wie Lebensraumtyp- und Biotoptypkartierungen.

Ausgangspunkt war die Verschneidung aller GIS-Daten zu einer flächendeckenden Objektkarte, die dann für Objektarten mit geringer Güte, z. B. Acker- Grünlanddifferenzierung, oder grober Klassifizierungstiefe als Segmentgrenzen für eine objektorientierte Segmentierung und Klassifizierung mittels eCognition 8.64 zur Differenzierung der übrigen Biotoptypen verwendet wurde. Biotoptypen mit dreidimensionalen Merkmalen (Schilf, Röhricht etc.) wurden regelbasiert aus den Lidar-Daten extrahiert und automatisch klassifiziert.

Summary: *Multisensoral, object- and GIS-based classification of grassland habitats in the Biosphere Reserve Schwäbische Alb.* Remote sensing of habitat complexes dates back into the 1990ies and has been continuously improved. At the same time the demand for spatially and temporally precise datasets has become urgent, due to international agreements like the NATURA 2000 and the CBD (NATURA2000 2002, CBD 1992).

Automatically derived habitat complexes which realize an appropriate level of relevance for end users was only seldomly achieved. Problems evolve with the transferability of algorithms to other sites or scenes as well as with the classification depths and accuracy.

Within the project „Flächendeckende Biotop- und Nutzungstypenkartierung im Biosphärengebiet Schwäbische Alb mittels Fernerkundungsdaten als Basis für ein Landschaftsmonitoring“ an area-wide classification of habitat complexes of the Biosphere Reserve Schwäbische Alb has been conducted.

The classification is based on multisensoral remote sensing datasets (Orthophotos, RapidEye, lidar, TerraSAR-X) and on vector data, mainly geodata sets of the cadastral land register and the agrarian control system InVeKoS. Additionally, environmental geodata sets like habitat mapping were used. The GIS data was merged to a thematic consistent pre-classification scheme that was used to further classify habitat complexes based on spectral and three dimensional attributes. Later, an object based image classification approach with image segmentation and rule based classification has been conducted and provided for the final classification. Three dimensional habitat complexes like reed were extracted from the lidar data.

 www.schweizerbart.de
DOI: 10.1127/1432-8364/2013/0167 1432-8364/13/0167 $ 2.50

1 Einleitung

Die Bedeutung der Erfassung und Bewertung von Biotoptypen wächst mit zunehmendem Landschaftswandel und fortschreitendem Artenverlust zusehends. Biotoptypenkartierungen nehmen nicht zuletzt auch für die Überwachung der Einhaltung von nationalen und internationalen Naturschutzvereinbarungen wie der FFH-Richtlinie und des Biodiversitätskonvention (CBD = Convention on Biological Diversity) eine wichtige Rolle ein (Mander et al. 2005, Frick 2006). Im Rahmen des Monitorings für diese Vereinbarungen sind stets aktuelle Daten über die Art, Lage und Verbreitung sowie die Häufigkeit und den Zustand der Biotoptypen in einem Lebensraum nötig (Brand et al. 2002, Kim 2007). Seit den 1990ern wurden verschiedene Fernerkundungsverfahren zur Biotoptypenbestimmung entwickelt (Brand et al. 2002, Bock 2003, Frick 2006, Tiede et al. 2008). Überwiegend wurden objektorientierte Klassifizierungsverfahren eingesetzt, mit denen genauere Ergebnisse als mit pixelbasierten Verfahren erreicht werden konnten (Bock et al. 2005).

Objektorientierte Klassifizierungsverfahren (GEOBIA = geographic object-based image analysis) stützen sich auf die zwei methodischen Säulen der Segmentierung und Klassifizierung (Lang 2008). Bei der Segmentierung werden benachbarte Pixel auf Grund von Ähnlichkeiten zu Pixelgruppen, sogenannten „*meaningful objects*“, zusammengefasst (Neubert 2005). Diese Objekte lassen sich anhand ihrer spektralen Eigenschaften klassifizieren. Darüber hinaus lassen sich Texturparameter objektweise berechnen und gleichzeitig Formeigenschaften und Nachbarschaftsbeziehungen für die Klassifizierung verwenden. Zusätzlich kann das Klassifizierungsverfahren durch die Einbindung von Sekundärdaten, z. B. des Liegenschaftskatasters, unterstützt werden.

Bei einer Segmentierung und Klassifizierung mit der überwiegend verwendeten Analysesoftware eCognition konnte Dietsche (2007) zeigen, dass die geometrische Abgrenzung der Objekttypen der softwaregestützten Segmentierung deutlich genauer als die durch Geländekartierer erstellte generalisierte FFH- und Biotop- und Nutzungstypenkarte ist. Trotz der großen Fortschritte bei der fernerkundungsbasierten Klassifizierung von Biotoptypen kann der Bedarf der Naturschutzverwaltung an zeitlich und räumlich hochaufgelösten Biotoptypenklassifizierungen mit einer für die Anwendung brauchbaren thematischen Tiefe und Genauigkeit bis hin zur Rechtssicherheit z. B. des FFH-Lebensraumtyps 6510 (Magere Flachland-Mähwiese) bislang nicht erfüllt werden. Oft ist die Klassifizierung als „Potentialfläche“ nach Franke et al. (2012) möglich. Das sind Flächen, die mit relativ hoher Güte als Mähwiesen klassifiziert werden konnten, aber noch einer Verifizierung im Gelände bedürfen. Als problematisch erweist sich häufig neben der geringen thematischen Tiefe und mangelnden Übertragbarkeit von Algorithmen auf andere Gebiete die ausschließliche Verfügbarkeit von monotemporalen Datensätzen, die keine Beobachtung über die zeitliche Entwicklung der Phänologie zulassen. Tiede et al. (2008) verfolgte in diesem Zusammenhang den Ansatz, bei großen Unsicherheiten der Klassifizierung einen fachkundigen Nutzer in den Entscheidungsprozess einzubeziehen, indem dieser über ein *graphical user interface* die Möglichkeit bekommt, die Klassenzuweisung und Aggregation von Objekten zu unterstützen. Die Datenbereitstellung durch die RapidEye Mission mit Wiederholungsraten von bis zu 14 Tagen eröffnet hier neue Möglichkeiten. Die Möglichkeiten zur Kartierung von Vegetationseinheiten mit multitemporalen RapidEye Daten wurden beispielsweise von Förster et al. (2011) untersucht.

Im Rahmen des Projektes „Flächendeckende Biotop- und Nutzungstypenkartierung im Biosphärengebiet Schwäbische Alb mittels Fernerkundungsdaten als Basis für ein Landschaftsmonitoring“ wird das Ziel verfolgt, eine flächendeckende Biotoptypenerfassung für das Biosphärengebiet Schwäbische Alb auf der Grundlage des Biotoptypen-Kartierschlüssels der Landesanstalt für Umwelt, Messungen & Naturschutz Baden-Württemberg (LUBW 2009) zu erstellen.

Dabei wird ein innovativer Ansatz verfolgt, der sich einerseits auf multisensorale Fernerkundungsquellen (Orthophotos, RapidEye, Lidar und explorativ TerraSAR-X) und andererseits auf amtliche vektoriellen Geobasisda-

ten stützt. Dies sind vor allem GIS-Daten wie die Angaben der landwirtschaftlichen Betriebe im „Gemeinsamen Antrag“ (GA 2013), das Amtliche Topographisch-Kartographische Informationssystem (ATKIS), das Forstliche Geo-Informations-Systems (FoGIS, SCHLÜTER 2011), NATURA 2000-Lebensraum- (LRT) & Biotopkartierungen und Landschaftspflegeflächen, im Folgenden „GIS-Geodatenbasis“ genannt (s. Abschnitt 2.1), die im Sinne einer Vorklassifizierung die Segmentierung entscheidend verbessern können. Die erarbeiteten Daten dienen als Planungsgrundlage sowie als Basis für ein langfristiges Monitoring der Landschaftsdynamik im Biosphärengebiet.

2 Material und Methoden

Das Biosphärengebiet Schwäbische Alb deckt eine Fläche von 85.269 ha der Schwäbischen Alb ab. 3,1 % des Gebietes sind als Kernzone, 41,8 % als Pflegezone und 55,4 % als Entwicklungszone ausgewiesen. Charakteristische und wertvolle Biotoptypen der Schwäbischen Alb sind beispielsweise die Wacholderheiden, die Magerrasen basenreicher Standorte oder die Streuobstgebiete, während nasse und/oder saure Standortbedingungen auf Grund der Geologie eher selten vorkommen.

Das Gebiet wurde im Jahr 2010 vollständig mit einer digitalen Kamera UltraCamXP beflogen, so dass Orthophotos in RGB und IR mit einer Auflösung von 20 cm und einer Datentiefe von 8 Bit vorliegen. Zusätzlich wurden alle in den Jahren 2010 und 2011 verfügbaren RapidEye-Satellitendaten (6,5 m Bodenauflösung, Level 3A) hinzugezogen. Für

Abb. 1: Schematische Darstellung des workflows für die Grünlandklassifizierung.

eine vollständige Abdeckung des Gebiets mit RapidEye Szenen werden 7 Kacheln benötigt. Während im Jahre 2010 nur für einen Termin wolkenfreie Aufnahmen vorlagen, standen für 2011 fünf Aufnahmetermine zur Verfügung, die das Gebiet nahezu vollständig abdecken und wolkenfrei sind. Die Daten wurden am 18.04., 26.06., 02.08., 22.08. und 10.09. aufgenommen.

Neben den optischen Fernerkundungssystemen wurden die Lidar-Daten des Landes Baden-Württemberg von 2002 für die Extraktion von Gehölztypen und hochwachsenden Pflanzen feuchter Standorte herangezogen. Die Daten liegen mit einer Punktdichte von 1 Punkt/m^2 vor.

Die verwendeten Sekundärdaten (GIS-Geodatenbasis, siehe Abschnitt 1) stammen aus den Jahren 2009 und 2010. Die zum Abgleich verwendeten Kartierungen der geschützten Biotope stammen aus den 90er Jahren und von 2011.

Zusätzlich wurde im Jahre 2010 eine gezielte Kartierung von Trainings- und Evaluierungsdaten im Gelände durchgeführt, bei denen alle im Biosphärengebiet vorkommenden Biotoptypen in 710 Einzelpolygonen mit insgesamt rund 800 ha Fläche erfasst wurden. Für einzelne Klassen erfolgten zusätzliche Geländekartierungen in den Jahren 2011 und 2012.

Der Kartierschlüssel der LUBW (2009) gliedert sich in vier hierarchische Ebenen, die je nach betrachteter Ebene eine feinere Aufschlüsselung und Betrachtung des Biotoptyps vornehmen. Die sechs Typen der ersten Ebene sind folgende: 1. Gewässer, 2. Terrestrisch-morphologische Biotoptypen, 3. Gehölzarme terrestrische und semiterrestrische Biotoptypen, 4. Gehölzbestände und Gebüsche, 5. Wälder, 6. Biotoptypen der Siedlungs- und Infrastrukturflächen. Daraus ergeben sich auf der 4. Ebene 281 Biotoptypen.

Schematisch lässt sich der *workflow* der Grünlandklassifizierung folgendermaßen gliedern:

2.1 *GIS-Daten*

In der objektorientierten Bildanalyse ist die Verwendung von Sekundärdaten konzep-

tionell angelegt. eCognition bietet daher die Möglichkeit, Sekundärdaten in den Segmentierungs- und Klassifizierungsprozess einzubeziehen. Auf Grund der unter 1. geschilderten Problematik bei der Ableitung von Biotoptypen aus Fernerkundungsdaten und der Gebietsgröße wurde aus den unter 2. erwähnten GIS-Daten (Terrestrisch-morphologische Biotoptypen) in einem iterativen Prozess eine einheitliche Maske für das Untersuchungsgebiet erstellt, die Objektgruppen, z. B. Wald, Grünland etc., von anderen Objektgruppen beziehungsweise bereits bekannten Biotoptypen, z. B. Acker, trennt. Dadurch konnte für schwer zu trennende Biotoptypen, z. B. Wirtschaftswiesen und beweidete Grünlandflächen, eine Vorabgrenzung vorgenommen werden.

Die Erstellung der Maske erfolgte in sechs aufeinander aufbauenden Prozessschritten.

1. Vom ATKIS-BasisDLM (Basis Digitales Landschaftsmodell) wurden 75 Objekttypen in 119 Einzelschritten mit ArcGIS 10 einheitlich aufbereitet, wobei der Schwerpunkt auf der Offenland/Waldabgrenzung und dem Siedlungs- und Gebäudebereich lag. Darüber hinaus wurden gehölzreiche Grünlandbestände aus den Siedlungen entfernt. Hierbei handelt es sich vorwiegend um Streuobstwiesen. Das ATKIS-Basis-DLM lag damals für Baden-Württemberg zersplittert in 429 einzelnen Shape-Dateien (Blattschnitten) vor. Mittlerweile wurden diese Einzeldateien seitens der zuständigen Behörde zu größeren Einheiten aggregiert.
2. Die FFH-Mähwiesenkartierung von 2004 und 2010 wurde kombiniert und in das BasisDLM eingefügt.
3. Die landwirtschaftlichen GA-Daten wurden mittels der Flurstücksnummer mit der Automatisierten Liegenschaftskarte (ALK) verbunden. Für das Gesamtgebiet wurden etwa 48.000 Flurstücke verwendet. Es wurden nur Flurstücke berücksichtigt, bei denen der einheitliche Flächenanteil im GA mindestens 80 % betrug, d. h. die Information von Flurstücken mit mehreren landwirtschaftlichen Schlägen unterschiedlicher Nutzung konnte prinzipiell nicht verwendet werden. Auf diese Weise konnten ca. 90 % der Ackerflächen abgeleitet werden, die auch bei unterschiedlicher Nutzung einen einheitlichen Biotoptyp darstellen.
4. Neben den Ackerflächen wurde aus den GA-Daten das naturschutzfachlich wertgebende Grünland („Artenreiches Grünland“, in Baden-Württemberg eine förderfähige Agrarumweltmaßnahme des MEKA-Programmes (MEKA 2013)) sowie die beweideten Flächen gefiltert.
5. Aus der Forstinventur wurden nach einem Bereinigungsschritt 6721 Flächen übernommen.
6. Aus den Landschaftspflegeverträgen wurden 131 Flächen übernommen, verteilt auf drei Landkreise. Dabei handelt es sich vor allem um Sommerschafweiden.

Nach Abschluss der sechs Prozessierungsschritte, wurden die Daten zu einem einheitlichen Landnutzungslayer verschnitten, wobei keine Polygone < 200 m² zugelassen bzw. mittels der ArcGIS-Erweiterung ET Geowizards 10.1 (www.ian-ko.com) zu Nachbarflächen

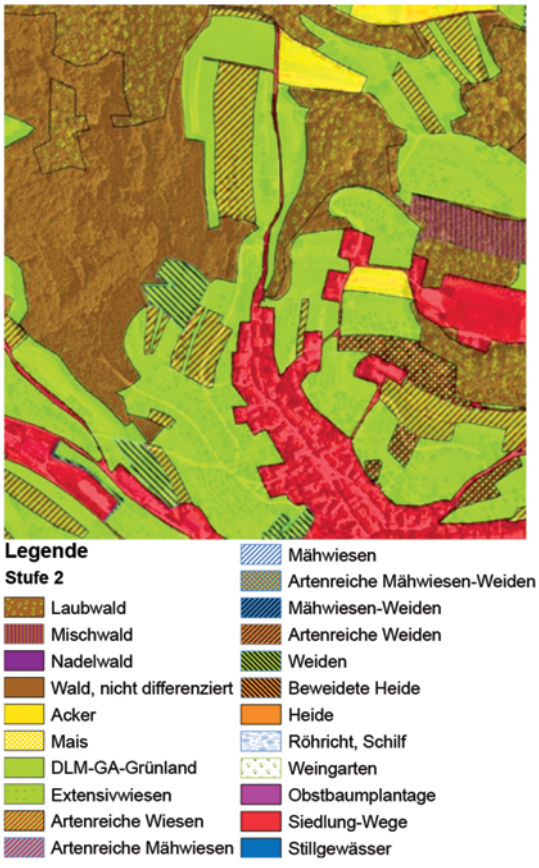

Abb. 2: Ausschnitt des Landnutzungslayers in der Detaillierungsstufe 2 mit zugehöriger Legende.

mit der längsten gemeinsamen Grenzen aggregiert wurden. Der Landnutzungslayer wurde in drei unterschiedlichen Detaillierungsgraden erstellt, um im Rahmen der Klassifizierung unterschiedliche Strategien testen zu können.

2.2 *Klassifizierung der spektralen Daten*

Mittels der Klassifizierung der spektralen Fernerkundungsdaten wurde das Ziel verfolgt, folgende Grünlandbiotoptypen zu klassifizieren: *Feuchtwiesen* (33.10), *Nasswiese* (33.20), *Schilf* (34.40), *Röhricht* (34.50), *Großseggenriede* (34.60), *Dominanzbestände* (35.30), *Hochstaudenfluren* (35.40), *Intensivgrünland* oder *Grünlandansaat* (33.60) und *Magerrasen basenreicher Standorte* (33.60). Zusätzlich wurden die *Wirtschaftswiesen mittlerer Standorte* (33.40) und die *Weiden mittlerer Standorte* (33.50) berücksichtigt. Allerdings war für die Ableitung dieser Klassen keine spektrale Klassifizierung notwendig, da sich die Wirtschaftswiesen als Restsumme aus dem Gesamtgrünland nach Abzug der anderen Grünlandtypen ergaben und die Weiden bereits durch die Erstellung des Landnutzungslayers erkannt waren.

Für die Klassifizierung wurden einerseits die in 30 Einzelkacheln vorliegenden RapidEye-Daten und andererseits die Orthophotos genutzt. Die RapidEye-Daten wurden einer Atmosphärenkorrektur unterzogen und anschließend zu fünf einheitlichen Bildmosaiken aufbereitet (Abb. 3). Die Orthophotos wurden in 4 x 1404 Einzeldateien geliefert und mussten zunächst zu *composites* gerechnet und anschließend mosaikiert werden. Durch das Mosaikieren wurden radiometrische Unterschiede in den Daten ausgeglichen.

Die Klassifizierung erfolgte in mehreren aufeinander aufbauenden Prozessierungsschritten. Zunächst wurden alle für die angestrebte Zielklasse relevanten Ausgangsklassen aus dem Landnutzungslayer ausgewählt und als Segmentierungsgrundlage in eCognition zugrunde gelegt (Level 1). Ausgehend davon wurde mittels einer *multiresolution segmentation* ein zweites Segmentierungslevel erstellt, das über die Funktion *relations to super objects* mit den in Level 1 eingegangenen Landnutzungslayer verbunden wurde. Dadurch standen die Ausgangsklassen auch auf Level 2 zur Verfügung. Innerhalb dieser noch relativ großen und unspezifischen Segmente wurden dann *geons*, d. h. Zielobjekte mit thematisch und geometrisch adäquater Auflösung, adressiert.

Bei der Klassifizierung wurden einerseits auf Fuzzy-Logik basierende Klassenbeschreibungen und die Definition von Zugehörigkeitsfunktionen verwendet und andererseits Schwellenwertfestlegungen. Die Definition von Objektbeziehungen diente dazu, die unterschiedlichen Segmentierungslevel miteinander zu verbinden und Nachbarobjekte zu fusionieren.

2.2.1 Feuchtflächen

Aufgrund der naturräumlich bedingten geringen Zahl von Feuchtflächen wurden diese in nur zwei Klassen aggregiert: Röhricht und Schilf sowie Nasswiesen, Dominanzbestände, Großseggenriede und Hochstaudenfluren. Ausgangspunkt für die Klassifizierung bildeten die im Landnutzungslayer definierten Klassen DLM-GA-Grünland. Die DLM-GA-Grünland enthält Grünland, das im Gemeinsamen Antrag und im BasisDLM nicht näher bestimmt ist, sowie Röhricht/Schilf, um Veränderungen gegenüber den bestehenden ATKIS Daten dokumentieren zu können. Diese

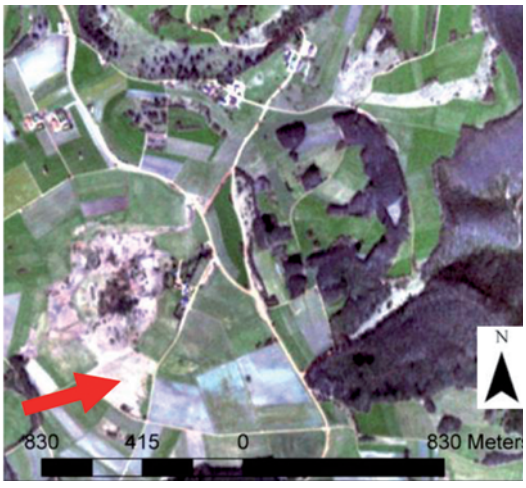

Abb. 3: Ausschnitt des RapidEye-Mosaiks vom 18.04.2011. Deutlich erkennbar sind die feuchten Bereiche (siehe Pfeil).

Daten wurden als Segmentierungsgrundlage für die RapidEye-Szene vom 18.04.2011 herangezogen.

Zu diesem frühen Aufnahmezeitpunkt war der Aufwuchs auf den feuchten Flächen noch kaum entwickelt, wodurch sich die Flächen zu den deutlich weiter entwickelten Wirtschaftswiesen spektral unterschieden (Abb. 2). Eine Trennung der feuchten und intensiver bewirtschafteten Flächen erfolgte mittels der Definition von Zugehörigkeitsfunktionen.

Anschließend wurde das Klassifizierungsergebnis als Segmentierungsgrundlage für die Klassifizierung der Orthophotos verwendet, für die eine eigene Segmentierung erstellt wurde. Mittels der Ableitung von Texturen erfolgte eine Trennung der fehlklassifizierten Wirtschaftswiesen, so dass im Anschluss eine Feuchtklasse verblieb, die mit Hilfe der Lidar-Daten weiter klassifiziert wurde. Aus den Lidar-Daten wurde ein in Bezug zur Geländehöhe „Normalisiertes Oberflächenmodell" berechnet. D. h., es wurden alle First- und Last-pulse-Reflexionen unterhalb von 1 m entfernt, so dass in dem Datensatz lediglich Punkte verblieben, die Gehölze oder andere potentielle Objekte mit dreidimensionalem Charakter repräsentieren. Aus diesem Datensatz wurden einerseits mittels der eigens entwickelten Software „Biomass" Offenlandgehölze klassifiziert (Krismann et al. 2012) und andererseits Röhricht und Schilfbestände. Neben der Ableitung der Objektgeometrien wurden objektweise mehrere Attribute wie die mittlere Höhe, das Längen- und Breitenverhältnis und anderes berechnet.

Die Ableitung der Schilf- und Röhrichtflächen erfolgte mittels der Kombination unterschiedlicher Attribute, z. B. mittlere Höhe $< 2{,}5$ m und Fläche < 500 m^2, sowie einer zusätzlichen Trennung von kleinen Gebüschen und Hochstauden anhand von relativen einzelflächenspezifischen NDVI-Schwellenwerten. Konkret: Wenn der mittlere NDVI eines Einzelobjektes (Gebüsch oder Hochstaudenpatch) mehr als 15 % unter dem des mittleren NDVI der gesamten Feuchtfläche oder mindestens ein Pixel (20 cm x 20 cm) mehr als 60 % unter dem des mittleren NDVI liegt, wurde das Objekt als kleines Gebüsch klassifiziert. Diese Schwellenwerte sind je nach Befliegungszeitpunkt anzupassen.

Bei der Entwicklung des Feuchtgebiets-Klassifizierungsschlüssels wurde auch auf Gebiete außerhalb des Biosphärengebiets zurückgegriffen (Bodenseeregion), da die wenigen Feuchtflächen der Schwäbischen Alb keine verlässliche Algorithmenentwicklung erlaubt hätten.

2.2.2 Intensivgrünland oder Grünlandansaat

Bei der Klasse Intensivgrünland handelt es sich um Grünlandstandorte, die vier- bis fünfmal im Jahr gemäht und stark gedüngt werden. Die Flächen werden von wenigen Arten, z. B. Klee und Weidelgras, dominiert. Spektral sind die Flächen bei einer monotemporalen Szene nur selten von Wirtschaftswiesen zu unterscheiden. Daher wurde als ausschlaggebendes Klassifizierungsmerkmal die Schnitthäufigkeit herangezogen, die aus den RapidEye-Mosaiken abgeleitet wurde.

Zunächst wurde das im Nutzungslayer nicht näher differenzierte Grünland mittels eCognition 8.64 auf Basis der RapidEye Mosaike segmentiert. Die Klassifizierung gemähter und ungemähter Flächen erfolgte für die RapidEye Mosaike vom 26.06.2011 – 10.09.2011. Als Klassifizierungsmerkmal wurden Klassenbeschreibungen erstellt, die sich im Wesent-

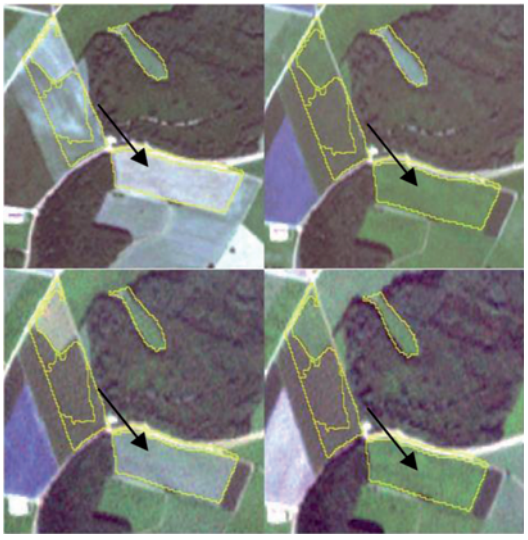

Abb. 4: Analyse der Schnitthäufigkeit anhand der vier RapidEye Aufnahmezeitpunkte (26.06. gemäht (links oben), 02.08. ungemäht (rechts oben), 22.08. gemäht (links unten), 10.09. ungemäht (rechts unten).

lichen auf eine abrupte Änderung des NDVI im Falle eines Schnittereignisses stützten. Die Klassentrennung deckte auch Fehler in der Ausgangsklasse „Undifferenziertes Grünland“ auf, vor allem vereinzelte Ackerflächen.

Im Anschluss an die Klassifizierung in eCognition wurden die Ergebnisse exportiert und mit ArcGIS 10.1 ServicePack 1 hinsichtlich der Schnittfrequenz untersucht. Dabei wurde folgende Regel angewandt, um Intensivgrünland zu differenzieren: Ein Mahdereignis ist auf allen Mosaiken vom 26.06.–10.09.2011 sichtbar oder nur am 26.06., 02.08. und 22.08. oder 10.09.?

In einem letzten Bereinigungsschritt wurden alle Flächen < 0,05 ha eliminiert und alle Flächen, die eine räumliche Überlagerung mit Straßen des BasisDLM aufweisen, entfernt. Die räumliche Überlagerung wird durch den Fehler der Entzerrung der Rapid-Eye-Szenen verursacht.

2.2.3 Magerrasen basenreicher Standorte

Magerrasen sind extensiv genutzte Grünlandstandorte auf nährstoffarmen („mageren“) Standorten, die durch historische Landnutzungsformen entstanden sind.

Für die Kartierung der Magerrasenstandorte wurden zusätzliche *ground truth* Daten in drei Testgebieten kartiert, da in den bereits verfügbaren *ground truth* Daten zu wenige und räumliche disperse Flächen vorhanden waren, um einen zuverlässigen Algorithmus zu entwickeln.

Ausgangspunkt der Klassifizierung bildeten die in der „Geodatenbasis“ erstellten Klassen: „Artenreiche Wiesen“, Artenreiche Weiden“, „Heide“, „Beweidete Heide“, „Weiden“ und „DLM-GA-Grünland“. Bei diesen Klassen handelt es sich um die Flächen, die Magerrasen enthalten können. Analog zum Vorgehen bei den Feuchtflächen wurde aus der GIS Maske Level 1 die Segmentierung des Rapid-Eye-Mosaiks vom 18.04.2011 generiert. Anhand dieser ließen sich die Magerrasenflächen gut herausfiltern, da diese zum Aufnahmezeitpunkt noch fast keinen Aufwuchs hatten und damit deutliche spektrale Unterschiede zu dem intensiver bewirtschafteten Grünland aufwiesen.

Im Anschluss an diese Vorabgrenzung erfolgte eine Analyse der Schnitthäufigkeit analog zu dem unter 2.2.2 beschriebenen methodischen Vorgehen. Lediglich die Abfrage der Schnitthäufigkeit wurde angepasst; jede Fläche, die mehr als einen Schnitt aufwies, wurde aus den Daten entfernt. Da magere Flächen höchstens einmal jährlich gemäht werden, konnten so Fehlklassifizierungen entfernt werden.

Die so in mehreren Iterationen verbesserte „Geodatenbasis“ wurde als Segmentierungsgrundlage für die Klassifizierung der Orthophotos herangezogen. Die Algorithmenentwicklung erfolgte in mehreren Testgebieten, da das gesamte knapp 1000 km² große Orthophotomosaik für jede Testklassifizierung drei Tage-Rechenzeit in eCognition benötigt.

Für die Klassifizierung wurde eine Segmentierungshierarchie mit zwei Leveln angelegt. Aufbauend auf Level 1 erfolgte eine *multiresolution segmentation* mit den Parametern scale 200, shape 0,3 und compactness 0,5 auf einem zweiten Level unterhalb von Level 1. Die so generierten *geons* trugen der kleinräumigen Strukturierung der Magerrasenpatches Rechnung.

In den Luftbilddaten konnten optisch drei Ausprägungen von Magerrasen unterschieden werden, für die auf Level 2 jeweils eigene Zugehörigkeitsfunktionen/Klassenbeschreibungen entwickelt wurden.

Nach der Übertragung des Algorithmus auf das gesamte Gebiet wurden mittels eines *grow region* Befehls benachbarte Magerrasensegmente zusammengefasst und exportiert. Die Auflösung der Kachelgrenzen wurde mit ArcGIS 10.1 und der darin eingebundenen Extension vLate 2 beta (V-LATE 2013) vorgenommen. Nach Abschluss der Klassifizierung wurden alle als Magerrasen kartierten Flächen innerhalb der Ausgangsklasse „Weiden“ entfernt, da die Textur der Weiden dem Magerrasen zu ähnlich war.

3 Ergebnisse und Diskussion

Die Ergebnisse der Grünlandklassifizierung wurden anhand einer *confusion matrix* ermittelt. Daraus resultierten klassenweise eine *producer's* (*pa*) und *user's accuracy* (*ua*) so-

wie die *overall accuracy* und ein Cohen-Kappa-Koeffizient für die Güte der gesamten Klassifizierung.

Der Cohen-Kappa-Koeffizient der gesamten Grünlandklassifizierung liegt bei 0,69 und die *overall accuracy* bei 80 %.

Das zufriedenstellende Klassifizierungsergebnis kann auf mehrere Faktoren des hier vorgestellten Ansatzes zurückgeführt werden.

Wie beim überwiegenden Anteil von fernerkundungsgestützten Biotopkartierungen seit dem Ende der 1990er hat sich der objektorientierte Bildanalyseansatz mit einer *multiresolution segmentation* und der Adressierung von *geons* auf unterschiedlichen Leveln als geeigneter Ansatz erwiesen, um sehr hochaufgelöste Spektraldaten zu klassifizieren (z. B. Bock 2003, Neubert 2005, Tiede et al. 2008). Insbesondere die Fähigkeit des Segmentierungsalgorithmus, Änderungen eines Biotoptyps präzise abzubilden und das gesuchte *geon* detailgetreu zu erfassen, hat sich dabei als sehr hilfreich erwiesen (vgl. z. B. Dietsche 2007).

Das Einbeziehen von bestehenden Sekundärdaten (zumeist ATKIS Daten) wird ebenfalls von den meisten Autoren verfolgt (z. B. Bock 2003, Leser 2003, Neubert 2005). Mit dem hier verfolgten Ansatz der Kombination unterschiedlicher GIS Daten in der vorgestellten Detaillierung konnte jedoch eine größere Differenzierung von Klassen erreicht werden. So fasst beispielsweise Tiede et al. (2008), der ebenfalls ATKIS Daten für die Vorklassifizierung verwendet und eine ähnliche Gebietsgröße bearbeitet, unterschiedliche Grünlandklassen zu funktionalen Habitatkomplexen zusammen, ohne eine weitere Differenzierung der Grünlandflächen vorzunehmen. Auch lässt sich der Informationsgewinn der detaillierten GIS Daten daran ablesen, dass viele Forschungsansätze standortähnliche, z. B. Feuchtstandorte, oder bewirtschaftungseinheitliche, z. B. Intensivwiesen, Typen untersuchen, ohne dass das gesamte Grünlandspektrum erfasst wird (Dietsche 2007, Franke et al. 2012). Schwer zu trennende Biotoptypen wie z. B. Wirtschaftswiesen und Weiden oder Magerrasen wurden bislang kaum untersucht.

Tab. 1: *Producer's* und *user's accuracy* der Grünlandklassifizierung.

Biotoptyp	Producer's accuracy	User's accuracy
Wirtschaftsgrünland	89 %	77 %
Intensivgrünland	41 %	63 %
Magerrasen	79 %	83 %
Röhricht/Schilf	80 %	94 %
Nasswiesen, Großseggen, Hochstauden, Dominanzbestände	74 %	96 %

Die Klassifizierung von multitemporalen Fernerkundungsdaten wird seit ca. 2011 vermehrt verfolgt, da für viele Gebiete Europas zwischenzeitlich größere Zeitreihen der RapidEye-Mission verfügbar sind. Wie im hier vorgestellten Ansatz wird beim Grünland häufig die Bewirtschaftung der Flächen dokumentiert (Förster et al. 2011, Franke et al. 2012). Franke et al. (2012) können bei ihrer Klassifizierung von intensiv bewirtschafteten Grünlandflächen bessere Ergebnisse der *producer's accuracy* und der *user's accuracy* als in der vorliegenden Klassifizierung aufweisen. Das liegt daran, dass für das Biosphärengebiet im Jahr 2011 die temporale Verteilung der Szenen nicht ganz optimal war. So fehlt beispielsweise eine Szene zwischen dem 15.05. und dem 31.05., mittels derer der erste Schnitt hätte erfasst werden können. Zwar liegt die *pa* mit 63 % noch in einem akzeptablen Bereich, die *ua* spiegelt allerdings mit 41 % das Fehlen von ein bis zwei Szenen zu einem günstigen Zeitpunkt deutlich wieder. Die Bedeutung der temporalen Verteilung für die Klassifizierung von Grünlandstandorten wird auch von Förster et al. (2011) und Franke et al. (2012) betont.

Die Kombination von Satellitendaten und Orthophotos hat sich vor allem bei der Klassifizierung von Magerrasen als sehr sinnvoll erwiesen. Während mit den RapidEye Daten eine gute Vorabgrenzung anhand eines frühen Aufnahmezeitpunkts im Jahr möglich war, konnten die auf engem Raum stark variierenden Magerrasenpatches mit den hochauflösenden Flugzeugbilddaten einerseits gut abgegrenzt und anschließend verlässlich kartiert werden.

Feuchtflächen wurden bereits in anderen Arbeiten mit zufriedenstellendem Ergebnis, häufig in kleineren Untersuchungsgebieten, klassifiziert (z. B. Dietsche 2007).

Die in der vorliegenden Arbeit vorgenommene relativ grobe Aggregation in zwei Klassen ist dem Umstand geschuldet, dass auf der Schwäbischen Alb Feuchtflächen nur in sehr geringer Zahl vorkommen, so dass die Entwicklung eines stabilen Algorithmus für jeden Biotoptyp kaum möglich war.

Dass ein zufriedenstellendes Ergebnis erzielt werden konnte, ist einerseits der Möglichkeit der Kombination unterschiedlicher Spektraldaten geschuldet. So waren beispielsweise auch bei der Klassifizierung der Feuchtflächen die unterschiedlichen Aufnahmezeitpunkte der RapidEye Daten eine Möglichkeit, Feuchtflächen einer Vorabgrenzung zu unterziehen, die dann mit den Orthophotos verbessert werden konnte. Das Einbeziehen von Lidar-Daten in den Klassifizierungsprozess stellt für die hochwüchsigen Kulturen eine methodische Erweiterung dar. Mittels der Lidar-Daten wurde auch der Versuch unternommen, Großseggenriede zu klassifizieren. Die Algorithmenentwicklung erfolgte im Bodenseeraum, da dort der Biotoptyp verbreiteter ist, und wurde anschließend auf die Schwäbische Alb übertragen. Allerdings konnte dabei für die Schwäbische Alb kein zufriedenstellendes Ergebnis erzielt werden. Vermutlich liegt dies daran, dass die auf der Schwäbischen Alb länger vorherrschende Schneelast die Großseggen länger niederdrückt und sie damit unterhalb der Schwellenwerte des Algorithmus drückt (im Winter vor der Befliegung 50–60 cm max. Schneehöhe).

Die TerraSAR-X Radardaten sollten zur Bestimmung von Feuchtigkeitsgradienten herangezogen werden. Dies erwies sich aber aufgrund der geringen Anzahl von verfügbaren Kacheln und den großen Datenlücken aufgrund des ausgeprägten Reliefes des Gebietes als nicht zielführend. Im Bereich des Albtraufes liegen aufgrund des Neigungswinkels des Satelliten für einen 200 bis 500 m breiten Streifen keine Radardaten vor.

4 Schlussbemerkung

Mit der flächendeckenden Biotoptypen- und Nutzungskartierung im Biosphärengebiet Schwäbische Alb wurden verschiedene spektrale Fernerkundungs- und Lidar-Daten mit amtlichen „Geobasisdaten“ sowie Daten der Umweltbeobachtung in einem innovativen Ansatz auf pragmatische und nachvollziehbare Weise kombiniert. Die Klassifizierungstiefe bewegt sich zwischen der 2. und 4. Stufe des Landes-Biotoptypenschlüssels (LUBW 2009). Insgesamt wurden 50 Biotoptypen klassifiziert.

Für die Klassifizierung von Grünlandbiotoptypen hat sich eine Kombination von weniger hochaufgelösten Satellitendaten und sehr hochaufgelösten Flugzeugdaten mit bereits bestehenden Umweltinformationen als sinnvoll erwiesen. Aus den unterschiedlichen Daten lassen sich Informationen über die Bewirtschaftung, die typischen spektralen Charakteristika oder die dreidimensionalen Charakteristika ableiten und zu fachlich nachvollziehbaren Klassifizierungsregeln zusammenstellen.

Wesentlichen Anteil am Erfolg des Projektes hatte das interdisziplinäre Team von Biologen und Geographen, ohne das die Erstellung wissensbasierter und empirisch ermittelter Klassifizierungsregeln nicht möglich gewesen wäre. Die verwendete Methodik soll für weitere Gebiete, gegebenenfalls Großschutzgebiete, weiterentwickelt werden. Die benutzten Klassifizierungsregeln sind vermutlich genügend valide und robust, um auf andere Gebiete in Deutschland übertragen zu werden, da diese bereits für ein knapp 900 km^2 großes Gebiet erfolgreich eingesetzt wurden.

Literatur

Brand, J., Ehlers, M. & Möller, M., 2002: Abschlussbericht des Projektes „Fortschreibung der Biotop- und Nutzungstypenkartierung mit multispektralen Scannerdaten“. – http://www.schleswig-holstein.de/UmweltLandwirtschaft/DE/NaturschutzForstJagd/_DL/Abschlussbericht_pdf__blob=publicationFile.pdf (16.3.2012).

Bock, M., 2003: Remote sensing and GIS-based techniques for the classification and monitoring of biotopes. – Journal for Nature Conservation **11:** 145–155.

Bock, M., Xofis, P., Mitchley, J., Rossner, G. & Wissen, M., 2005: Object-oriented methods for habitat mapping at multiple scales – Case studies from Northern Germany and Wye Downs, UK. – Journal for Nature Conservation **13:** 75–89.

CBD, 1992: Convention on Biological Diversity. – http://www.cbd.int/convention/text/ (5.3.2013).

Dietsche, D., 2007: Der Einsatz hochauflösender Fernerkundungsdaten zur Klassifizierung und Bewertung von FFH-Gebieten am Beispiel ausgewählter Moorhabitate Schleswig-Holsteins. – Magisterarbeit, Albert-Ludwig-Universität Freiburg, Freiburg.

Förster, M., Schuster, C., Sonnenschein, R., Bahls, A. & Kleinschmit, B., 2011: Möglichkeiten der Erfassung von Landbedeckung und Vegetationsgesellschaften mittels Rapid-Eye-Daten. – Borg, E. & Daedelow, H. (Hrsg.): RapidEye Science Archive (RESA) – Erste Ergebnisse, 3. RESA Workshop, GITHO Verlag, Berlin.

Franke, J., Keuck, V. & Siegert, F., 2012: Assessment of grassland use intensity by remote sensing to support conservation schemes. – Journal for Nature Conservation **20**: 125–134.

Frick, A., 2006: Beiträge höchstauflösender Satellitenfernerkundung zum FFH-Monitoring – Entwicklung eines wissensbasierten Klassifikationsverfahrens und Anwendung in Brandenburg. – Dissertation, Technische Universität Berlin, Berlin.

GA, 2013: Gemeinsamer Antrag. – landwirtschaft-mlr.baden-wuerttemberg.de/servlet/PB/menu/1211144/index.html (5.3.2013).

Kim, H.O., 2007: Beitrag sehr hochauflösender Satellitenfernerkundungsdaten zur Aktualisierung der Biotop- und Nutzungstypenkartierung in Stadtgebieten – Dargestellt am Beispiel von Seoul. – Dissertation, Technische Universität Berlin, Berlin.

Krismann, A., Bischoping, H. & Rentsch, M., 2012 (in press): Landesweite Biomasseberechnung von Gehölzen auf OpenSource-Basis. – Konferenzband: Energetische Biomassenutzung – Neue Technologien und Konzepte für die Bioenergie der Zukunft, 5.12.2012, Berlin.

Lang, S., 2008: Object-based image analysis for remote sensing applications: modeling reality – dealing with complexity. – Blaschke, T., Lang, S. & Hay, G. (Hrsg.): Object-based image analysis: 3–27, Springer, Hamburg.

Leser, C., 2003: Entwicklung operationell einsatzfähiger Methoden zur Biotoptypen-Kartierung anhand hochauflösender HRSC-Daten. – Dissertation Technische Universität Berlin, Berlin.

LUBW Landesanstalt für Umwelt, Messungen und Naturschutz Baden-Württemberg (2009): Arten, Biotope, Landschaft – Schlüssel zum Erfassen, Beschreiben, Bewerten. – 4. Auflage, 314 S., http://www.lubw.baden-wuerttemberg.de/servlet/is/60969/arten_biotope_landschaft.pdf?command=downloadContent&filename=arten_biotope_landschaft.pdf (16.3.2012).

Mander, Ü., Mitchley, J., Xofis, P., Keramitsoglou, I. & Bock, M., 2005: Earth observation methods for habitat mapping and spatial indicators for nature conservation in Europe. – Journal for Nature Conservation **13:** 69–73.

MEKA, 2013: http://www.landwirtschaft-mlr.baden-wuerttemberg.de/servlet/PB/-s/10fw6i44i8yboxb23bsp2hv1f1fimu24/menu/1149417/ (10.3.2013).

NATURA2000, 2002: Arbeitsdokument der Kommission NATURA 2000. – ec.europa.eu/environment/nature/info/pubs/docs/nat2000/2002_faq_de.pdf (5.3.2013).

Neubert, M., 2005: Bewertung, Verarbeitung und segmentbasierte Auswertung sehr hoch auflösender Satellitendaten vor dem Hintergrund landschaftsplanerischer und landschafts-ökologischer Anwendungen. – Dissertation, Technische Universität Dresden, Dresden.

Schlüter, W., 2011: Zusammenarbeit des Landesbetriebs ForstBW mit dem LGL (Vortrag 24. Mai 2011: https://www.lgl-bw.de/lgl-internet/web/sites/default/de/01_Aktuelles/Veranstaltungen/Galerien/Dokumente/01_Schlueter.pdf

Tiede, D., Lang, S. & Hölbling, D., 2008: Class modelling of biotope complexes – success and remaining challenges. – http://homepages.ucalgary.ca/~gjhay/geobia/Aug18/GEOBIA%20Proceedings_Linked.pdf (26.6.2012).

V-LATE, 2013: Vector-based Landscape Analysis Tools Extension. – https://sites.google.com/site/largvlate/gis-tools/v-late (5.3.2013).

Adressen der Autoren:

Patric Schlager und Volker Hochschild, Geographisches Institut, Universität Tübingen, Rümelinstr. 19–23, D-72070 Tübingen, e-mail: patric.schlager@geographie.uni-tuebingen.de, volker.hochschild@uni-tuebingen.de

Alfons Krismann, Institut für Landschaftsökologie und Naturschutz (ILN Singen) Singen, Burgstr. 15, D-78244 Singen, e-mail ak@iln-singen.de

Kathrin Wiedmann, Heiko Hiltscher und Klaus Schmieder, Institut für Landschafts- und Pflanzenökologie, Universität Hohenheim, August-von-Hartmann Str. 3, D-70599 Stuttgart, e-mail: kathrinwiedmann@web.de, heiko.hiltscher@googlemail.com, schmied@uni-hohenheim.de

Manuskript eingereicht: November 2012
Angenommen: Februar 2013

PFG 2013 / 3, 0173–0184
Stuttgart, June 2013

Article

Flugzeuggestütztes Laserscanning für ein operationelles Waldstrukturmonitoring

Reik Leiterer, Zürich, Schweiz, Werner Mücke, Wien, Österreich, Felix Morsdorf, Zürich, Markus Hollaus, Wien, Norbert Pfeifer, Wien & Michael E. Schaepman, Zürich

Keywords: forest structure, airborne laser scanning, full-waveform, multi-temporal, understory, deadwood.

Zusammenfassung: Die Struktur des Waldes hat einen signifikanten Einfluss auf die globalen biogeochemischen Stoffkreisläufe und kann darüber hinaus als Indikator dienen, um das Potential zum Erhalt der Biodiversität abzuschätzen und die Widerstandsfähigkeit des Waldes gegen äußere Einflüsse zu bestimmen. Flugzeuggestütztes Laserscanning (ALS) bietet hierbei die Möglichkeit einer räumlich hochaufgelösten Erfassung und Beschreibung sowohl der horizontalen als auch der vertikalen Waldstruktur. Wir stellen robuste Verfahren basierend auf flugzeuggestützten Laserscanningdaten vor, um eine Extraktion von forstwirtschaftlich und -wissenschaftlich relevanten Strukturinformationen zu ermöglichen. Dies beinhaltet: i) die Einzelbaumextraktion, ii) die Bestimmung von Unterwuchs und Bodenbedeckung und iii) die Totholzerkennung. Die Datengrundlage bestand aus multi-temporalen, full-waveform Laserdaten in dichtem Laub- und Mischwald für Testgebiete in der Schweiz (Lägern) und in Deutschland (Uckermark). Basierend auf der ALS-Punktwolke mit ihren geometrischen Attributen und den zugehörigen full-waveform Eigenschaften wurden folgende Methoden angewendet: i) hierarchisches, 3D-Clustering und die Ableitung von *alpha shapes* für die Einzelbaumextraktion, ii) rasterbasierte, vertikale Stratifizierung für die Charakterisierung von Unterwuchs, und iii) die Kombination aus *map algebra* und Vektorisierung für die Totholzanalyse. Die erzielten Genauigkeiten der abgeleiteten Strukturvariablen entsprachen den Anforderungen der traditionellen Forstinventur. Vorbehaltlich der Verfügbarkeit einer entsprechenden Datengrundlage (multi-temporale ALS-Daten mit hohen Punktdichten) ist es mit den vorgestellten robusten Methoden möglich, ein großflächiges und operationelles Waldstrukturmonitoring durchzuführen.

Summary: *Operational forest structure monitoring using airborne laser scanning.* The structure of forests influences the global biochemical cycles and can serve as an indicator to estimate the conservation potential for biodiversity and to determine forest stand resistance to disturbances. Airborne laser scanning (ALS) systems have been proven as suitable tools to provide horizontal as well as explicit vertical information due to the canopy penetration of the emitted signal. We developed robust methods based on multi-temporal ALS data to provide a more efficient monitoring of forest structure variables. The derived forest structure information includes: i) the individual tree delineation, ii) the detection and description of understory and ground cover, and iii) the detection of dead wood. We used full-waveform ALS data under foliated and defoliated conditions in dense, deciduous dominated forest stands in the Lägern (Switzerland) and the Uckermark (Germany). Based on the ALS point cloud with the traditional geometrical characteristics and the related full-waveform information, we applied the following methods: i) hierarchical, 3D-clustering and alpha shape derivation for the individual tree delineation, ii) grid based, vertical stratification for understory detection, and iii) combination of map algebra and vectorization for the dead wood analysis. The validation showed high accuracies for the derived forest structure information following the requirements of traditional forest inventories. We conclude that it is possible to detect and characterize the forest structure with robust methods based on full-waveform ALS data; however, the availability of foliated/ defoliated ALS data with a high point density is indispensable.

 www.schweizerbart.de
DOI: 10.1127/1432-8364/2013/0168 1432-8364/13/0168 $ 3.00

1 Einleitung

Um Ökosystemgüter und -leistungen von Wäldern zu bestimmen und darauf aufbauend eine Quantifizierung zu ermöglichen, bedarf es robuster und operationeller Methoden des Waldmonitorings (Ross 2011, De Groot et al. 2002). Diese ermöglichen sowohl die Entwicklung von flächendeckenden und nachhaltigen Managementstrategien als auch Projektionen über die Entwicklung des Waldes unter sich verändernden klimatischen Bedingungen (Hardiman et al. 2011, Sierra et al. 2009). Speziell die komplexe 3-dimensionale Waldstruktur beeinflusst den Stoffaustausch zwischen Wald und Atmosphäre (Xue et al. 2011, Nadkarni et al. 2008, Yang & Friedl 2003). Darüber hinaus ist die Waldstruktur ein bedeutender Indikator, um den Gesundheitszustand des Waldes zu bestimmen, das Potential zum Erhalt der Waldbiodiversität abzuschätzen oder Aussagen über die Bestandsdynamik zu treffen (Kayes & Tinker 2012, Lindenmayer et al. 2006).

Die Erhebung von Strukturvariablen war bisher mit verschiedenen Einschränkungen verbunden. Die Erhebung im Feld ist zeitintensiv, zum Teil subjektiv und in der räumlichen Ausdehnung eingeschränkt (Foody 2010, Haara & Leskinen 2009, Strand et al. 2002). Traditionelle Fernerkundungsmethoden ermöglichen zwar die Ableitung flächendeckender Informationen, sind aber nur bedingt geeignet, um die vertikale Struktur des Waldes zu beschreiben (Jones et al. 2012, Hall et al. 2011, Wulder et al. 2008, Roberts et al. 2007). In den letzten Jahren sind zunehmend hochaufgelöste, flugzeuggestützte Laserscanningdaten (engl. *Airborne Laser Scanning* – ALS) verfügbar geworden, deren Anwendbarkeit in Hinblick auf die Erfassung sowohl horizontaler als auch vertikaler Waldstrukturvariablen bereits in zahlreichen Studien nachgewiesen wurde (Kaartinen et al. 2012, Wulder et al. 2012, Lindberg & Hollaus 2012, Lindberg et al. 2012, Zhao et al. 2011, Leeuwen & Nieuwenhuis 2010, Wagner et al. 2008). Die in diesen Studien ermittelten Strukturvariablen umfassen sowohl geometrische Variablen, wie zum Beispiel die Baumhöhe, das Kronenvolumen oder den Kronendurchmesser (Kaartinen et al. 2012, Lindberg et al. 2012, Reitberger et al. 2009), als auch biophysikalische Variablen, wie z. B. Blattflächenindex, Kronenschlussgrad (Hilker et al. 2010, Morsdorf et al. 2009) und Holzvorrat (Lindberg & Hollaus 2012). Darüber hinaus finden auch Methoden zur Unterscheidung von Baumarten Anwendung (Heinzel & Koch 2011, Kim et al. 2009). Eine Übertragung dieser Methoden in operationelle Anwendungsbereiche findet zwar vereinzelt statt, ist aber insbesondere für großflächige Anwendungen mit Komplikationen verbunden. Dieses ist unter anderem dadurch bedingt, dass je nach Untersuchungsgebiet die Waldstrukturen voneinander abweichen, z. B. Baumartenzusammensetzung, Bestandesdichte, die entsprechende Datengrundlage nicht zur Verfügung steht oder umfangreiches Vorwissen, z. B. Spezien, Management, und manuelle Datenbearbeitungsschritte notwendig sind (Antonarakis et al. 2011, Korpela et al. 2010, Kim et al. 2009). In dieser Arbeit stellen wir robuste Methoden zur Auswertung von ALS-Daten vor, um die für operationelle Monitoringvorhaben relevanten Strukturvariablen abzuleiten. Diese beinhalten sowohl die Erkennung und Charakterisierung von Einzelbäumen und Unterwuchs als auch die Detektion von Totholz als wichtigen Indikator für z. B. Habitatausweisungen.

2 Testgebiete und Daten

2.1 *Testgebiete*

Für die Anwendung der Methodik zur Totholzerfassung wurde ein 110 ha umfassender Buchenwald im Fauna-Flora-Habitat (FFH) „Hardenbeck-Küstrinchen“ (Deutschland/Uckermark; 53°14‘N, 13°26‘E) ausgewählt. Der Wald weist neben der dominierenden Buche (*Fagus sylvatica*) vereinzelt Fichten (*Picea abies*), Eschen (*Fraxinus excelsior*) und Eichen (*Quercus robur*) auf. Die Waldstruktur variiert zwischen unterwuchsarmen Hallenwäldern und, mit Hinblick auf Alter und Stammdurchmesser der Bäume, sehr heterogene und vertikal stark untergliederten Beständen (Mücke et al. 2012). Die Methodik der Einzelbaumbestimmung und der Unterwuchsdetektion wurde für ein 9 ha großes Testgebiet im Bereich der Lägern (Schweizer Jura;

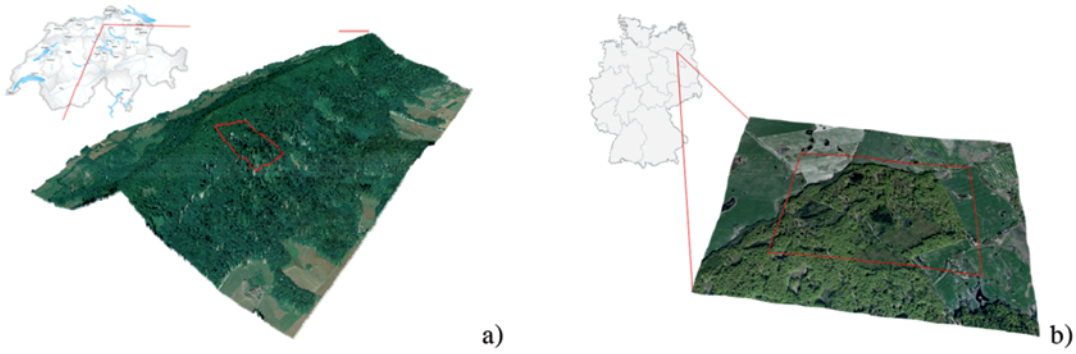

Abb. 1: (a) Untersuchungsgebiet Lägern und (b) FFH-Gebiet „Hardenbeck-Küstrinchen“ mit dem für die Methodenentwicklung ausgewählten Testbereich (rotes Rechteck).

47°28‘N, 8°21‘E) entwickelt und anschließend auf den vollständigen Wald (ca. 16.000 ha) der Lägern angewendet, um die Robustheit der Methodik zu überprüfen. Der Wald setzt sich aus naturnahen Buchenmischbeständen und Fichtenmonokulturen (*Picea abies*) zusammen. In den Mischbeständen finden sich vor allem Buchen (*Fagus sylvatica*), Eschen (*Fraxinus excelsior*), Ahorn (*Acer pseudoplatanus*) und Weißtannen (*Abies alba*) mit einer hohen Variabilität im Hinblick auf Alter (55 – 160 Jahre), Stammdurchmesser (7 cm – 120 cm) und Höhe (bis 45 m) (Eugster et al. 2007). In Abb. 1 sind die Untersuchungsgebiete visualisiert.

2.2 *Referenzdaten*

Im FFH-Gebiet „Hardenbeck-Küstrinchen“ wurden 2011 und 2012 Feldkampagnen durchgeführt, um sowohl liegendes Totholz als auch abgestorbene, aber noch stehende Bäume zu kartieren. Für liegendes Totholz wurden der Start- und Endpunkt des Stammes (für Durchmesser > 30 cm) mittels differentiellem GPS aufgenommen und jeweils Länge, Orientierung und Durchmesser erfasst. Die Lokalisierung des stehenden Totholzes (für Baumhöhen > 3 m und Durchmesser > 30 cm) wurde ebenso mittels differentiellem GPS vorgenommen. Zusätzlich wurden der Durchmesser in Brusthöhe (DBH) und die Baumhöhe gemessen. In Summe wurden 29 Stämme liegendes Totholz und 40 Stämme stehendes Totholz erfasst. Für die Evaluierung und Validierung der abgeleiteten Strukturparameter in der Lägern wurden Feldmessungen zur Inventarisierung des Bestandes und des Unterwuchses durchgeführt, wobei ein mehrstufiges Stichprobenverfahren basierend auf dem VALERI-Ansatz (VALERI 2013) Anwendung fand. Zusätzlich stand ein umfangreicher Referenzdatensatz zur Verfügung: räumlich hochaufgelöste Orthofotos, digitale hemisphärische Fotografien, Daten von terrestrischem Laserscanning (TLS – Z+F IMAGER 5006), Informationen der nationalen Forstinventur und eine pflanzensoziologische Klassifikationen. Diese Daten wurden basierend auf einer klassischen Vermessung mit Tachymeter und differentiellem GPS georeferenziert.

2.3 *Laserscanning Daten*

Um die Methodik zu entwickeln, standen für beide Untersuchungsgebiete full-waveform ALS-Daten mit sehr hohen Punktdichten zur Verfügung. Für die Lägern erfolgten die Aufnahmen im April 2010 unter unbelaubten Bedingungen, hier mit dem RIEGL LMS-Q560 Scanner, und im August 2010, um den Zustand nach der vollständigen Blattentwicklung zu erfassen, hier mit dem RIEGL LMS-Q680i Scanner. Die Aufnahmen im FFH-Gebiet wurden im Mai 2011 unter belaubten und im März 2012 unter unbelaubten Bedingungen durchgeführt. In beiden Befliegungen fand der RIEGL LMS-Q680i Scanner Verwendung. Tab. 1 zeigt die jeweils verwendeten Sensorspezifikationen. Zusätzliche Informationen zu den Sensoren sind in Wagner et al. (2008) sowie in den technischen Sensordo-

Tab. 1: Sensoreigenschaften und verwendete Einstellungen für die jeweiligen ALS-Befliegungen.

	Lägern		FFH-Gebiet Hardenbeck-Küstrinchen	
	LMS-Q560	LMS-Q680i	LMS-Q680i	
Mittlere Flughöhe über Grund	500 m			
Pulsfrequenz	200 000 Hz		400 000 Hz	
Abtastwinkel	± 15°		± 30°	
Mittlere Punktdichte	20 Pkte./m²	40 Pkte./m²	22 Pkte./m²	17 Pkte./m²
Aufnahmedatum/-zeit	10.04.2010	01.08.2010	05.–06.05.2011	22.03.2012

kumentationen von RIEGL zu finden (RIEGL 2012).

Die ALS-Daten wurden dahingehend bearbeitet, dass mittels Gauß-Dekomposition aus den Rohdaten die Ableitung einer Punktwolke mit der exakten räumliche Position (x, y, z-Koordinate) für jedes Echo erfolgte. Über die Analyse der Echo-Wellenform wurden die Echoweite, Amplitude und Intensität bestimmt und als Attribute der Punktwolke hinzugefügt. Ausführlichere Informationen über die Methodik zur Bearbeitung von full-waveform Daten und die daraus abgeleiteten Attribute finden sich in Wagner (2010), Mallet & Bretar (2009) und Persson et al. (2005).

3 Methoden

Aufbauend auf den vorverarbeiteten Daten (vgl. Kapitel 2.3) wurden folgende Vorgehensweisen zur Erfassung der Waldstruktur angewandt: i) die Erkennung und Charakterisierung von Einzelbäumen, ii) die Detektion und Beschreibung des Unterwuchses und iii) die Totholzerfassung.

3.1 *Extraktion von Einzelbäumen*

In einem ersten Schritt wurden aus der ALS-Punktwolke das digitale Geländemodell (DGM), das Oberflächenmodell (DOM) und das Vegetationshöhenmodell (VHM) aus der Differenz von DOM-DGM abgeleitet. Basierend auf dem Ansatz von Evans & Hudak (2007) wurde ein Algorithmus entwickelt, um ein Geländemodell auch in den steilen Hängen der Lägern (bis zu 60° Hangneigung) abzuleiten (vgl. Leiterer et al. 2012). Dieser Algorithmus selektiert Bodenechos und berücksichtigt sowohl die Verteilung der Echotypen und deren geometrische Charakteristiken, als auch die Informationen über die Echoweiten (Mücke et al. 2010). Die so selektierten Echos wurden mit einem Kriging-Verfahren zu einem 1 m x 1 m DGM interpoliert. Die Ableitung des 1 m x 1 m DOMs erfolgte über Echos der Punktwolke mit den jeweils höchsten z-Werten. Im letzten Schritt wurden für jeden Punkt in der Punktwolke als weitere Attribute die zugehörigen DGM-, DOM-, VHM-Werte und die Höhe über Grund zugewiesen. Für die Ableitung von Strukturinformationen auf der Einzelbaumebene ist eine Segmentierung der vollständigen Punktwolke in individuelle Cluster notwendig, die dann die Geometrie von einzelnen Bäumen repräsentieren sollten. Die für die Clusterbildung benötigten Startpunkte wurden über ein *local maximum*-Verfahren basierend auf der Punktwolke ermittelt, wobei ein Strukturelement in Form eines abgeplatteten Rotationsellipsoids Anwendung fand. Ein mit dieser Methode erhaltener Punkt wurde erst dann als lokales Maximum verwendet, wenn er eine Mindesthöhe über Grund von > 3 m aufwies. Die gewählte Mindesthöhe orientiert sich an den gängigen Walddefinitionen nationaler Forstinventuren (vgl. McRoberts et al. 2012) und kann entsprechend der Nutzerbedürfnisse angepasst werden. Lag das lokale Maximum mehr als 3 m unterhalb des entsprechenden VHM-Wertes, wurde von einem Baum im Unterwuchs ausgegangen. Unter Verwendung der Referenzinformationen fand anschließend die Validierung der resultierenden Baumpositionen in Hinblick auf deren Vollständigkeit und räum-

liche Lokalisierung statt. Basierend auf den Baumpositionen erfolgte ein hierarchisches *k-Means*-Clustering, um für jeden Baum eine separate Punktwolke auszuweisen. Da der verwendete Cluster-Algorithmus auf einer euklidische Metrik aufbaut, wurde durch eine Skalierung der Höhenwerte (z-Werte) eine Unterteilung des Merkmalsraums in kugelförmige Objekte angestrebt (vgl. Morsdorf et al. 2004). Für jede Punktwolke berechneten wir anschließend die *alpha shapes* zur Ableitung weiterer kronenspezifischer Variablen, z. B. Kronenvolumen, -oberfläche (Vauhkonen et al. 2009) (Abb. 2).

Innerhalb des Kronenvolumens fand anschließend eine statistische Auswertung der Punktverteilung statt, z. B. Unterschiede belaubt/unbelaubt. Im Zuge der Einzelbaumextraktion wurden folgende Strukturvariablen bestimmt: Baumhöhe, Kronenlänge, Kronendurchmesser, Höhe bis zur Kronenbasis, Kronenvolumen und Kronenoberfläche. Zusätzlich erfolgte die Unterscheidung zwischen Laub- und Nadelbäumen. Die Validierung dieser Variablen erfolgte durch den Vergleich zu den terrestrischen Lasermessungen, den Orthofotos und den Daten aus der Inventarisierung.

3.2 *Detektion und Beschreibung von Unterwuchs*

Für die Detektion und Charakterisierung des Unterwuchses wurde die im Rahmen der Einzelbaumextraktion erstellte ALS-Punktwolke mit den erweiterten Attributen verwendet (vgl. Abschnitt 3.1). Die Detektion des Unterwuchses fand auf Grundlage eines 1 m x 1 m Rasters statt. Für jede Rasterzelle wurde der Bereich zwischen dem kleinsten DGM-Wert und dem höchsten DOM-Wert in Schichten mit einer vertikalen Ausdehnung von jeweils 0,25 m untergliedert. Für jede dieser Schichten wurden anschließend der prozentuale Anteil der Echos im Verhältnis zur Gesamtanzahl der Echos und die Variation der Echos zwischen belaubtem und unbelaubtem Zustand bestimmt. Zusätzlich erfolgte die Auswertung der full-waveform Informationen unter Berechnung der gängigen statistischen Lage- und Streuungsmaße. Um die vertikale Verteilung von Objekten innerhalb eines Echos zu berücksichtigen, wurden Echos mit großen Echoweiten durch Liniensegmente (Länge = Echoweite) mit Ausrichtung in Laserstrahlrichtung ersetzt. Sobald ein Liniensegment innerhalb einer Schicht liegt, wurde dies in der Auswertung wie ein individuelles Echo aufgefasst.

Die Detektion des Unterwuchses beschränkte sich auf die Klassen „Unterwuchs < 0,5 m“ (beinhaltet u.a. Gräser und Moose), „Unterwuchs 0,5–3 m“ und „Bäume im Unterwuchs > 3 m“. Die Bodenbedeckung wurde unterteilt in „vegetationsfreie Flächen“, z. B. Fels, Rohboden oder Kieswege, und „Laub/Nadelstreu“. Einzelne Bäume im Unterwuchs wurden aus der Einzelbaumextraktion übernommen (vgl. Abschnitt 3.1). Die Klassen

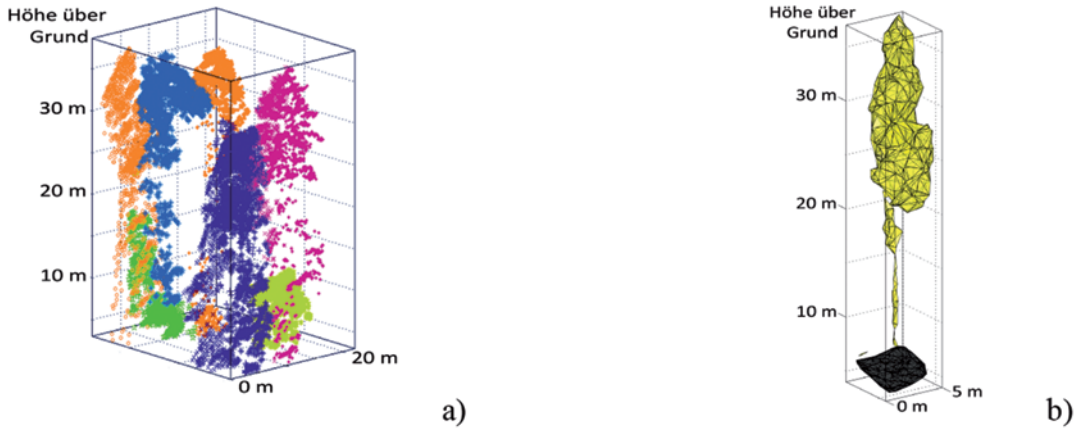

Abb. 2: (a) Segmentierung der Punktwolke in individuelle für die Visualisierung eingefärbte Cluster, (b) Ableitung der *alpha shapes*.

„Unterwuchs < 0,5 m“ und „Unterwuchs 0,5–3 m“ leiteten sich aus der Echoverteilung innerhalb der Schichten ab. Eine Schicht wurde immer dann einer Vegetationsklasse zugeordnet, wenn mindestens 5 % der Echos im Bereich 0–3 m über Grund innerhalb der jeweiligen Schicht lagen. Um den Klassen „vegetationsfreie Flächen“ und „Laub/Nadelstreu“ zugewiesen zu werden, mussten sowohl 95 % der Echos im Bereich 0–3 m innerhalb der ersten Schicht (0–0,25 m über Grund) liegen und mindestens 95 % dieser Echos schmale Echoweiten und hohe Amplituden aufweisen. Zusätzlich wurde die Verteilung der Echotypen (z. B. Verhältnis *single echoes* zu *last echoes*) als Indikator für die Lichtverfügbarkeit und die damit verbundene Wahrscheinlichkeit für das Vorhandensein bodennaher Vegetation verwendet (vgl. Mücke & Hollaus 2011). Für die Unterscheidung von „vegetationsfreien Flächen“ und „Laub/Nadelstreu“ fand eine Kombination der Lage- und Streumaße der Echotypen und -weiten sowie der Amplitudenwerte Anwendung. Lagen keine Echos im Bereich 0–3 m über Grund vor, wurde ein Klassifikationswert aus den umliegenden Rasterzellen interpoliert. Die Klassifikation wurde mit den Feldmessungen aus den VALERI-Flächen und der feldbasierten pflanzensoziologischen Klassifikation verglichen.

3.3 *Erfassung von Totholz*

Wie bereits in Kapitel 3.1 methodisch beschrieben, wurde auch für die Totholzerfassung eine um die full-waveform Attribute erweiterte Punktwolke verwendet. Im Unterschied zur Einzelbaumextraktion und zur Unterwuchsdetektion wurde für die Erfassung des Totholzes ein räumlich höher aufgelöstes DGM berechnet (0,25 m x 0,25 m), um die exakte Lokalisierung der Stämme und die Beschreibung der Stammformen zu ermöglichen (vgl. Mücke et al. 2012). In einem ersten Schritt erfolgte die Selektion jener ALS-Punkte, welche den Waldboden inklusive der umgefallenen Stämme repräsentieren. Dieser Selektionsprozess verwendete unter anderem die Echoweite, um Echos von bodennaher Vegetation auszuschließen. Die verbleibenden Echos wurden anschließend mittels der Interpolationsmethode der kleinsten Quadrate für die Erstellung eines detaillierten Oberflächenmodells des Waldbodens und des Totholzes verwendet (DOM_{cand}). Dieses spezielle Oberflächenmodell wurde anschließend mit Methoden der morphologischen Bildverarbeitung und mit Rasterkarten-Algebra aufbereitet, woraus sich eine binäre Karte des liegenden Totholzes ergab. Abschließend fand eine Vektorisierung dieser binären Karte statt. Im Zuge dieser Umwandlung wurden Objekte mit einer Fläche < 3 m² entfernt, da diese mit großer Wahrscheinlichkeit keine liegenden Stämme repräsentieren. Als Vergleichsdatensatz wurde auf Grundlage des DOM_{cand} visuell erkennbares Totholz digitalisiert. Mit dieser Methode wurden 193 liegende Stämme identifiziert. Die Charakterisierung von stehendem Totholz erfolgte über eine explorative Analyse der Punktwolke. Dazu wurden alle Echos in einem Radius von jeweils 2,5 m um das durch die Feldmessungen lokalisierte stehende Totholz ausgewertet. Die Auswertung beinhaltete sowohl die vertikale Verteilung der Echos als auch die entsprechenden full-waveform Attribute.

4 Ergebnisse

4.1 *Einzelbaumextraktion*

Die Einzelbaumextraktion mit den zugehörigen Strukturvariablen resultierte in einer 3-dimensionalen Repräsentation des untersuchten Bestandes (Abb. 3). Die komplexen, auf den *alpha shapes* aufbauenden Kronenformen wurden hierbei auf geometrische Primitive reduziert, Ellipsoide für Laubbäume und Paraboloide für Nadelbäume.

Für die 9 ha der Testfläche lagen Referenzinformationen auf Einzelbaumebene vor, wohingegen die Übertragbarkeit und Zuverlässigkeit der Methodik für den vollständigen Wald der Lägern nur auf der Bestandesebene evaluiert werden konnte. Die Bestimmung der Kronen-/Baumpositionen zeigte *commission* (Überlassungsfehler) und *omission errors* (Unterlassungsfehler) von 5,2 % bzw. 13,1 %. Aus dem Vergleich der Ergebnisse der automatischen Unterscheidung in Laubbäume und Nadelbäume mit den Forstinventurdaten er-

gab sich eine Übereinstimmung von 89,7 % bei einem Cohen-Kappa-Koeffizienten von 0,74. Eine Abschätzung der Genauigkeit der abgeleiteten Kronendimensionen ergab für die vertikalen Variablen, z. B. Kronenlänge, Kronenbasis, einen mittleren Fehler von 2,8 m. Die horizontalen Dimensionen sind quantitativ hingegen schwer zu valideren, da insbesondere in dichten Laubwaldbeständen die Kronen stark ineinander übergehen, was keine exakte Bestimmung der äußeren Kronenbegrenzung ermöglichte. Variablen, die auf Bestandsebene abgeleitet wurden, z. B. Baumdichte, Kronenschluss, zeigten sehr hohe Übereinstimmungen mit den durch die Forstinventur erhobenen Größen (mittleres Bestimmtheitsmaß r^2 von 0,78). Nach der Anwendung der Methodik auf den ganzen Waldbereich der Lägern ergaben sich für die auf Bestandesebene abgeleiteten Variablen Baumdichte, Kronenschluss, mittlere Baumhöhe und prozentualer Anteil Laubbäume/Nadelbäume ein mittleres r^2 von 0,73. Damit lagen die Genauigkeiten nur geringfügig unter den Werten, die für die Testfläche erzielt wurden, was die Robustheit der Methodik zumindest für diesen Waldtyp unterstreicht. Signifikante Abweichungen gab es lediglich in sehr jungen Beständen (< 10 m mittlere Baumhöhe), wobei der Einfluss der zeitlichen Differenz zwischen Inventarisierung und Befliegung berücksichtigt werden muss.

4.2 *Detektion und Beschreibung des Unterwuchses*

Die Detektion und Klassifikation des Unterwuchses und der Bodenbedeckung wurde für ein 1 m x 1 m Raster durchgeführt (Abb. 4). Im Bereich der Testfläche (9 ha) erfolgte die Validierung der Bäume im Unterwuchs durch

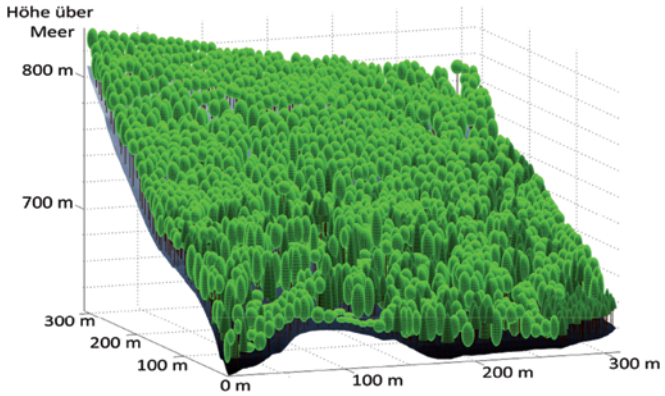

Abb. 3: Visualisierung der Ergebnisse der Einzelbaumrekonstruktion.

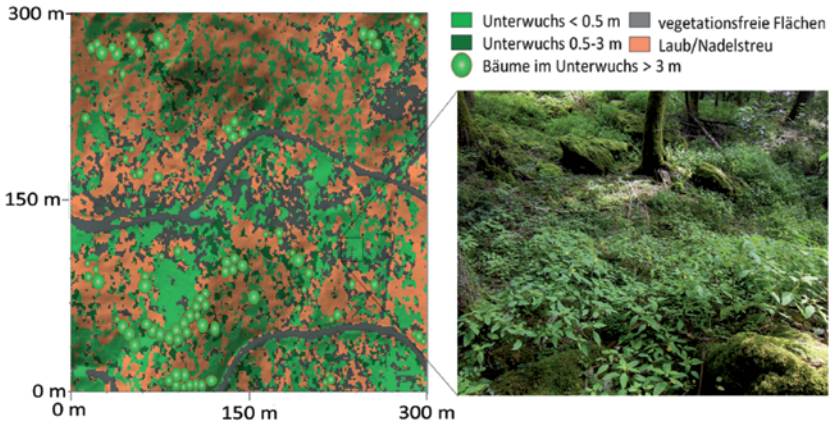

Abb. 4: Ergebnis der Unterwuchs- und Bodenbedeckungsklassifikation. Das Foto zeigt beispielhaft den Unterwuchs für einen ausgewählten Bereich der Klasse „Unterwuchs < 0,5 m“.

Tab. 2: Genauigkeiten der Klassifikation des Unterwuchses und der Bodenbedeckung.

	Unterwuchs 0,5–3 m	Unterwuchs < 0,5 m	Laub/ Nadelstreu	vegetationsfreie Flächen
User's accuracy (%)	73,8	58,3	57,4	63,8
Producer's accuracy (%)	81,7	61,3	51,3	58,7

den Vergleich mit TLS Messungen innerhalb zweier 40 m x 40 m Untersuchungsflächen. Der Unterwuchs und die Bodenbedeckung wurden anhand der pflanzensoziologischen Klassifikation und der stratifizierten Feldmessungen validiert. Eine Validierung der Unterwuchsklassifikation nach der Übertragung der Methode auf den vollständigen Wald der Lägern konnte nicht durchgeführt werden, da flächendeckende Referenzinformationen mit der notwendigen räumlichen Auflösung nicht zur Verfügung standen.

Der aus der Validierung resultierende *commission* bzw. *omission error* für die Erfassung der Bäume im Unterwuchs betrug 26,7 % bzw. 39,8 %. Unter Verwendung der Konfusionsmatrix (vgl. Liu et al. 2007) ergaben sich die in Tab. 2 aufgelisteten klassenspezifischen Genauigkeiten bei einer *overall accuracy* von 64,2 % und einem Cohen-Kappa-Koeffizienten von 0,52.

Wie aus der Konfusionsmatrix ersichtlich wird, war die Detektion von Unterwuchs < 3 m mit einer Zuverlässigkeit von ca. 89 % möglich. Die größte Klassenüberschneidung findet zwischen Laub/Nadelstreu und den vegetationsfreien Flächen statt, da insbesondere die Struktureigenschaften des Bodens sehr ähnlich den entsprechenden Eigenschaften von Laub/Nadelstreu sind.

4.3 *Totholzerfassung*

Anhand der im Feld durchgeführten Kartierung und der manuell digitalisierten Stämme erfolgte die Genauigkeitsabschätzung für die Totholzerfassung. Mit der vorgestellten automatischen Methode ist es gelungen, 70,5 % der umgestürzten Bäume zu detektieren. Bei 37 % der detektierten Bäume war eine vollständige Erfassung und bei 33,2 % eine teilweise Erfassung der Stammdimensionen möglich. Abb. 5 zeigt beispielhaft die Ergebnisse der DOM_{cand}-Erstellung und der darauf basierenden binären Karte sowie die resultierende Totholzklassifikation (vgl. Mücke et al. 2012).

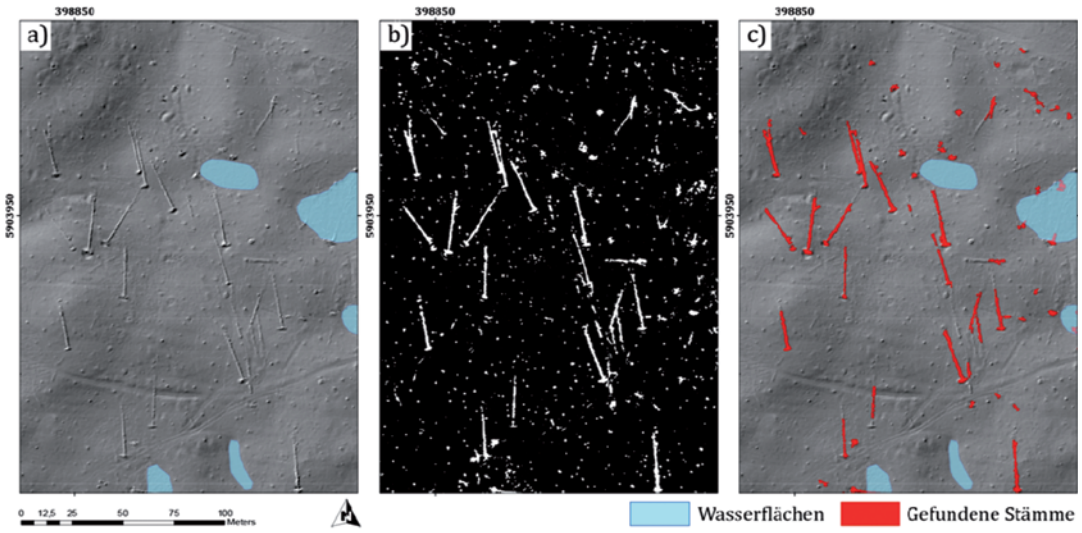

Abb. 5: (a) DOM_{cand}, (b) binäre Karte des liegenden Totholzes, (c) Vektorkarte der Stammdetektion.

Die explorative Analyse der Punktwolke zur Erfassung von stehendem Totholz ergab, dass die Verteilung der Echos und die jeweiligen Amplitudeninformation die wichtigsten Indikatoren für die Ausweisung von stehendem Totholz sind. Vertikal gleichmäßig verteilte Echos repräsentieren mit einer hohen Wahrscheinlichkeit tote Bäume. Dabei konnte keine signifikante Bedeutung der unterschiedlichen Echotypen festgestellt werden. Auch die Unterschiede der vertikalen Echoverteilung zwischen den Aufnahmen im belaubten und unbelaubten Zustand konnte nicht für eine Differenzierung herangezogen werden. Im Gegensatz dazu wurden deutliche Unterschiede in der vertikalen Verteilung der Amplitudenwerte zwischen den beiden Aufnahmen festgestellt. Für das Totholz ist die Verteilung relativ homogen, während für die noch lebenden Bäume eine deutliche Zunahme der Amplitudenwerte in den oberen Kronenschichten, bedingt durch die Laubbildung erkennbar ist.

5 Diskussion

Die Ergebnisse zeigen, dass mit den entwickelten Methoden im Vergleich zu traditionellen Ansätzen eine verbesserte Beschreibung räumlich expliziter Waldstrukturinformationen bei einem deutlich geringeren Zeitaufwand erreicht werden kann. Dabei lag der Schwerpunkt der Methodenentwicklung insbesondere auf einer automatisierten und robusten Anwendbarkeit, um eine einfache Übertragung des Verfahrens auf großflächigere Anwendungsgebiete zu gewährleisten. Bis auf eine Initialisierung der Algorithmen mit den nutzerspezifischen Eingangsvariablen „Mindesthöhe eines Baumes“, „Signifikanzniveau“ und der jeweiligen Pixelgröße für rasterbasierte Auswertungen (DGM, DOM, $DOM_{cand,}$ VHM, Unterwuchsklassifikation) sowie der Definition der Klassengrenzen für die Unterwuchsklassifikation (Höhen-Schwellwerte) bedarf es keiner zusätzlichen, manuellen Interaktionen. Einige Einschränkungen und Unsicherheiten sind dennoch gegeben: Da das lokale Maximum innerhalb einer Krone nicht zwingend senkrecht über der zugehörigen Stammposition liegen muss, kann dies insbesondere in steilen Hangbereichen zu einer Überschätzung der Baumhöhen führen. Die hohen *omission error* bei der Einzelbaumextraktion sind primär durch nicht erfasste Bäume im Unterwuchs verursacht. In diesem Zusammenhang ist insbesondere die Bewirtschaftung des Waldes von Bedeutung, da diese die kleinräumliche Gruppierung von Bäumen beeinflusst, z. B. durch Stockausschlag (vgl. VAN CALSTER et al. 2008). Die hohen *commission errors* bei der Bestimmung von Bäumen im Unterwuchs sind hingegen durch vertikal stark untergliederte Kronen der dominanten Bäume verursacht. Die Fehlerwerte entsprechen hierbei den Resultaten vorhergehender Studien, z. B. KAARTINEN et al. (2012) und FERRAZ et al. (2012), und verdeutlichen die generelle Limitierung bei der Bestimmung von Bäumen im Unterwuchs, selbst wenn ALS-Daten im unbelaubten Zustand mit sehr hohen Punktdichten zur Verfügung stehen. Für die Unterwuchsklasse „Unterwuchs < 0,5 m“ ist die Qualität des abgeleiteten DGMs ausschlaggebend, da eine sehr kleinräumliche Heterogenität in der Topographie zu deutlichen Fehlklassifikationen führen kann. Auch für die Detektion des Totholzes ist die Qualität des DGMs und damit verbunden des DOM_{cand}s ausschlaggebend. Dies ist insbesondere deshalb problematisch, da durch den Filteralgorithmus der DGM-Erstellung die bodennahen Punkte des Totholzes und der Vegetation entfernt werden sollen, die Erhaltung räumlich kleiner Geländeunebenheiten aber notwendig ist, um diese im weiteren Verlauf nicht als Totholz zu klassifizieren. Zusammenfassend ist festzuhalten, dass für die vorgestellte räumlich hoch aufgelöste Erfassung von Waldstrukturinformationen full-waveform ALS-Daten mit sehr hohen Punktdichten unabdingbar sind. Um eine zuverlässige Unterwuchscharakterisierung und Totholzerkennung durchzuführen, sind zudem Aufnahmen im unbelaubten Zustand notwendig. Inwieweit in diesem Zusammenhang die Anforderungen an die Datengrundlage, z. B. minimale Punktedichte pro m^2, die Notwendigkeit von full-waveform Daten und der Einfluss des Abtastwinkels genauer spezifiziert werden können, ist Inhalt weiterführender Untersuchungen.

Danksagung

Wir danken dem STSE Programm der Europäischen Weltraumorganisation (ESA) für die Finanzierung des 3D-VegetationLab Projektes. Teile dieser Studie wurden aus Mitteln des ChangeHabitats2 Projektes (Marie Curie FP7-PEOPLE-2009-IAPP – Grant Agreement No. 251234) finanziert.

Literatur

Antonarakis, A.S., Saatchi, S.S., Chazdon, R.L. & Moorcroft, P.R., 2011: Using LiDAR and Radar measurements to constrain predictions of forest ecosystem structure and function. – Ecological Applications **21** (4): 1120–1137.

De Groot, R.S., Wilson, M.A. & Boumans, R.M.J., 2002: A typology for the classification, description and valuation of ecosystem functions, goods and services. – Ecological Economics **41** (3): 393–408.

Eugster, W., Zeyer, K., Zeeman, M., Michna, P., Zingg, A., Buchmann, N. & Emmenegger, L., 2007: Nitrous oxide net exchange in a beech dominated mixed forest in Switzerland measured with a quantum cascade laser spectrometer. – Biogeosciences Discussion **4** (2): 1167–1200.

Evans, J.S. & Hudak, A.T., 2007: A multiscale curvature algorithm for classifying discrete return LiDAR in forested environments. – IEEE Transactions on Geoscience and Remote Sensing **45** (4): 1029–1038.

Ferraz, A., Bretar, F., Jacquemoud, S., Gonçalves, G., Pereira, L., Tomé, M. & Soares, P., 2012: 3-D mapping of a multi-layered Mediterranean forest using ALS data. – Remote Sensing of Environment **121:** 210–223.

Foody, G.M., 2010: Assessing the accuracy of land cover change with imperfect ground reference data. – Remote Sensing of Environment **114** (10): 2271–2285.

Haara, A. & Leskinen, P., 2009: The assessment of the uncertainty of updated stand-level inventory data. – Silva Fennica **43** (1): 87–112.

Hall, F.G., Bergen, K., Blair, J.B., Dubayah, R., Houghton, R., Hurtt, G., Kellndorfer, J., Lefsky, M., Ranson, J., Saatchi, S., Shugart, H.H. & Wickland, D., 2011: Characterizing 3D vegetation structure from space: Mission requirements. – Remote Sensing of Environment **115** (11): 2753–2775.

Hardiman, B.S., Bohrer, G., Gough, C.M., Vogel, C.S. & Curtis, P.S., 2011: The role of canopy structural complexity in wood net primary production of a maturing northern deciduous forest. – Ecology **92** (9): 1818–1827.

Heinzel, J. & Koch, B., 2011: Exploring full-waveform LiDAR parameters for tree species classification. – International Journal of Applied Earth Observation and Geoinformation **13** (1): 152–160.

Hilker, T., van Leeuwen, M., Coops, N.C., Wulder, M.A., Newnham, G.J., Jupp, D.L.B. & Culvenor, D.S., 2010: Comparing canopy metrics derived from terrestrial and airborne laser scanning in a douglas-fir dominated forest stand. – Trees – Structure and Function **24** (5): 819–832.

Jones, T.G., Coops, N.C. & Sharma, T., 2012: Assessing the utility of LiDAR to differentiate among vegetation structural classes. – Remote Sensing Letters **3** (3): 231–238.

Kaartinen, H., Hyyppä, J., Yu, X., Vastaranta, M., Hyyppä, H., Kukko, A., Holopainen, M., Heipke, C., Hirschmugl, M., Morsdorf, F., Næsset, E., Pitkänen, J., Popescu, S., Solberg, S., Wolf, B.M. & Wu, J.C., 2012: An international comparison of individual tree detection and extraction using airborne laser scanning. – Remote Sensing **4** (4): 950–974.

Kayes, L.J. & Tinker, D.B., 2012: Forest structure and regeneration following a mountain pine beetle epidemic in southeastern Wyoming. – Forest Ecology and Management **263:** 57–66.

Kim, S., McGaughey, R.J., Andersen, H.-E. & Schreuder, G., 2009: Tree species differentiation using intensity data derived from leaf-on and leaf-off airborne laser scanner data. – Remote Sensing of Environment **113** (8): 1575–1586.

Korpela, I., Ørka, H.O., Maltamo, M., Tokola, T. & Hyyppä, J., 2010: Tree species classification using airborne LiDAR – effects of stand and tree parameters, downsizing of training set, intensity normalization, and sensor type. – Silva Fennica **44** (2): 319–339.

Leeuwen, M. & Nieuwenhuis, M., 2010: Retrieval of forest structural parameters using LiDAR remote sensing. – European Journal of Forest Research **129** (4): 749–770.

Leiterer, R., Morsdorf, F., Schaepman, M.E., Mücke, W., Hollaus, M. & Pfeifer, N., 2012: Robust characterization of forest canopy structure types using full-waveform airborne laser scanning. – Conference Proceedings SilviLaser, Vancouver, Canada.

Lindberg, E. & Hollaus, M., 2012: Comparison of methods for estimation of stem volume, stem number and basal area from airborne laser scan-

ning data in a hemi-boreal forest. – Remote Sensing **4** (4): 1004–1023.

Lindberg, E., Olofsson, K., Holmgren, J. & Olsson, H., 2012: Estimation of 3D vegetation structure from waveform and discrete return airborne laser scanning data. – Remote Sensing of Environment **118** (4): 151–161.

Lindenmayer, D.B., Franklin, J.F. & Fischer, J., 2006: General management principles and a checklist of strategies to guide forest biodiversity conservation. – Biological Conservation **131** (3): 433–445.

Liu, C., Frazier, P. & Kumar, L., 2007: Comparative assessment of the measures of thematic classification accuracy. – Remote Sensing of Environment **107:** 606–616.

Mallet, C. & Bretar, F., 2009: Full-waveform topographic LiDAR: State-of-the-art. – ISPRS Journal of Photogrammetry and Remote Sensing **64** (1): 1–16.

McRoberts, R.E., Tomppo, E., Schadauer, K., Vidal, C. & Ståhl, G., 2012: Harmonizing national forest inventories. – Forest Science **58** (3): 189–190.

Morsdorf, F., Meier, E., Kötz, B., Itten, K., Dobbertin, M. & Allgöwer, B., 2004: LIDAR-based geometric reconstruction of boreal type forest stands at single tree level for forest and wildland fire management. – Remote Sensing of Environment **92** (3): 353–362.

Morsdorf, F., Nichol, C., Malthus, T. & Woodhouse, I.H., 2009: Assessing forest structural and physiological information content of multispectral LiDAR waveforms by radiative transfer modeling. – Remote Sensing of Environment **113** (10): 2152–2163.

Mücke, W., Briese, C. & Hollaus, M., 2010: Terrain echo probability assignment based on full-waveform airborne laser scanning observables. – International Archives of Photogrammetry and Remote Sensing **XXXVIII/7A:** 157–162.

Mücke, W. & Hollaus, M., 2011: Modelling light conditions in forests using airborne laser scanning data. – SilviLaser, Hobart, Australia.

Mücke, W., Hollaus, M. & Pfeifer, N., 2012: Identification of dead trees using small footprint full-waveform airborne laser scanning data. – SilviLaser, Vancouver, Canada.

Nadkarni, N.M., McIntosh, A.C.S. & Cushing, J.B., 2008: A framework to categorize forest structure concepts. – Forest Ecology and Management **256** (5): 872–882.

Persson, Å., Söderman, U., Töpel, J. & Ahlberg, S., 2005: Visualization and analysis of full-waveform airborne laser scanner data. – International Archives of Photogrammetry, Remote Sensing and Spatial Information Sciences **36** (3): W19.

Reitberger, J., Schnörr, C., Krzystek, P. & Stilla, U., 2009: 3D segmentation of single trees exploiting full-waveform LiDAR data. – ISPRS Journal of Photogrammetry and Remote Sensing **64** (6): 561–574.

RIEGL, 2012: Products. Airborne Scanning. Datasheets. <http://www.riegl.com/nc/products/airborne-scanning/produktdetail/product/scanner/> (21.12.2012).

Roberts, J., Tesfamichael, S., Gebreslasie, M., van Aardt, J. & Ahmed, F., 2007: Forest structural assessment using remote sensing technologies: an overview of the current state of the art. – Southern Hemisphere Forestry Journal **69** (3): 183–203.

Ross, A.N., 2011: Boundary-layer flow within and above a forest canopy of variable density. – Quarterly Journal of the Royal Meteorological Society.

Sierra, C.A., Loescher, H.W., Harmon, M.E., Richardson, A.D., Hollinger, D.Y. & Perakis, S.S., 2009: Interannual variation of carbon fluxes from three contrasting evergreen forests: the role of forest dynamics and climate. – Ecology **90** (10): 2711–2723.

Strand, G., Dramstad, W. & Engan, G., 2002: The effect of field experience on the accuracy of identifying land cover types in aerial photographs. – International Journal of Applied Earth **4** (2): 137–146.

VALERI, 2013: w3.avignon.inra.fr/valeri/ (20.2.2013).

Van Calster, H., Baeten, L., Verheyen, K., De Keersmaeker, L., Dekeyser, S., Rogister, J.E. & Hermy, M., 2008: Diverging effects of overstorey conversion scenarios on the understorey vegetation in a former coppice-with-standards forest. – Forest Ecology and Management **256** (4): 519–528.

Vauhkonen, J., Tokola, T., Packalén, P. & Maltamo, M., 2009: Identification of Scandinavian commercial species of individual trees from airborne laser scanning data using alpha shape metrics. – Forest Science **55** (1): 37–47.

Wagner, W., Hollaus, M., Briese, C. & Ducic, V., 2008: 3D vegetation mapping using small-footprint full-waveform airborne laser scanners. – International Journal of Remote Sensing **29** (5): 1433–1452.

Wagner, W., 2010: Radiometric calibration of small-footprint airborne laser scanner measurements: Basic physical concepts. – ISPRS Journal of Photogrammetry and Remote Sensing **65** (10): 505–513.

Wulder, M.A., Bater, C.W., Coops, N.C., Hilker, T. & White, J.C., 2008: The role of LiDAR in sustainable forest management. – The Forestry Chronicle **84** (6): 807–826.

Wulder, M.A., White, J.C., Nelson, R.F., Næsset, E., Ørka, H.O., Coops, N.C., Hilker, T., Bater, C.W. & Gobakken, T., 2012: LiDAR sampling for large-area forest characterization: A review. – Remote Sensing of Environment **121:** 196–209.

Xue, B.-L., Kumagai, T., Iida, S., Nakai, T., Matsumoto, K., Komatsu, H., Otsuki, K. & Ohta, T., 2011: Influences of canopy structure and physiological traits on flux partitioning between understory and overstory in an eastern Siberian boreal larch forest. – Ecological Modeling **222** (8): 1479–1490.

Yang, R. & Friedl, M.A., 2003: Modeling the effects of three-dimensional vegetation structure on surface radiation and energy balance in boreal forests. – Journal of Geophysical Research D: Atmospheres **108** (16): GCP10-1–GCP10-11.

Zhao, K., Popescu, S., Meng, X., Pang, Y. & Agca, M., 2011: Characterizing forest canopy structure with LiDAR composite metrics and machine learning. – Remote Sensing of Environment **115** (8): 1978–1996.

Adressen der Autoren:

Reik Leiterer, Felix Morsdorf & Michael E. Schaepman, UZH Universität Zürich, Institut für Geographie, Labor für Fernerkundung, Winterthurerstrasse 190, CH-8057 Zürich, Tel.: +41-44-6356517, Fax: +41-44-6356846, e-mail: {reik.leiterer}{felix.morsdorf}{michael.schaepman}@geo.uzh.ch

Werner Mücke, Markus Hollaus & Norbert Pfeifer, Technische Universität Wien, Institut für Photogrammetrie und Fernerkundung, Gusshausstraße 27–29, A-1040 Wien, Austria, e-mail: {wm}{mh}{np}@ipf.tuwien.ac.at

Manuskript eingereicht: November 2012
Angenommen: Februar 2013

PFG 2013 / 3, 0185 – 0195
Stuttgart, June 2013

Article

Automated Analysis of Satellite Imagery to provide Information Products for Humanitarian Relief Operations in Refugee Camps – from Scientific Development towards Operational Services

Dirk Tiede, Petra Füreder, Stefan Lang, Daniel Hölbling & Peter Zeil, Salzburg, Austria

Keywords: object-based image analysis, refugee and IDP camps, GMES, knowledge-based rule-sets, information products, conditioned information

Summary: Assistance to displaced people in crisis situations requires coordinated and timely action. The latest generation of very high resolution satellite imagery, previously limited in terms of availability and/or resolution, has opened new possibilities for aid organisations to enhance their own reconnaissance. This paper documents the development of algorithms for automated satellite imagery based analysis of refugee and IDP (internally displaced people) camps, and their application over several years under varying conditions, i.e. different sensors and different areas. At fourteen sites VHR (very high resolution) satellite data of four different sensors were used to analyse camps by applying automated dwelling extraction including dwelling differentiation, dwelling density calculation and camp outline estimations, as well as camp monitoring over time. Ranging from experimental stage research, over real-time and benchmarking exercises to pre-operational information provision, the OBIA (object-based image analysis) processing routines greatly matured in terms of transferability, usability and operability.

Zusammenfassung: *Automatische Auswertung von Satellitenbilddaten zur Bereitstellung von Informationen zur Unterstützung von humanitären Hilfsaktionen in Flüchtlingslagern – von wissenschaftlicher Entwicklung bis hin zu funktionsfähigen Diensten.* Die Versorgung von Flüchtlingen in Krisensituationen erfordert koordinierte und zeitkritische Hilfsmaßnahmen. Die Fernerkundung als Quelle zeitnaher, flächendeckender und unverfälschter Primärdaten eignet sich insbesondere seit dem Zeitalter der höchstauflösenden optischen Daten zum Monitoring und zur Folgenabschätzung von Bevölkerungsbewegungen in Krisensituationen, insbesondere von Flüchtlings- bzw. Vertriebenenlagern in schwer erreichbaren oder nicht zugänglichen Gebieten. In diesem Beitrag werden die Entwicklung von Algorithmen zur automatisierten Analyse von Satellitenbilddaten im Bereich von Flüchtlingslagern und deren praktische Anwendungen über einen mehrjährigen Zeitraum und unter verschiedenen Bedingungen beschrieben. Die Anwendungen umfassen bisher insgesamt 14 unterschiedliche Gebiete unter Nutzung von vier unterschiedlichen Sensoren zur Extraktion von Behausungsstrukturen inklusive unterschiedlicher Behausungstypen, Analyse der Ausdehnung der Flüchtlings-/Vertriebenenlager, aber auch zum Monitoring über einen längeren Zeitraum hinweg. Angefangen von ersten experimentellen Entwicklungen über Echtzeit- bzw. Validierungsübungen bis hin zur operationellen Anwendung wird die Verbesserung der auf objektbasierter Bildanalyse (object-based image analysis OBIA) beruhenden Algorithmen hinsichtlich Übertragbarkeit, Verwendbarkeit und Funktionsfähigkeit gezeigt.

www.schweizerbart.de
DOI: 10.1127/1432-8364/2013/0169
1432-8364/13/0169 $ 2.75

1 Introduction

By the end of 2011, 42.5 million people worldwide were forcibly displaced (UNHCR 2012). That means that the number of affected people exceeded 42 million for the fifth consecutive year, a result of persistent and new conflicts in different parts of the world (UNHCR 2012). The highest number since the mid-1990s occurred at the end of 2010, when an estimated 43.3 million people were forcibly displaced due to conflict and persecution (UNHCR 2011). The usefulness of Earth Observation (EO) data to provide important information which may assist in planning and monitoring the activities in refugee and IDP camps, where field assessments are not possible, is widely recognized (Bouchardy 1995, UNHCR 2000, Bjørgo 1999 and 2000). Previously thought to be only at the disposal of military users, the advent of commercial very high resolution (VHR) satellite imagery opened new possibilities for aid organisations to enhance their own reconnaissance. Humanitarian actions that try to relief the life of displaced people often take place in difficult environments. The location of the affected group is often not precisely known. Civil conflicts prohibit the access to those areas: In the case of internally displaced people (IDP), local authorities are not supportive. The location and the number of refugees may change quickly. Under these circumstances aid agencies, especially NGOs (non-governmental organization), require independent information sources to safeguard their personnel and operations. Accuracy and timeliness of information products are essential requirements.

Some few approaches for the automated extraction of dwellings from satellite imagery are documented in the literature. Giada et al. (2003), Lang et al. (2006a), Laneve et al. (2006) and Kemper et al. (2011) showed research applications for automated extraction of dwellings, while Lang et al. (2010) focused on the transfer of such routines for (retrospective) time-series analysis on camp evolution. For the operational and more sustainable usage of such automated algorithms, continuous improvement is required, especially with respect to:

(1) Transfer of algorithms (different sensors, different areas).
(2) Implementation and performance in real-world and real-time scenarios.
(3) Validation of results, especially reflecting end-users' needs.

This article summarizes previous efforts from initial research to pre-operational service development which have been composed into an efficient processing chain. The applied research was done at the Interfaculty Department of Geoinformatics – Z_GIS (University of Salzburg) and embedded in a series of EU FP (framework programme) 6/7 research projects and institutional research support. In 2003, the European Security Policy 'A secure Europe in a better world' (European Council 2003) broadened security from an exclusive concern regarding the security of the state towards a concern regarding also the security of the citizens. Instead of traditional warfare, e.g. tanks, barracks in national security, objects such as the status of the infrastructure, migration routes, as well as population monitoring became the objects for observation under 'human security'. The challenge of defining and developing methodologies and tools to serve the observational needs emerging from the new definition of security was taken up by the Network of Excellence GMOSS (Global Monitoring for Security and Stability, 2004–2008) in the early stages of the Global Monitoring for Environment and Security GMES (Jasani et al. 2009). During this research effort and the subsequent pre-operational service development projects LIMES (Land and Sea Integrated Monitoring for European Security, 2006–2010) and G-MOSAIC (GMES services for Management of Operations, Situation Awareness and Intelligence for regional Crises, 2009–2012), methodologies and workflows for refugee and IDP camp monitoring using EO data were developed and tested.

Building on this experience, Z_GIS recently entered into an operational commitment with humanitarian aid organizations, whereby the provided services reached a high level of independency from EC funding. This fully supports the GMES idea of establishing self-sustaining services in specific application domains. Recently, GMES was renamed to Co-

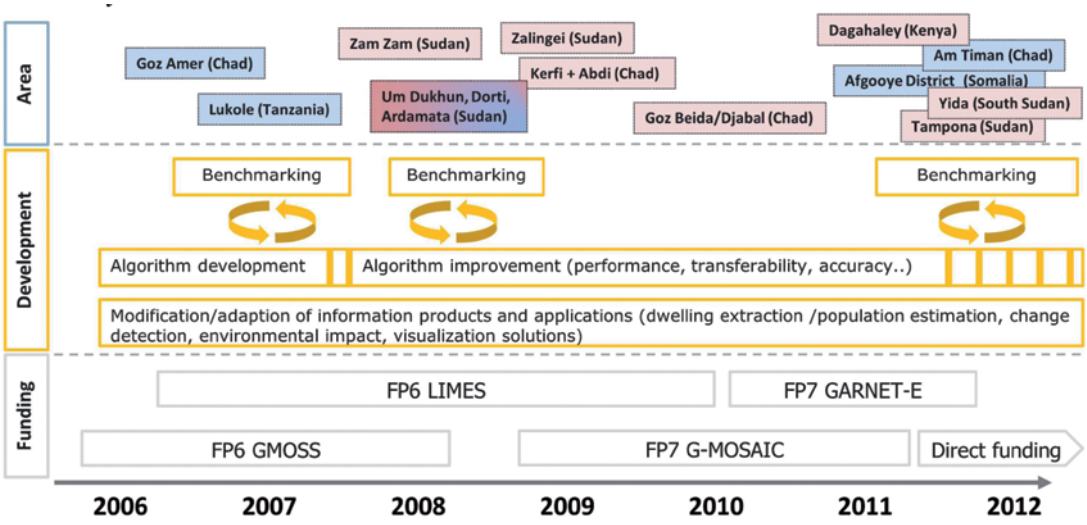

Fig. 1: Overview of the algorithm development since 2006 and the mapped sites (blue: test areas for algorithm development and benchmarking of results, red: pre-operational application areas, red/blue: combined test area (algorithm development and pre-operational application)). The lower part (grey) indicates the research projects/research cooperation supporting the continuous developments, FP = framework programme, LIMES = Land and Sea Integrated Monitoring for European Security, GARNET-E = GMES and Africa: Regional Network for Information Exchange and Training in Emergencies, GMOSS = Global Monitoring for Security and Stability, G-MOSAIC = GMES Services for Management of Operations, Situation Awareness and Intelligence for regional Crises.

pernicus, the European Earth observation programme.

Fig. 1 shows an overview of the research environment for a permanent development and improvement of the algorithms showing also the test areas and benchmarking activities from 2006 until today.

2 Algorithm Development and Improvements

The core algorithm for automated dwelling extraction was developed and improved over several years. Early developments (Lang et al. 2006a and 2006b) were conducted within the FP-6 funded Network of Excellence (GMOSS).

The algorithm relies on object-based image analysis (OBIA) as a methodological framework, which offers the possibility to address complex information classes, defined by spectral, spatial, contextual, as well as hierarchical properties (Lang 2008, Blaschke 2010). Expert knowledge is represented through rule-sets developed within eCognition (Trimble Geospatial Imaging), which offers a modular programming language (CNL, Cognition Network Language) for (image-)object handling (Tiede et al. 2011). Further developments and improvements of the initial algorithms were based on four main pillars:

(1) The development of so called master rule-sets (Tiede et al. 2010): These are generic rule-sets to reduce the time needed for the adaptation of rule-sets if transferred to other camps or other time intervals. To reach this, initial rule-sets are designed where all fixed thresholds, e.g. spectral thresholds, class definitions, are defined as initial variables. This is similar to classical software development and allows the encapsulation of the rule-sets in combination with a graphical user interface (GUI) for parameter adaptation.

(2) Adapted segmentation techniques (Lang et al. 2010, Tiede et al. 2010): Since standard segmentation techniques were not sufficient to achieve a satisfactory delineation of dwelling structures (especially in complex areas), an adapted approach incorporating edge filtering

algorithms as additional parameters for class descriptions of anthropogenic elements (De Kok & Wezyk 2008) was developed. An initial classification of objects at a coarser scale level based on the underlying edge detection layer leads to a better identification of refugee camp areas while minimizing false positives outside of the camp areas at the same time. In addition, class modelling techniques are applied such as cyclic object combination, building on an initial segmentation, and stepwise classification based on parameterized regionalization techniques. These class modelling techniques lead to improved delineations of single dwelling structures.

(3) Improvement of the transferability by reducing absolute thresholds: The classification of dwelling structures builds to a certain degree on relative differences regarding spectral information and spatial characteristics (Tiede et al. 2010). Spatial characteristics such as size, shape and arrangement of the dwelling structures are combined with relative spectral differences between the objects. For example, the identification of a bright dwelling structure is defined relative to darker neighbours, or dark fence structures can be distinguished through shape descriptors from dark round huts. Therefore, fixed spectral thresholds could be significantly reduced in the classification process. Some thresholds like an NDVI threshold and separation values between the main dwelling structures still need to be set. Using sensors such as WorldView-2 with eight spectral bands, the adaptation of rule-sets requires additional expert override, but has the advantage of an improved feature extraction due to the extended spectral information.

(4) Performance improvements: High (timely) performance is one main asset of automated approaches compared to manual image interpretation. In this respect the algorithm was successfully tested in distributed computing environments (Tiede & Lang 2008). New 64 bit based software versions are also leading to performance gains. An entire VHR satellite scene can now be analysed without using distributed computing in acceptable timeframes, i.e. < 4 hours computing time after the adaptation of the rule-sets for an IKONOS scene on a standard PC.

Degree of automation and required accuracies

Ideally, the geometric and thematic accuracy of an automated camp analysis should be comparable to the results of a visual interpretation. In such an ideal situation the automated approach is faster and leads to more detailed results in some areas, as for example the extraction of dwellings as polygons with a measurable size accounts for more accurate population estimations. The degree of automation depends mainly on specific conditions such as complex versus simpler camp structures and the quality of the image data. Complex situations are e. g. caused by cloud shadows within the camp areas, camp locations in very densely vegetated areas or a large variety of building material used for shelters. In contrast, simpler situations for example exist in camps composed of predominantly uniform tent types or huts with corrugated iron roofs. These factors directly influence the adaptation efforts of the master rule-sets. Most of the applications (Tab. 1) make use of satellite imagery such as QuickBird or IKONOS with four spectral bands. The resolution of IKONOS (1 m panchromatic, 4 m multispectral) is the lower limit for single dwelling detection; higher spatial resolutions are preferred (0.5 m in the panchromatic band is at the moment the

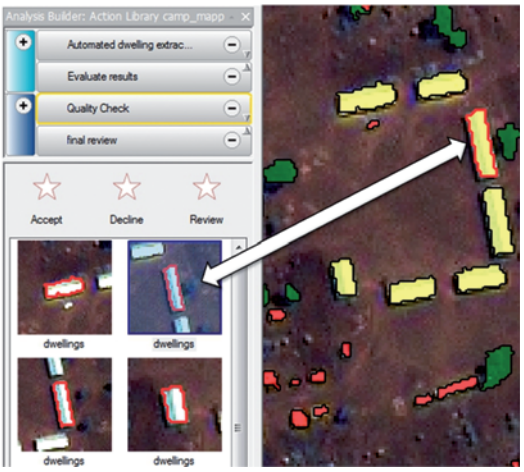

Fig. 2: Hybrid solution for a combined automated and manual analysis and quality check, programmed in eCognition Architect. Extracted dwellings are visualized as thumbnails for an easier post-processing and editable as well as linked to the object in the image scene.

limit, at least for non-US Government customers). Through the availability of new sensors like WorldView-2 with eight spectral bands, improved feature extraction is possible, but the additional bands have to be addressed in the expert rule-set. This increases usually the time for the master rule-set adaptation.

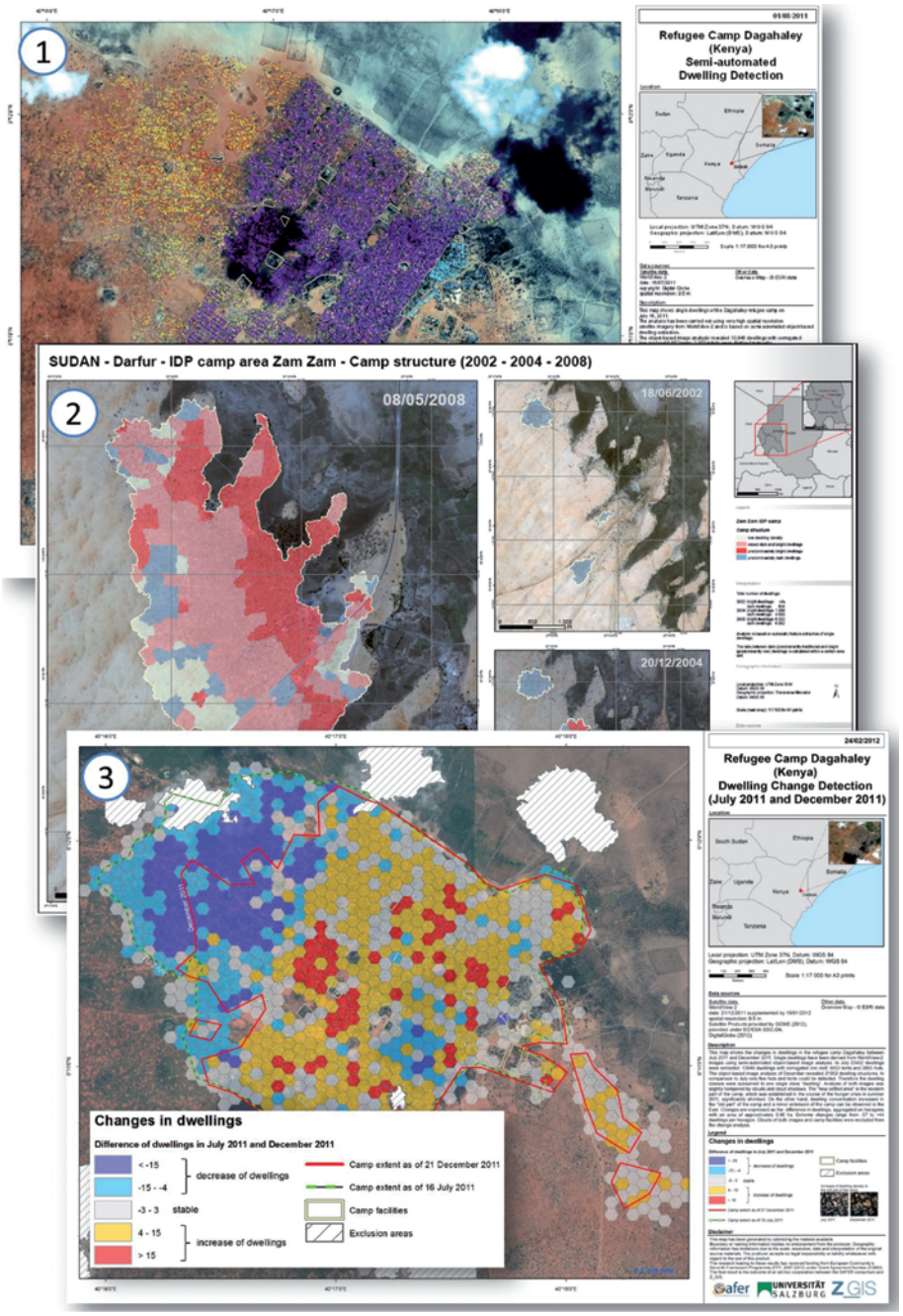

Fig. 3: Examples for products derived from the automated dwelling extraction: (1) single dwelling extraction with different dwelling types (Dagahaley refugee camp, Kenya); (2) camp structure analysis based on dwelling type distributions (IDP camp evolution based on three time slices in Zam Zam, Sudan); (3) change detection analysis and camp outline estimation based on single extracted dwellings aggregated to hexagonal units (Dagahaley refugee camp, Kenya, two time slices) (Füreder et al. 2012).

Under very complex conditions, so called hybrid solutions are applied. They combine automated object detection and manual interpretation in a synergetic manner. Fig. 2 shows such a user interface which supports editing, in order to achieve acceptable accuracies in less favourable environments. The graphical user interfaces and the routines for quality check and analysis are programmed in eCognition Architect.

3 Accuracy Assessment, Benchmarking Exercises and User Validation

Accuracy assessment is very important for the evaluation of the reliability of information products, but in the case of refugee and IDP camps one faces the problem that the products are mostly requested and required in areas where field data is not available or very limited. Only in rare cases real and usable in-situ data are available. Most studies for the development of automated approaches are therefore comparing the results with visual, and in the best case independent, image interpretations (e.g. Giada et al. 2003 and Kemper et al. 2011). For our approach the classification accuracy differs – as mentioned before – due to situation complexity between different camps. More than 90 % classification accuracy could be reached for some camps dominated by dwellings with corrugated iron roofs and/or bright tent types (Lang et al. 2010, Tiede & Lang 2008), whereas around 80 % overall classification accuracy could be reached for mixed structures (Lang et al. 2006a). It dropped partly below 60 % for specific situations like for example dwelling structures which are not easily distinguishable from the surrounding area such as traditional huts and dust or sand covered tents (Lang et al. 2010, Tiede et al. 2010). These figures reflect the results before a potential manual improvement using the described hybrid solutions is applied.

The approach underwent several benchmarking exercises (Fig. 1) in order to calibrate the algorithms and improve the accuracy estimations. This comprised comparisons with automated approaches from other institutions and independent manual interpretation. Results of the benchmarking exercises are documented in the literature (Lang et al. 2006b, Kranz et al. 2010a, Kranz et al. 2010b) and seem promising in terms of accuracy and timeliness, but also reveal the limitations caused by the absence of ground truth, since independent visual interpretations by experts vary a lot.

Building on these experiences a validation study (Grundy et al. 2012) jointly performed with the London School of Hygiene and Tropical Medicine (LSHTM), the Manson Unit – MSF-UK and MSF-OCA (Chad) aimed at the validation of the population estimations derived from two independent manual image interpretations and our automated approach. The results were compared with a population survey carried out by a ground survey of a test area in Am Timan, Chad. For the population survey the quadrat method was used, i.e. sample squares (quadrats) from an overlaying grid of constant size were randomly selected and the ground survey was performed within each of the sampled squares. The resulting estimation of the population density for the samples is then multiplied by the total surface area to compute a population estimate for the whole area. Despite of a general compliance between the methods – with differences mainly in dwelling structure type rather than in total count – it proved the automated method to have its advantages for large areas with less complex structures and recursive analysis (monitoring) over time. The information delivery process can be subdivided in two domains: (1) the user domain addressing relevance and impact, and (2) the information provider domain comprising the translation of the user's request into a service or product regarding demand, thematic information, spatial resolution, and others. The validation of the process and its outputs can then be split in user validation, i.e. feedback by users on relevance and impact of the information product, and technical validation, i.e. effectiveness, efficiency. The latter is a subject well attended by the scientific community (Zeil & Lang 2009).

4 Information Products and Information Delivery

Fig. 3 shows a summary of information products originating from an automated analysis. The base information is the amount of single dwellings distinguished between different dwelling types, e.g. tents, round huts, and camp facility structures. Based on this, the population can be estimated if average occupancy rates per dwelling type are available. Additional information products based on the single dwellings comprise camp structure, e.g. calculated by considering the ratio between tents and huts as an indicator for newly settled areas, and dwelling density measured as dwellings per km² using kernel density methods (Silverman 1986, Lang et al. 2010, Tiede et al. 2010) to provide a better overview on the spatial distribution of the dwellings. Based on the dwelling density, a camp outline can be approximated which is helpful in rapidly expanding camps where the extent can hardly be observed on the ground. The change of camps can be monitored if satellite images of different times are available. Changes of dwellings are visualized using regular shapes, like hexagonal units, or grids, or non-regular features like camp management areas, as reporting units for a fast and easy to grasp overview of the areas undergoing major changes.

All information is delivered to the user as maps in geospatial PDF format, i.e. georeferenced and multi-layer enabled, but also, if requested, as web-services based on Google's KML format or as ArcGIS online Web-

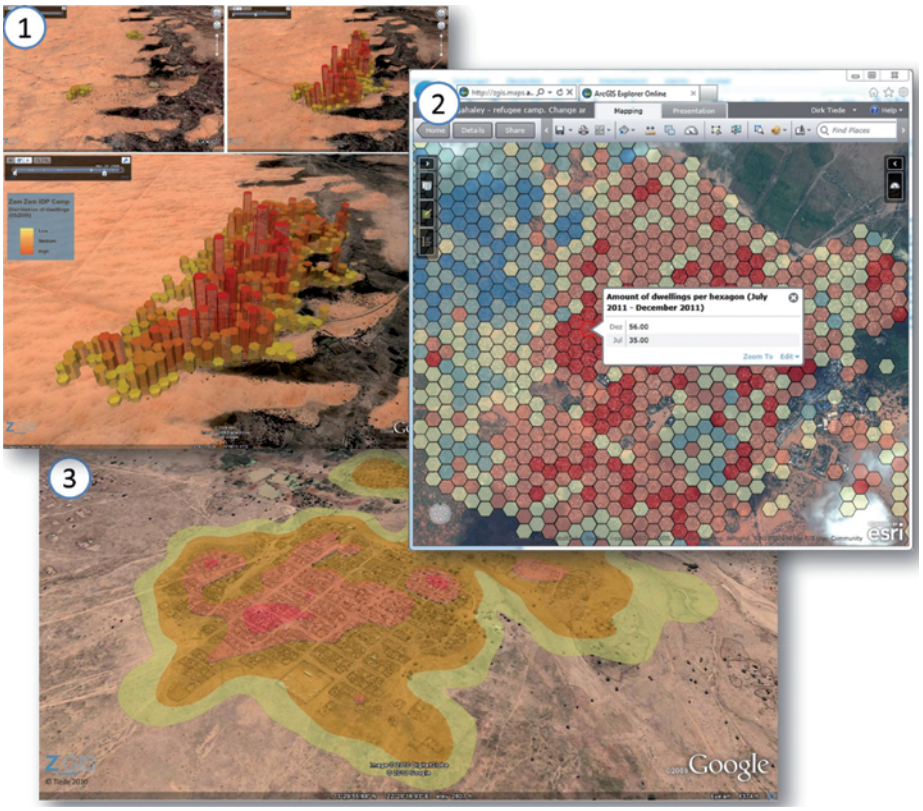

Fig. 4: Web-based visualisations of the information products: (1) Time series of analytical 3D views (Tiede & Lang 2010) in Google Earth showing the development of the IDP camp Zam Zam from 2002 (top left), 2004 (top right) and 2008 (below). Red tones and higher extrusion values of the hexagons indicate higher amounts of automatically extracted dwelling structures (Tiede & Lang 2009); (2) change detection analysis provided via ArcGIS Explorer online, which allows interactive queries; red/yellow tones are indicating increase, blue tones are indicating decrease (Dagahaley refugee camp, Kenya, two time slices); (3) dwelling density analysis, based on kernel density calculations and visualized in Google Earth (IDP camp Dorti, Sudan).

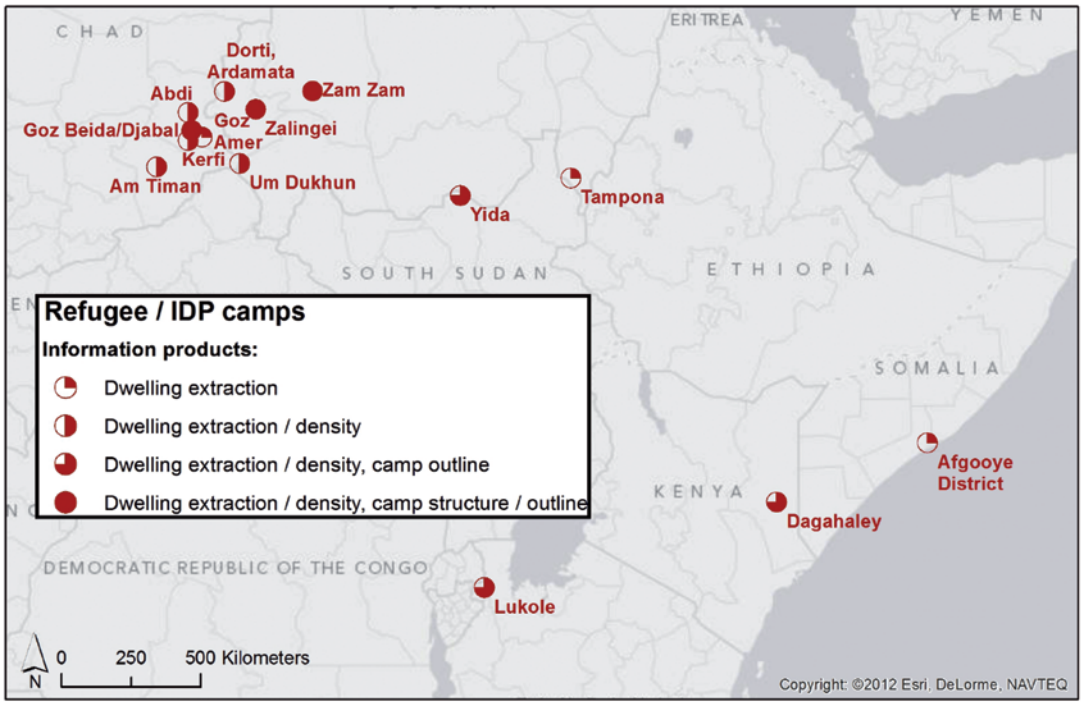

Fig. 5: Overview of the analysed refugee and IDP camps and the provided information products per camp.

Service in conjunction with ArcGIS Server (Fig. 4).

5 Investigated Sites

Fig. 5 shows the location of all refugee and IDP camps which have been analysed since 2006, and the derived products per camp. Tab. 1 indicates the type of analysis (development, benchmarking, real-time exercise/pre-operational application) and the satellite images used. The last column indicates the research project/research cooperation by which the application was co-funded or directly funded. A total of 14 camps were analysed, six of them with more than one time slice, in the case of the IDP camp Zam Zam, even three images were available for retrospective monitoring (Lang et al. 2010). All camps are located in Africa, which limits the experience regarding transferability to certain types of dwelling structures and camp types. Beside emergency shelters, e.g. tents, provided by aid organizations, which are similar in most countries, refugee shelters are often built from local materials and therefore vary from country to country depending on availability, local culture and custom (UNHCR 2007).

6 Discussion and Outlook

The presented applications are the result of a continuous development process, i.e. co-funded research covering more than one funding period, implemented under the GMES/Copernicus framework. Information on the amount and distribution of dwellings can be extracted from VHR imagery in an automated way for inaccessible areas; still, information from the ground is required, e.g. on mean occupancy rates for realistic total population estimations.

We consider the service as still being pre-operational. It requires further research and development as well as frequent applications in order to become fully operational. This is important to improve and test the transferability to other camp structures or types, e.g. on other continents, the overall robustness of the algorithm, and the degree of automation for different sensors. In this respect we need to

decide from case to case what degree of "automation" is possible or sensible: Hybrid approaches may be more appropriate to meet the users' need (Füreder et al. 2012) and, where difficult camp structures and data quality issues prevail, they remain the best choice to provide relevant and reliable information most effectively in many cases.

Close cooperation with users, e.g. humanitarian aid organizations, allows a steady improvement of the provided service and the extension of the product portfolio.

Tab. 1: Refugee and IDP camps analysed since 2006 based on the presented workflow (D = Development, B = Benchmarking, RE = Real Time Exercise).

Refugee / IDP Camp	Data	Application Status	Funding
Goz Amer (Chad)	QuickBird 12/2004	D/B	FP6 GMOSS
Lukole (Tanzania)	IKONOS 09/2000	D/B	FP6 GMOSS
Zam Zam (Sudan)	QuickBird 06/2002 12/2004 05/2008	RE	FP6 LIMES
Zalingei (Sudan)	IKONOS 09/2004 QuickBird 07/2008	RE	FP6 LIMES
Dorti, Ardamata (Sudan)	GeoEye-1 05/2009	RE/B	FP6 LIMES
Um Dukhun (Sudan)	GeoEye-1 05/2009	RE/B	FP6 LIMES
Abdi (Chad)	QuickBird 06/2008 10/2008	RE	FP6 LIMES
Kerfi (Chad)	QuickBird 04/.2006 07/2008	RE	FP6 LIMES
Djabal (Chad)	QuickBird 06/2007 GeoEye-1 03/2010	RE	FP7 G-MOSAIC
Afgooye District (Somalia)	GeoEye-1 01/2011	B	FP 7 GARNET-E
Am Timan (Chad)	WorldView-2 12/2011	B	Institutional Funding
Dagahaley (Kenya)	WorldView-2 07/2011 12/2011 01/2012	RE	Institutional Funding
Tampona (Sudan)	WorldView-2 07/2012	RE	Institutional Funding
Yida (South Sudan)	QuickBird 10/2012	RE	Institutional Funding

Summarizing, constant user feedback including a critical reflection on the overall relevance of the provided information products is essential for sustaining such services, also in terms of funding – especially in low-budget domains like humanitarian aid and civilian conflict resolution. As in many other GMES (Copernicus) domains, high-quality and ubiquitous availability of reliable and well tailored geospatial services, whenever and wherever requested, is crucial for a mutually beneficial and sustaining information market.

Acknowledgements

The presented work was co-funded by the European Commission (EC) within the FP6 and FP7 projects GMOSS (contract no: SNE3-CT-2003-503699), LIMES (contract no: 031046), G-MOSAIC (contract no: 218822) and GARNET-E (contract no: 242385). Direct funding has been received by Médecins Sans Frontières (MSF) Austria and the Karl Kahane Foundation.

References

Bjørgo, E., 1999: Very High Resolution Satellites: A New Source of Information in Humanitarian Relief Operations. – Bulletin of the American Society for Information Science **26** (1): 22–24.

Bjørgo, E., 2000: Using very high spatial resolution satellite sensor imagery to monitor refugee camps. – International Journal of Remote Sensing **21** (3): 611–616.

Blaschke, T., 2010: Object based image analysis for remote sensing. – ISPRS Journal of Photogrammetry and Remote Sensing **65:** 2–16.

Bouchardy, J.-Y., 1995: Development of a GIS system in UNHCR for environmental, emergency, logistic, and planning purposes. – Program report. DPOS UNHCR. Geneva, Switzerland, http://repository.forcedmigration.org/show_metadata.jsp?pid=fmo:3246 (6.1.2013).

De Kok, R. & Wezyk, P., 2008: Principles of full autonomy in image interpretation. – The basic architectural design for a sequential process with image objects. – Blaschke T., Lang, S. & Hay, G. (eds.): Object-Based Image Analysis – Spatial concepts for knowledge-driven remote sensing applications: 697–710, Springer, Berlin, Heidelberg.

European Council, 2003: A secure Europe in a better world – The European Security Strategy (Solana Strategy). – www.consilium.europa.eu/uedocs/cmsUpload/78367.pdf (6.1.2013).

Füreder, P., Hölbling, D., Tiede, D., Zeil, P. & Lang, S., 2012: Monitoring refugee camp evolution and population dynamics in Dagahaley, Kenya, based on VHR satellite data. – **9th** International Conference African Association of Remote Sensing of the Environment (AARSE), El Jadida, Morocco, CD-ROM.

Giada, S., De Groeve, T., Ehrlich, D. & Soille, P., 2003: Information extraction from very high resolution satellite imagery over Lukole refugee camp, Tanzania. – International Journal of Remote Sensing **24** (22): 4251–4266.

Grundy, C., Füreder, P., Siddiqui, R., Katsuva Sibongwe, D., Tiede, D., Lang, S. & Checci, F., 2012: Validation of satellite imagery methods to estimate population size. – MSF Scientific Day, 25 May 2012, London, Great Britain.

Hagenlocher, M., Lang, S. & Tiede, D., 2012: Integrated assessment of the environmental impact of an IDP camp in Sudan based on very high resolution multi-temporal satellite imagery. – Remote Sensing of Environment **126:** 27–38.

Jasani, B., Pesaresi, M., Schneiderbauer, S. & Zeug, G. (eds.), 2009: Remote Sensing from Space: Supporting International Peace and Security. – 298 p., Berlin, Springer Netherland.

Kemper, T.M., Jenerowicz, M., Soille, P. & Pesaresi, M., 2011: Enumeration of dwellings in Darfur Camps from GeoEye-1 satellite images using mathematical morphology. – IEEE Journal of Selected Topics in Applied Earth Observations and Remote Sensing **4** (1): 8–15.

Kranz, O., Lang, S., Tiede, D., Zeug, G., Kemper, T., Caspard, M. & Clandillon, S., 2010a: GMES Services for Conflict Prevention and Mitigation: Support the DG RELEX in Mission Planning. – Konecny, M., Zlatanova, S. & Bandrova, T.L. (eds.): 171–188, Springer, New York.

Kranz, O., Zeug, G., Tiede, D., Clandillon, S., Bruckert, D., Kemper, T., Lang, S. & Caspard, M., 2010b: Monitoring Refugee/IDP camps to Support International Relief Action. – Altan, O., Backhaus, R., Piero Boccardo, P. & Zlatanova, S. (eds.): Joint Board of Geospatial Information Societies (JB GIS), United Nations Office for Outer Space Affairs (UNOOSA).

Laneve, G., Santilli, G. & Lingenfelder, I., 2006: Development of Automatic Techniques for Refugee Camps Monitoring using Very High Spatial Resolution (VHSR) Satellite Imagery. – Geoscience and Remote Sensing Symposium, IGARSS **2006:** 841–845.

Lang, S., Tiede, D. & Hofer, F., 2006a: Modeling ephemeral settlements using VHSR image data and 3D visualisation – the example of Goz Amer refugee camp in Chad. – PFG – Photogrammetrie, Fernerkundung, Geoinformatik, Special Issue: Urban Remote Sensing **2006** (4): 327–337.

Lang, S., Tiede, D. & Santilli, G., 2006b: Varying sensors and algorithms – an information delivery approach for population estimation in African refugee camps. – **6th** African Association of Remote Sensing of the Environment Conference (AARSE).

Lang, S., 2008: Object-based image analysis for remote sensing applications: modeling reality – dealing with complexity. – Blaschke, T., Lang, S. & Hay, G. (eds.): Object-Based Image Analysis – Spatial concepts for knowledge-driven remote sensing applications: 3–27, Springer.

Lang, S., Tiede, D., Hölbling, D., Füreder, P. & Zeil, P., 2010: Earth observation (EO)-based ex post assessment of internally displaced person (IDP) camp evolution and population dynamics in Zam Zam, Darfur. – International Journal of Remote Sensing **31:** 5709–5731.

Silverman, B.W., 1986: Density Estimation for Statistics and Data Analysis. – 175 p., Chapman and Hall, London, New York.

Tiede, D. & Lang, S., 2008: Distributed computing for accelerated dwelling extraction in refugee camps using VHSR satellite imagery. – Car, A., Griesebner, G. & Strobl, J. (eds.), Wichmann, Heidelberg.

Tiede, D. & Lang, S., 2009: IDP camp evolvement analysis in Darfur using VHSR optical satellite image time series and scientific visualization on virtual globes. – Guo, H. & Wang, C. (eds): **Sixth** International Symposium on Digital Earth: Models, Algorithms, and Virtual Reality, SPIE 7840, 78401E, Beijing, China.

Tiede, D. & Lang, S., 2010: Analytical 3D views and virtual globes – scientific results in a familiar spatial context. – ISPRS Journal of Photogrammetry and Remote Sensing **65:** 300–307.

Tiede, D., Lang, S., Hölbling, D. & Füreder, P., 2010: Transferability of OBIA rule-sets for IDP Camp Analysis in Darfur. – Addink, E.A. & Coillie, F.M.B.V. (eds.): ISPRS **XXXVIII-4/C7**, Archives ISSN No 1682–1777.

Tiede, D., Lang, S., Füreder, P., Hölbling, D., Hoffmann, C. & Zeil, P., 2011: Automated damage indication for rapid geospatial reporting. An operational object-based approach to damage density mapping following the 2010 Haiti earthquake. – Photogrammetric Engineering and Remote Sensing **77:** 933–942.

United Nations High Commissioner for Refugees (UNHCR), 2000: Key Principles for Decision-making. Refugee Operations and Environmental Management. Engineering and Environmental Service Section. – UNHCR. Geneva, Switzerland, http://www.unhcr.org/3b03b24d4.html (6.1.2013).

United Nations High Commissioner for Refugees (UNHCR), 2007: Hand-book for emergencies. – Third edition, http://www.unhcr.org/refworld/docid/46a9e29a2.html (22.2.2013).

United Nations High Commissioner for Refugees (UNHCR). 2011: Statistical Yearbook 2010. Trends in Displacement, Protection and Solutions. – Geneva, Switzerland, http://www.unhcr.org/4ef9cc9c9.html (6.1.2013).

United Nations High Commissioner for Refugees (UNHCR). 2012: Global Trends 2011. A year of crisis. – Geneva, Switzerland, http://www.unhcr.org/4fd6f87f9.html (6.1.2013).

Zeil, P. & Lang S., 2009: Do have clients a role in validation? – Corbane, C., Broglia, M., Carrion, D., Lemoine, G. & Pesaresi, M. (eds.): Validation of geo-information products for crisis management VALgEO 2009. – European Commission, Joint Research Centre, Institute for the Protection and Security of the Citizen: 143–147, Ispra, Italy, http://bookshop.europa.eu/en/valgeo-workshop-proceedings-pbLBNA24082/ (20.2.2013).

Address of the Authors:

Dr. Dirk Tiede, Mag. Petra Füreder, Mag. Dr. Stefan Lang, Mag. Daniel Hölbling & Dipl. Geophy. Peter Zeil, Interfaculty Department of Geoinformatics – Z_GIS, University of Salzburg, A-5020 Salzburg, Austria, e-mail: {dirk.tiede}{petra.fuereder}{stefan.lang}{daniel.hoelbling}{peter.zeil}@sbg.ac.at

Manuskript eingereicht: November 2012
Angenommen: Februar 2013

PFG 2013 / 3, 0197 – 0208
Stuttgart, June 2013

Article

Assessment of using ASTER-derived DTM for Glaciological Applications in the Central Andes, Mt. Aconcagua, Argentina

M. Gabriela Lenzano, Mendoza, Argentina

Keywords: ASTER, DTM, glacier volume change, Mt. Aconcagua

Summary: Monitoring glaciers has recently gained more attention, as efforts to better model climate changes are intensifying worldwide. This paper presents a feasibility study on the implementation and performance assessment of digital terrain models (DTMs), derived from Advanced Spaceborne Thermal Emission and Reflection Radiometer (ASTER) optical imagery, in order to determine the altimetric and volumetric changes on Las Vacas and Horcones Superior glaciers, located at 32° 41' S and 69° 57' W in the Mt. Aconcagua area, Mendoza, Argentina. The DTMs were created from ASTER images from 2001 and 2008 in a standard satellite digital photogrammetry environment. To assess the absolute vertical accuracy of the DTMs, GPS data was used, and the results indicated a 24 ± 10 m RMSEz, in topographically complex scenarios and with slopes greater than 30°. To obtain a robust matching as well as to minimize the residuals between DTMs, a 3D conformal transformation was applied to co-register them. To calculate the differences between DTMs, the approach of computing the differences along surface normal vectors was proposed. Next, the changes happened to the glaciers were identified, resulting in −3.15 m/a and −0.92 m/a for Las Vacas and the Horcones Superior, respectively. Finally, the results were tested using the 3D control deformation in order to determine the degree of uncertainty in the estimation of changes in the thickness and volume of glaciers.

Zusammenfassung: *Untersuchung zur Eignung von Höhenmodellen aus ASTER-Daten für glaziologische Untersuchungen in den Zentralanden am Aconcagua, Argentinien.* Das Gletschermonitoring hat an Bedeutung gewonnen, weil weltweit die Bemühungen um eine bessere Modellierung der Klimaveränderung gestiegen sind. Dieser Artikel stellt eine Machbarkeitsstudie zur Nutzung von ASTER-Daten (Advanced Spaceborne Thermal Emission and Reflection Radiometer) zur Bestimmung von Höhen und Volumenveränderungen am Beispiel der Gletscher Las Vacas und Horcones Superior vor (32° 41' S, 69° 57' W, Aconcaguamassiv). Als Datengrundlage dienten zwei ASTER-Szenen von 2001 und 2008. Mit den GPS-bestimmten Bodenpunkten wurde eine Höhengenauigkeit (RMSEz) von 24 ± 10 m in topographisch stark bewegtem Gelände mit bis zu 30° Hangneigung nachgewiesen. Die beiden Höhenmodelle wurden mit einer 3D-Helmerttransformation zusammengeführt, um dann die Unterschiede entlang der Oberflächennormalen zu bestimmen. Daraus ergab sich ein Abtrag von −3.15 m/a beim Las Vacas und −0.92 m/a beim Horcones Superior Gletscher. Abschließend wurde die Genauigkeit der Bestimmung an Kontrollpunkten verifiziert.

1 Introduction

Glaciers play a significant role in controlling downstream water supply in arid or semiarid regions, where precipitation is minimal. Therefore, it is crucial to understand the temporal and spatial behaviour and volume changes of glaciers in those regions. During the late 20th and early 21st centuries, glaciers have suffered a global recession. This sustained de-

www.schweizerbart.de
DOI: 10.1127/1432-8364/2013/0170 1432-8364/13/0170 $ 3.00

cline of ice covered areas is one of the most reliable indicators of global warming (Haeberli 2005, IPCC 2007). A parallel trend is that the demand for fresh water has increased sharply in recent decades. Therefore, research on analysing and quantifying changes in glacier processes has become an important subject, since knowledge of the evolution of glaciers is essential to make future decisions regarding their conservation and/or protection.

Considering that glaciers are usually located in difficult to access areas with complex topography and extreme weather conditions, their monitoring from the ground is a rather complex task. Consequently, remote sensing represents an attractive approach to map glaciers.

To monitor glacier volume changes, digital terrain models (DTMs) represent the ideal data, as from DTMs, acquired at different epochs, both deformation and movements can be detected (Barrand el al. 2009). Nowadays, DTMs are one of the most common products in mapping practice and come in a broad range of spatial resolution and accuracy. Historically, stereo image based surface extraction by photogrammetry used to be the primary source to create digital terrain models (DTMs) until active sensors, such as light detection and ranging (lidar) and synthetic aperture radar interferometry (InSAR) technologies, were introduced. Presently, lidar technology provides a powerful tool for high-density and high-accuracy three-dimensional terrain point data acquisition, and one of the advantages is the direct availability of three-dimensional coordinates of points in object space (Shan & Toth 2008). As an active remote sensing technology, airborne lidar data are practically free of shadows, a major advantage compared to photogrammetric methods where the shadows are a big problem, in particular in areas of complex topography or in glacier areas. Lidar from airborne platforms could provide the most accurate elevation information for glacier surfaces, but its cost is high, and, in fact, prohibitive in many earth science applications. InSAR is a powerful technique to monitor land surface changes from space and air with good quality. The limiting factors in mountainous terrain are occlusions, the difficulty of decorrelation, and the SAR image geometry. Restrictions to the spatial coverage arise from decorrelating snow-covered areas, such as glaciers over forested areas, and shadowing caused by the very rugged topography (Franceschetti & Lanari 1999). Photogrammetry generally falls behind in terms of performance, but is much more affordable from both airborne and satellite platforms. Another important issue is that InSAR and photogrammetry are dependent on ground control, but lidar without GCPs is not more exact than photogrammetry. Despite of the recent dominance of active sensors, optical image-based DTM extraction by photogrammetry has seen significant improvements recently, and provides a less accurate yet very inexpensive alternative to lidar and SAR techniques.

The objective of this study is to investigate the feasibility of using DTMs derived from ASTER imagery to estimate glacier changes in the complex topographic areas of the Mt Aconcagua. The use of satellite image-based digital photogrammetric method represents the first implementation and use of DTMs in that region. While ASTER imagery is very inexpensive, its use presents a challenge due to its coarse resolution and modest georeferencing accuracy. The ASTER product level 1A has the stereo pairs 3N and 3B that permit the generation of topographic mapping products, such as digital elevation models (DEMs), digital terrain models (DTMs) and orthophotos (Iwasaki & Fujisada 2005). Stereo ASTER imagery has been frequently used to monitor glaciers, since it is available at low cost with worldwide coverage (Etzelmüller & Sulebak 2000, Vignon et al. 2003, Rivera 2004, Miller et al. 2009, Bolch et al. 2011).

To get a better understanding of the behaviour and the accuracy of DTMs of different types of relief, it is relevant to make an assessment. DTM errors vary with relief types and elevation. Typical accuracies above 2000 m above sea level (ASL) range between ± 15 to 30 m at the 68 % confidence level, while for the worst case, at 5000 m ASL, the error could reach ± 60 m at the 68 % confidence level (Kääb et al. 2002, Racoviteanu et al. 2007, Schneider et al. 2008). Kääb et al. (2002) showed that the errors increase with the complexity in the topography, and the best eleva-

tion accuracy found for a scenario with moderate topography was ± 18 m. Lang & Welch (1999), Hirano et al. (2002), Toutin (2008), and others found that RMSEz values generally fall between 10 m and 50 m. In the Mt. Everest region, Pieczonka et al. (2011) found data that defies the overall trend, where RMSEz values are 45 m below 5000 m ASL and 37 m above 6000 m ASL. This may be due to the difficulty of validating the elevation data at higher altitudes. Their study also confirmed that for slopes steeper than 50°, the error could be more than ± 105 m.

This investigation is focused on accuracy estimation and assessing the capability to monitor the evolution of glacier surfaces in the Mt. Aconcagua region. A novel component is that the proposed method calculates the elevation difference along surface normal vectors, resulting in better volume difference estimation. The next two sections describe related work and the methodology used for the extraction of the DTMs, including a study on the accuracy of the DTMs using reference fields surveyed by GPS. The computation and analysis of the differences between DTMs, made before and after a robust surface matching, based on a conformal transformation, is discussed in the fourth section. To better identify the changes produced by the glaciers, a test for 3D control deformation is used to assess to what extent the results correspond to noise due to the method, including error budget of the data and algorithmic limitations in resolution, or due to the actual changes by the ice bodies. Finally, the fifth section discusses the results of comparing ASTER DTMs from 2001 and 2008, including the glaciological analysis of the changes found in glaciers during that period.

2 Related Work

DTMs are approximations of the land surface that have inherent inaccuracies that should be taken into account when are used for comparative evaluation in order to ensure the maximum reliability (Nuth & Kääb 2011, Pieczonka et al. 2011).

There are a large number of studies, introducing various methods to analyse and/or minimize the height differences between DTMs in areas with variable topographic complexities to obtain more reliable results to model glaciers. Vignon et al. (2003) conducted tests in the Rio Santa Basin, Peru, with the goal of estimating the local displacement. They selected the calibration area in a region with no spatial changes in time, and thus, obtained unbiased absolute differences in elevation. Berthier et al. (2007) works in the Spiti/Lahaul region in the Himachal Prades, India, and their approach is based on a correction in the glacier elevation changes between DTMs made by subtracting the bias in the ice-free areas. Racoviteanu et al. (2007), working in Nevado Coropuna, Peruvian Andes, computed the vertical differences by subtracting two DTMs on a cell by cell basis. Kääb (2008) studied the glaciers on the Svalbard archipelago, Norway. He selected ice-free areas in the vicinity of and rock outcrops within the ice-caps as reference sites to compare two and more ASTER DTMs. Later, contour models were derived. The average elevation differences were expressed as a function of the elevation, e.g., 4 m by 100 m elevation, and this representation appears to reduce the influence of noise and errors in the mean change in the ice thickness. Miller et al. (2009) were also studying the Svalbard archipelago, Norway, and proposed an algorithm, where the vertical difference between points located on the matched and the reference surfaces is minimized. Nuth & Kääb (2010) focused on regions with characteristics of alpine glaciers. Nuth & Kääb (2011) relate the height differences to the slope and the aspect.

3 Study Area

The study area is located within the Parque Provincial Aconcagua, Mendoza, Argentina, a protected nature reserve, located around 32° 41' S and 69° 57' W (Fig. 1). The characteristics of the relief in the study area are topographically complex with an elevation ranging from 3200 m to 6969 m ASL. The annual precipitation rate for the area at 4000 m ASL is

above 600 mm (Minetti & Corte 1984). The mean annual air temperature at Cristo Redentor (32° 50' S, 70° 05' W) at 3832 m ASL during the period of 1961–1980 was −1.6 °C (Estadísticas Meteorológicas 1986, Trombotto 1991). The Las Vacas glacier is located to the north of Mt. Aconcagua and has an area of 19.4 km² (February 2007). Its orientation is towards the east with an altitudinal range between 3700 m and 5500 m ASL. This is a typical cirque calving glacier with three arms coming together downstream in a big Seracs cascade up to the front. The Horcones Superior glacier is located at the west foot of Mt. Aconcagua where Plaza de Mulas camp is at 4370 m ASL. The orientation is southeast with an area of 5.6 km² in February 2007, and its maximum altitude is 5400 m ASL. Fig. 1 also shows the slope map of the study area with the maximum value of 48° in the south wall of Mt. Aconcagua; also, the elevation histograms of both glaciers are shown.

4 Data and Methods

4.1 *Data Sources*

Images: To support this study, two ASTER scenes were selected. The characteristics of level 1A stereo pairs (3N and 3B) are listed in Tab. 1. The images from the TERRA Advanced Spaceborne Thermal Emission and Reflection Radiometer (ASTER) sensor have a geometric resolution ranging from 15 m to 90 m depending on the bands with an area coverage of 60 x 60 km². The ASTER sensors were designed to produce detailed maps of the temperature, reflectance, elevation and emissivity of the earth surface. The three ASTER telescopes VNIR (visible and near-infrared), SWIR (short wavelength infrared), and TIR (thermal infrared region) can be oriented in the cross track direction, rotating the camera in the ± 24° range. Therefore, ASTER has the ability to generate stereoscopic images through two telescopes, a nadir-looking (3N)

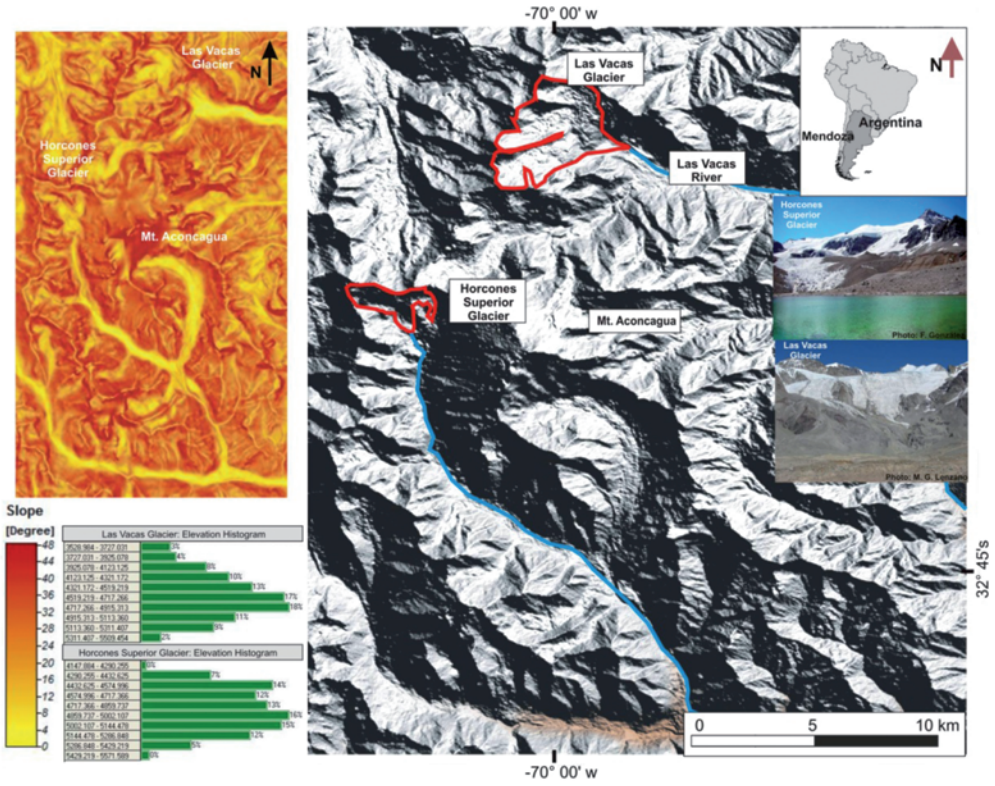

Fig. 1: Map of the study area: upper left: slope map of the study area; lower left: elevation histogram of both glaciers; centre: right shaded relief of the studied terrain; upper right: the location in Argentina; right: Horcones Superior glacier; lower right: Las Vacas glacier.

Tab. 1: Characteristics of images used.

Satellite Sensor	ID	Date	Resolution
TERRA ASTER	AST_L1A_00301132001150259	01/13/2001	15 m
TERRA ASTER	AST_L1A_00301012008145101	01/01/2008	15 m

and a backward-looking (3B) telescope. Both ASTER images were acquired during mid-summer. The images show scarce snow cover and the maximum cloud percentage of 20 % has a limited or no affect over the glacier areas.

GNSS data: GCPs and checkpoints based on GPS surveys were established in the field with respect to a base station located at Horcones lake using the DGPS (differential GPS) static positioning method. This base point is part of the geodetic network of Mendoza province in the framework POSGAR98 (Posicionamiento Geodésico Argentino) (Cimbaro & Lauria 2007, Lauria 2009), and linked to the Permanent Station (PS) network SIRGAS (Sistema de Referencia Geocéntrico para las Américas) (Fortes et al. 2006). The base station at Horcones lake was established by using three PSs, including MZAC in the city of Mendoza, SANT, in Santiago de Chile, and CFAG in the province of San Juan. The receiver installed at the base was a double-frequency receiver, Trimble 5700, and the receivers used as rovers were single-frequency Geo-Tech models. The data processing was based on commercial software, using fixed solutions at the 95 % confidence level. The RMSEs (root-mean-square error) for GCPs were: RMSEx = 0.19 m, RMSEy = 0.22 m, and RMSEz = 0.35 m. This accuracy of the coordinates was satisfactory for this type of investigation.

A reference profile was surveyed along the road from the entrance to the Aconcagua Provincial Park on Lake Horcones through Horcones River to camp Plaza de Mulas (Fig. 5). This profile was used to evaluate the accuracy of the DTMs. The survey was done by kinematic GPS processing (Trimble R3, single-frequency), resulting in errors of RMSEx = 0.37 m, RMSEy = 0.21 m, and RMSEz = 0.36 m.

4.2 *Digital Terrain Model (DTM) Extraction*

Image orientation is solved by the addition of GCPs to optimize the quality (Etzelmüller & Sulebak 2000). The use of GCPs is important to obtain precise georeferencing for the stereo models, as they assure accurate elevation as well as planimetry in the reference frame (Wolf & DeWitt 2000). In this study, 11 GCPs were surveyed by GPS and projected into the Argentine GK2 local mapping frame. To improve the image georeferencing, and subsequently increase the reliability of the DTMs, additional 25 secondary GCPs were derived from the cartographic database of IGN (Instituto Geográfico Nacional, República Argentina) at 1:50,000 scale. Finally, approximately 100 tie points per scene were used to form strong stereo models. The DTMs with a grid size of 45 m were extracted by the digital photogrammetric software Photomod 4.4 (Rózycky & Wolniewicz 2007, Liba & Jarve 2009).

During the relative orientation, the y-parallax value for the 2001 and 2008 stereo models was 1.1 and 1.2 pixels RMSE, respectively. After performing the absolute orientation, the residuals at GCPs for both models are shown in Tab. 2. According to Toutin (2008), these results range between the acceptable limits of accuracy, given the geometric resolution of the ASTER imagery.

From the two datasets acquired in 2001 and 2008, the first one, DTM_{01}, was considered as the base or reference in the subsequent analysis, i.e. the DTM_{08} was compared to DTM_{01} with the objective to minimize the residual errors produced by the photogrammetric transformation (Vignon et al. 2003).

The surface of the glaciers is represented by TIN structures (triangulated irregular network). In addition to automatically created surface points, topographic discontinuities,

Tab. 2: Residuals of GCPs in the 2001 and 2008 stereo pairs, respectively (RMSE = root-mean-square error, STD = standard deviation).

		Res X (m)	Res Y (m)	Res Z (m)
2001	RMSE	19.0	20.1	21.8
	Mean	15.3	14.8	18.6
	STD	11.3	13.6	11.4
	Max	39.7	46.8	40.6
2008	RMSE	13.1	12.6	23.8
	Mean	10.5	9.6	20.7
	STD	7.3	8.2	11.7
	Max	34.6	29.1	37.8

through manually measured breaklines and points were modelled, improving the relief forms in areas with complex landscape (Marzolff & Poesen 2009).

4.3 *DTM Differencing*

The difference between DTMs was assessed based on using a variety of topographic features, such as rocky outcrops that are assumed to be static in the proximity of the glaciers under study. Based on comparing 100 points, the RMSEz found for ΔH_{01-08} was 26 m, see Tab. 3. The Fig. 2 shows the places where the relative differences between the DTMs were taken.

Results shown in Tab. 3 may indicate that the mathematical model needed to adequately describe the surface differences could be quite complex, as the definition of the shift between two glacier surfaces is not a simple task. Regardless of the model complexity, the approach is based on minimizing the differences between the two surfaces in a least squares sense. Assuming that the surface shape changes slower than the movement of the glacier, a 3D conformal transformation was selected to model the surface changes. If this assumption does not hold for a complete area, then the area can be segmented to smaller sub-areas that should be independently processed. In this study, a robust matching was achieved by using a large number of outcrops as references as well as other surface features of the glaciers (Berthier et al. 2007, Kääb 2008). The 7 parameters of the 3D conformal transformation are three rotations (ω, φ, κ), three translations (X, Y, Z) and a scale factor (s). Tab. 4 shows the adjusted values for both glaciers. The results from the calculation of the parameters reflect the relative accuracy of ASTER models; the rotations angles are considerably larger in ω, φ due to the shape of the scenes, while the shifts in X, Y, and Z are generally in the order of a half pixel. Note that the transformation produced an improvement in the accuracy of both models. Fig. 3 shows a profile of DTM_{01} overlaid on DTM_{08} before and after applying the 3D conformal transformation. Errors decreased between 14 % and 77 %. The location of this profile (A) is shown in Fig. 5.

Tab. 3: Differences between DTM_{01} and DTM_{08} respectively.

Glacier	Mean ΔXY_{01-08} (m)	Mean ΔZ_{01-08} (m)
Las Vacas	27.3 ±15.5	15.3 ±13.0
Horcones Superior	15.7 ± 9.3	34.7 ±13.2

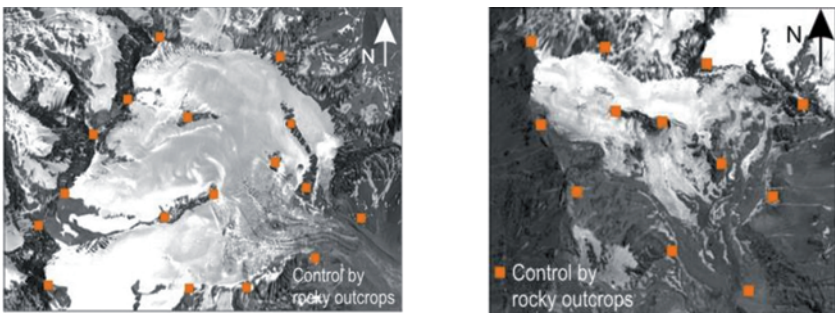

Fig. 2: Location of rocky outcrops around the glaciers: a) LV (Las Vacas), b) HS (Horcones Superior).

Tab. 4: Transformation parameters for both glaciers.

Glacier	ω(°)	φ(°)	κ(°)	X (m)	Y (m)	Z (m)	scale	Number of iterations
Las Vacas	0.416	0.130	0.008	7.78	−5.71	2.69	0.999	4
Horcones Superior	0.455	−0.221	0.124	−7.08	11.69	5.66	1.000	4

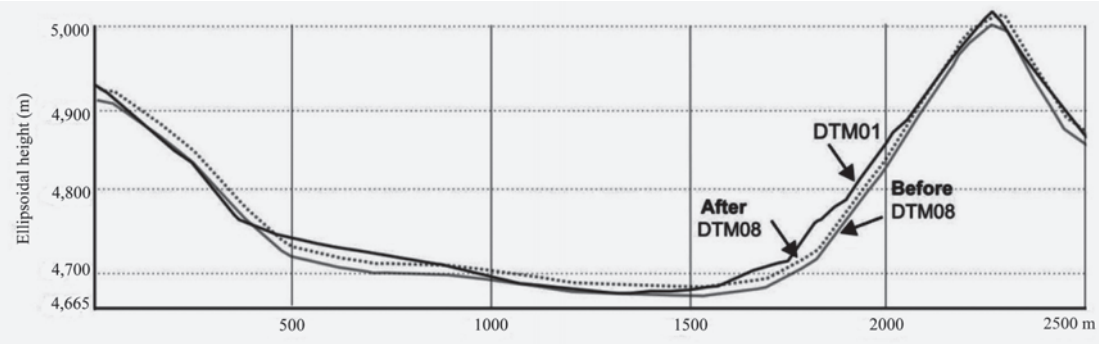

Fig. 3: Profiles before and after applying the transformation.

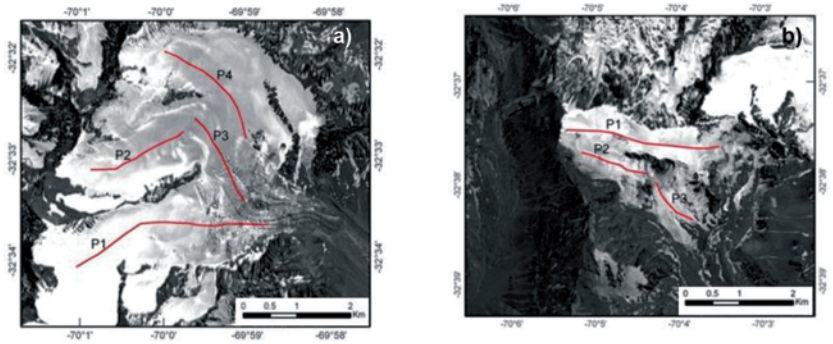

Fig. 4: Profiles overlaid on the glaciers (ASTER image 2001): a) LV (Las Vacas), b) HS (Horcones Superior).

4.4 *Glacier Surface Changes (2001–2008)*

The areal changes, ΔA_{01-08}, in the period of 2001–2008 were derived from ASTER orthorectified images by manually delineating glaciers. This process was repeated several times to determine the deviation of the manual method. The surfaces were expressed per convention as surfaces projected to the ground reference plane.

Profiles on the glaciers were generated by manual delineation, following the line of the ice central flow on 3D surfaces, and the elevation differences (ΔH_{01-08}) were computed along them. Fig. 4 shows the location of the profiles over the glaciers. The elevation differences were taken as normal differences between both surfaces. By comparing DTM_{01} and DTM_{08}, the volumetric changes (ΔV_{01-08}) of the glaciers were determined. The volumetric changes were estimated using an iterative method that re-triangulates a new surface based on points from both surfaces, and then calculates the new surface elevations based on the difference between the elevations of the two surfaces.

4.5 *Testing Changes in the Glaciers*

Since deformations introduced during the generation of DTMs substantially impact the final quality of any derived products, it is important to quantify the distortion and noise introduced in the models, and determine the degree of uncertainty in the estimation of changes in ice volume (Koblet et al. 2010). In this study, the method of *testing 3D displacement vectors by confidence ellipsoids* (Sutti & Torok 1996) was implemented which basically mean applying tests to the profile changes of the glaciers. The significance of a statistical hypothesis test allows for deciding whether a point movement can be considered as a physical deformation, a displacement, or random measurement errors (noise). In this work, only the elevation change (ΔH_{01-08}) along the profiles was analysed using single variable-based deformation assessment.

In this study, the noise coefficient T_k (1) was calculated based on the test with respect to the d_k vector as threshold. Note that d_k is defined by the distance between points of the corresponding 2001 and 2008 data. The vector d_k was taken at 50 m spacing along of the profiles of both glaciers. In the study all measurements were taken with the same weight. The vector d_k provides information about the movement between two periods. Values that are above the T_k thresholds imply that there have been actual changes of the glaciers. If the d_k value is less than T_k, it means noise or no deformation.

$$|T_k| = \sigma_0 \sqrt{Q_{hk} F_{1-a}} \tag{1}$$

Where

σ_0: average standard error of the profile in each epoch $\frac{\sigma_1^2 + \sigma_2^2}{2}$

σ_1, σ_2: average standard error of the profile in each epoch

Q_{hk}: is a function of the measurements weights

F_{1-a}: coefficient which is extracted from the Fisher-Snedecor table (Forbes et al. 2011).

Fig. 5: GPS checkpoints (green) and profile B (red) used for the validation of the DTMs, and profile A (black) used for evaluating the robust surface matching (ASTER image 2001).

5 Results

5.1 *DTM Accuracy Assessment*

The investigated area represents an extreme scenario, as the elevation range is between 3800 m and almost 7000 m ASL and the average height is 5000 m ASL. To assess the absolute accuracy of the DTMs, the elevation data, H, extracted from the 3D models, were compared with seven fairly evenly distributed GPS checkpoints, independent of the GCPs (Fig. 5). The vertical accuracy between ASTER and GPS data was 24 ± 10 m RMSEz, and 28 ± 12 m in planimetry. Furthermore, a GPS transect from the entrance to the Parque Provincial Aconcagua through the Horcones River valley until the Plaza de Mulas camp was acquired. Using that GPS profile, the RMSEz for $\Delta(H_{GPS}–H_{DTM})$ was 44 ± 9 m for DTM_{01}, and 52 ± 11 m for DTM_{08}. Fig. 5 shows the distribution of GPS check points in green colour and the profile in red colour.

5.2 *Area, Volume and Mass Changes*

The 2D areal variations of the glaciers during the 2001–2008 period were as follows: the Las Vacas and Horcones Superior glaciers diminished by 9 % and 12.4 %, respectively (Tab. 5).

The elevation changes ΔH through the comparison of the different profiles extracted from the DTMs during the 2001–2008 period were computed. Tab. 5 shows the elevation mean values for every profile in each glacier, free of noise, and the computed T_k threshold values. T_k coefficients in both glaciers show a variation between 28.2 m and 29.5 m, and therefore, values above these are considered as changes of the glacier surface by the co-registration. Based on that, all profiles had deformations except for the LV-2 on the Las Vacas glacier.

Tab. 5: Mean elevation variations in glaciers and T_k values.

Glacier	Noise coefficient T_k (m)	Profile	Mean ΔH_{01-08} /a
Las Vacas	29.5	#1	0.87 ± 1.4
		#2	estimation failed
		#3	−7.1 ± 1.1
		#4	−1.5 ± 1.4
Horcones Superior	28.2	#1	0.63 ± 0.8
		#2	0.16 ± 0.06
		#3	−3.56 ± 1.9

The profiles were analysed by this test for a change of the elevation and, as a result, on average 31 % of the cases were due to the loss of glacial ice. In the case of Las Vacas, based on the LV-1, LV-3 and LV-4 profiles examined, the glacier lost mass with an average decline of −4.3 m/a. Only the LV-1 profile shows a modest gain of mass. Since this profile is oriented from west to east, many of its points are in the accumulation zone. In addition, due to the shape of the valley more precipitation is caught than elsewhere. Hence, $\Delta H_{01–08}$ has positive values, while the other points, at the ablation zone have negative $\Delta H_{01–08}$ values. The LV-3 profile points, north-south oriented and situated in the ablation zone of Las Vacas glacier, give negative $\Delta H_{01–08}$ values. The profile LV-4, north-south oriented, having a few points in the accumulation zone, has also negative $\Delta H_{01–08}$ values.

The Horcones Superior glacier (HS) is northwest – southeast oriented. Fig. 4 shows its profile HS-1, located in the accumulation zone. The results of profiles HS-1 and HS-2 show positive values for ice elevation change with an average rate of 0.35 m/a, while those of profile HS-3, located in the HS glacier ablation zone, show mass loss with an elevation change rate of −3.5 m/a.

The Las Vacas glacier shows a volume gain of +0.062 km^3 while the Horcones Superior glacier experienced a loss of −0.011 km^3. Tab. 6 shows areal and volumetric changes for both glaciers.

Tab. 6: Volumetric and areal variations in the glaciers in 2001–2008 period.

Glacier	Gain (km^3)	Loss (km^3)	ΔV_{01-08} (km^3)	ΔA_{01-08} (km^2)
Las Vacas	0.20	−0.147	0.053	−1.5
Horcones Superior	0.04	−0.055	−0.015	−0.55

Since these results are based only on 31 % of the profiles points, the use of independent references is essential to estimate the performance of the proposed approach. In this study, we analysed a relatively short period of time, and therefore, the author decided to extend it to a longer lapse to confirm the behaviour of the DTMs. Thus, a similar methodology was used to estimate the changes in ice elevation in the Piloto glacier in the 1974–2001 (ΔH_{74-01}) period. This glacier is located at the end of Quebrada de Matienzo (Fig. 5), in the upstreams of the Las Cuevas River, next to the Horcones valley. The Piloto glacier has been monitored with direct measuring methods for the past 30 years, thus providing a reliable annual mass balance series (Leiva 1982, Leiva et al. 2007). The DTM was created from a contour line model from 1974 (CLM_{74}), made by the Photogrammetry Department of the National University of San Juan through a photogrammetric data compilation, based on aerial photos from 1974 (1:10000 scale, 10 m contour interval). The elevation change in the glacier was calculated from (CLM_{74}) with respect to ASTER DTM_{01}, and compared with the values obtained from the Piloto glacier mass balance in the 1979–2001 period. According to Leiva et al. (2007), the accumulated balance in the Piloto glacier eastern tongue (PE) between 1979 and 2001 is −9.79 m of water equivalent (water equivalent (w.e.) considers a standard ice density of 850 kg/m^3), which yields an average rate of −0.44 m/a w.e. per year. The PE glacier mean ice elevation change (ΔH_{74-01}), calculated by the comparison of DTM_{01}-CLM_{74} gives a result of –15.40 m, which represents – 13.09 m w.e., giving an average rate of −0.48 m/a w.e. per year, a rather good match.

The difference between both rates of mass loss calculations is almost negligible considering the errors of the mass balance determination by the glaciological method, and thus supports the applicability of the photogrammetric approach.

6 Discussions and Conclusions

This study demonstrates that the generation of DTMs from ASTER optical images in areas with high topographic complexity, such as the Mt. Aconcagua region, is feasible and the quality of the DTM is adequate to estimate elevation and volumetric changes in glaciers. The proposed method produced acceptable results in difficult to access areas, which cannot be observed effectively and rapidly with conventional methods, and thus are rarely investigated. The validation of the DTMs through GPS checkpoints and profiles provided valuable information about the accuracy of derived products and how the slope can contribute to deformations and errors on DTMs.

The relative errors between the DTMs were minimized through a robust matching by a 3D conformal transformation, using segments of smaller sub-areas independently processed with parameters adjusted using stable points, such as rocky outcrop areas around the glaciers. Applying the transformation to co-register the two DTMs, the quality of the final results has improved, as shown in Fig. 3.

The glaciers showed a net ice mass loss for the 2001–2008 period even though the LV-1 profile and the HS-1 and HS-2 profiles, located at the accumulation zone of the glaciers, gave a small ice mass gain and simultaneously a decrease of their area. Another relevant issue is the differences between the results at both sites. This may be explained by the different orientation that is west–east in the case of Las Vacas and northwest–southeast in Horcones Superior, and also the different size, LV has a 19.4 km^2 while the HS has 5.6 km^2.The behaviour of a big glacier could be different compared to the small one. Another aspect could be the local conditions of each valley, the bedrocks, slope, the winds in the upper zone, drifting and accumulated snow in other areas. Therefore, it is important to take the non-photogrammetric aspects in subsequent studies into account, including shape of the cirque glacier, the winds patterns and temperatures.

Because only 31 % of the profile points passed a test for 3D deformation comparing ASTER imagery has certain limitations. To independently assess the performance potential of the introduced method for a longer period of time, a comparison with the results of mass balance on the Piloto glacier, where direct measurements provided reliable mass balances, lead to good results. Future work will further investigate the optimization of the re-

siduals and consider the cross performance evaluation of data obtained by different sensors.

As a final remark, it is important to note that the geodetic balances give acceptable results which can be adjusted and controlled from direct field data. However, the photogrammetric method has the advantage to easily cover places, even large areas with difficult access on the ground. Also, regular studies by direct mass balance measurements are significantly more expensive than the here proposed approach.

Acknowledgements

This work was supported by a grant from CONICET (Argentine National Research Council) PICT 5759/08. Additional support was provided by the SIGMA program (Geodynamics Research System Mt. Aconcagua). The author would like to thank Dr. Charles Toth, Dr. Juan Carlos Leiva and Dr. Matthias Braun for their review and comments, and Tec. Adalberto Ferlito for his help in the fieldworks. Also, the author thanks to Department of Natural Resources, Mendoza to provide the support in the Aconcagua Park.

References

Barrand, N.E., Murray, T., James, S.L. & Mills, J.P., 2009: Optimizing photogrammetric DEMs for glacier volume change assessment using laser-scanning derived ground-control points. – Journal of Glaciology **55** (189): 106–111.

Berthier, E., Arnaud, Y., Kumar, R., Ahmad, S., Wagnon, P. & Chevallier, P., 2007: Remote sensing estimates of glacier of mass balance in the Himachal Pradesh (Western Himalaya, India). – Remote Sensing of Environment **108:** 327–338.

Bolch, T., Pieczonka, T. & Benn, D.I., 2011: Multi-decadal mass loss of glaciers in the Everest area (Nepal Himalaya) derived from stereo imagery. – The Cryosphere **5:** 349–358.

Cimbaro, S.E. & Lauria, E.A., 2007: Adoption of an ITRF 2005 based frame as the National Geodetic Frame of Argentina. – Poster presented at IUGG XXIV General Assembly Earth, Our Changing Planet, Perugia, Italy, 2–13 July.

Estadísticas Meteorológicas, 1986: Periodo 1971–1980. – Servicio Meteorológico Nacional. Buenos Aires, Argentina.

Etzelmüller, B. & Sulebak, J.R., 2000: Developments in the use of digital elevation models in periglacial geomorphology and glaciology. – Physische Geographie **41**, Jahrestagung Winterthur.

Forbes, C., Evans, M., Hastings, N. & Peacock, B., 2011: **4th** Statistical Distribution. – 230 p., Wiley.

Fortes, L.P., Lauria, E., Brunni, C., Amaya, W., Sanchez, L., Drewes, H. & Seemeller, W., 2006; Current status and future developments of the SIRGAS project. – Wissenschaftlich Arbeiten der Fachrichtung Vermessungswesen der Universität Hannover **258:** 59–70.

Franceschetti, G. & Lanari, R., 1999: Fundamentals of Synthetic Aperture Radar Processing. – CRC Press LLC, Boca Raton, Florida, USA.

Fujisada, H., Bailey, G.B., Kelly, G.G., Hara, S. & Abrams, M., 2005: ASTER DEM Performance. – IEEE Transactions on Geoscience and Remote Sensing **43** (12): 2707–2813.

Haeberli, W., 2005: Mountain glaciers in global climate-relate observing systems. – Huber, U.M., Burgmann, H.K.H. & Reasoner, M.A. (eds.): Global change and mountain regions (a state of the knowledge overview): 169–175, Springer, Dordrecht, Niederlande.

Hirano, A., Welch, R. & Lang, H., 2002: Mapping from ASTER stereo imagery data: DEM validation and accuracy assessment. – ISPRS Journal of Photogrammetry & Remote Sensing **57:** 356–370.

Iwasaki, A. & Fujisada, H., 2005: ASTER Geometric Performance. – IEEE Transactions on Geoscience and Remote Sensing **43** (129).

IPCC, 2007: Intergovernmental Panel on Climate Change. – **26th** Session of the IPCC, Bangkok, Thailand.

Kääb, A., Huggel, C., Paul, F., Wessels, R., Raup, B., Kieffer, H. & Kargel, J., 2002: Glacier monitoring from ASTER imagery: accuracy and applications. – EARSeL-LISSIG-Workshop Observing our Cryosphere from Space: 43–53, Bern, Schweiz.

Kääb, A., 2008: Glacier volume change using ASTER satellite stereo and ICESat GLAS Laser altimetry. A test study on Edgeøya, Eastern, Svalbard. – IEEE Transactions on Geoscience and Remote Sensing **46** (10).

Koblet, T., Gärtner-Roer, I., Zemp, M., Jansson, P., Thee, P., Haeberli, W. & Holmlund, P., 2010: Reanalysis of multi-temporal aerial images of Storglaciären, Sweden (1959–1999) – Part 1: Determination of length, area, and volume changes. – The Cryosphere **4:** 333–343.

Lang, H.R. & Welch, R., 1999: Algorithm Theoretical Basis Document for ASTER Digital Elevation Models. – 69 p., version 3.0, Jet Propulsion Laboratory, Pasadena, CA, USA.

Lauria, E.A., 2009: República Argentina – Adopción del Nuevo Marco de Referencia Geodésico Nacional POSGAR 07–RAMSAC. – Novena Conferencia Cartográfica Regional de las Naciones Unidas para América, United Nations E/CONF.99/CRP.9, 10–14 August, New York, USA.

Leiva, J.C., 1982: Le glacier du Cajón del Rubio. – Ph.D. Thesis, Université Joseph Fourier, Grenoble, France.

Leiva, J.C., Cabrera, G.A. & Lenzano, L.E., 2007: 20 years of mass balance on the Piloto glacier, Las Cuevas river basin, Mendoza, Argentina. – Global and Planetary Change **59:** 10–16.

Liba, N. & Jarve, I., 2009: Making orthophotomosaic about Tartu city with PHOTOMOD Program and its geometrical quality. – FIG 2009 Working Week Report, Surveyors Key Role in Accelerated Development, Eilat, Israel.

Marzolff, I. & Poesen, J., 2009: The potential of 3D gully monitoring with GIS using high-resolution aerial photography and a digital photogrammetry system. – Geomorphology **111**: 48–60.

Miller, P.E., Kunz, M., Mills, J.P., King, M.A., Murray, T., James, T.D. & Marsh, S.H., 2009: Assessment of Glacier Volume Change Using ASTER-Based Surface Matching of Historical Photography. – IEEE Transactions on Geoscience and Remote Sensing **47** (7): 1971–1979.

Minetti, J. & Corte, A., 1984: Zonificación latitudinal del clima en la zona andina y su relación con el límite inferior del hielo perenne (LIHP) y del límite inferior geocriogénico (LIG). – Acta Geocriogénica **2**: 129–143.

Nuth, C. & Kääb, A., 2010: What's in an elevation difference? Accuracy and corrections of satellite elevation data sets for quantification of glacier changes. – The Cryosphere Discussion **4**: 2013–2077.

Nuth, C. & Kääb, A., 2011: Co-registration and bias corrections of satellite elevation data sets for quantifying glacier thickness change. – The Cryosphere **5** (1): 271–290.

Pieczonka, T., Bolch, T. & Buchroithner, M., 2011: Generation and evaluation of multitemporal digital terrain models of the Mt. Everest area from different optical sensors. – ISPRS Journal of Photogrammetry and Remote Sensing **66**: 927–940.

Rivera, A., 2004: Mass balance investigations at Glaciar Chico, Southern Patagonia Icefield, Chile. – Ph.D. Thesis, School of Geographical Sciences, University of Bristol, Großbritannien.

Racoviteanu, A.E., Manley, W.F., Arnaud, Y. & Williams, M.W., 2007: Evaluating digital elevation models for glaciological applications: an example from Nevado Coropuna, Peruvian Andes. – Global and Planetary Change **59:** 110–125.

Rózycki, S. & Wolniewicz, W., 2007: Assessment of DSM accuracy obtained by High resolutions stereo images. – ISPRS Hannover Workshop 2007, High Resolution Earth Imaging for Geospatial Information, 29 May–1 June, Leibniz Universität Hannover.

Schneider, D., Delgado Granados, H., Huggel, C. & Kääb, A., 2008: Assessing lahars from ice-capped volcanoes using ASTER satellite data, the SRTM DTM and two different flow models: case study on Iztaccíhuatl (Central Mexico). – Natural Hazards and Earth System Science **8:** 559–571.

Shan, J. & Toth, C., 2008: Topographic Laser Ranging and Scaning: Principles and Processing. – CRC Press, Taylor and Francis.

Sutti, J. & Torok, C., 1996: Testing 3D displacement vectors by confidence ellipsoids. – Acta Montanistica Slovaca, Rocnik **4:** 301–310.

Toutin, T., 2008: ASTER DEMs for geomatic and geoscientific applications: a review. – International Journal Remote Sensing **29:** 1855–1875.

Trombotto, D., 1991: Untersuchungen zum periglazialen Formenschatz und zu periglazialen Sedimenten in der ‚Lagunita del Plata', Mendoza, Argentinien. – Heidelberger Geographische Arbeiten **90:** 171 p., Heidelberg.

Vignon, F., Arnaud, Y. & Kaser, G., 2003: Quantification of glacier volume change using Topographic and ASTER DEMs. A case study in the Cordillera Blanca. – IGARSS' **2003:** 2605–2607, 21– 25 July 2003, Toulouse, France.

Wolf, P.R. & Dewitt, B.A., 2000: Elements of photogrammetry with applications in GIS. – Third ed., chapter 5, McGraw Hill, New York, USA.

Address of the Author

Dr. M. Gabriela Lenzano, Geomatics Department, Argentine Institute of Snow, Glaciology and Environmental Sciences Research (IANIGLA)-CCT, CONICET, 330 P.O. Box, 5500, Mendoza, Argentina, e-mail: mlenzano@mendoza-conicet.gob.ar

Manuskript eingereicht: Dezember 2012
Angenommen: März 2013

PFG 2013 / 3, 0209–0220
Stuttgart, June 2013

Article

Unsupervised Change Detection on SAR images using a New Fractal-Based Measure

Hossein Aghababaee, Jalal Amini, Teheran, Iran, Maio-Li Yu-Chang Tzeng, Maio-Li, Taiwan & Josaphat Tetuko Sri Sumantyo, Chiba, Japan

Keywords: change detection, fractal geometry, wavelet multi-resolution, SAR image

Summary: Change detection for land use/cover is very important in the application of remote sensing. This paper proposes a new fractal measure for automatic change detection in synthetic aperture radar (SAR) images. The proposed measure is computed based on the fractal dimension and intensity information. The fractal dimension is calculated using the wavelet multi-resolution analysis based on the concept of fractional Brownian motion. In the next stage, a binary decision is made at each pixel location to determine whether it is a change or not, by applying a threshold on the image derived from the proposed measure. The threshold is computed from the distribution of the proposed fractal measure using the well-known Otsu method. The proposed change indicator is compared to the classical log-ratio detector as well as two other statistical similarity measures, namely Gaussian Kullback-Leibler and cumulant-based Kullback-Leibler detectors. Experiments on simulated and real data show that the proposed approach achieves better results than the other detectors.

Zusammenfassung: *Unüberwachte Detektion von Veränderungen in SAR-Bildern mit einem neuen Fraktal-basierten Veränderungsmaß.* Die Detektion von Veränderungen der Landnutzung bzw. der Bodenbedeckung ist eine wichtige Anwendung der Fernerkundung. In diesem Beitrag wird ein neues Maß für die automatische Erkennung von Änderungen in Radarbildern mit synthetischer Apertur (SAR) auf Basis von Fraktalen vorgeschlagen. Dieses Maß wird aus der fraktalen Dimension und der Intensität der SAR-Bilder bestimmt. Die fraktale Dimension wird auf Basis einer Analyse mit mehrskaligen Wavelets berechnet und beruht auf dem Konzept der fraktalen Brownschen Bewegung. Anschließend wird in jedem Pixel eine binäre Entscheidung dahingehend getroffen, ob eine Veränderung vorliegt oder nicht, indem ein Schwellwert auf das Veränderungsmaß angewandt wird. Dieser Schwellwert wird aus der Verteilung des Veränderungsmaßes mit Hilfe der Otsu-Methode abgeleitet. Der vorgeschlagene Veränderungsindikator wird mit dem klassischen log-Verhältnis-Detektor sowie mit zwei anderen statistisch motivierten Ähnlichkeitsmaßen verglichen, nämlich mit dem Gaußschen Kullback-Leibler- und dem kumulierenden Kullback-Leibler-Detektor. Untersuchungen mit simulierten und realen Daten zeigen, dass der vorgestellte Ansatz bessere Ergebnisse liefert als andere verwendete Detektoren.

1 Introduction

Detection of the changes occurring on the Earth's surface by means of multi-temporal remote sensing images is one of the most important applications of remote sensing technology. It depends on the fact that, for many public and private institutions, the knowledge of the dynamics of either natural resources or man-made structures is a valuable source of information in order to make decisions. Satellite and airborne remote sensing sensors have proven to be particularly useful in addressing change detection applications related to environmental monitoring, agricultural surveys, urban studies, and forest monitoring (Bazi et al. 2005). In remote sensing earth monitoring, unlike optical sensors, SAR sensors can

www.schweizerbart.de
DOI: 10.1127/1432-8364/2013/0171 1432-8364/13/0171 $ 3.00

acquire data day and night regardless of the cloud cover. Furthermore, in comparison with the optical sensors, data obtained by SAR sensors show great potentials for monitoring applications in some cloudy regions. Moreover, SAR images contain additional information like image coherence by acquiring interferometric images while considering critical baseline length, which could be a nice feature for change detection. In remote sensing applications, change detection is the process of identifying the differences in the state of a land cover or land use by analyzing a pair of images acquired in the same geographical areas at different times (Singh 1989).

Change detection between two optical images can easily be addressed by using difference-based indices. However, this task is much more difficult when it comes to SAR images due to the speckle effect. It is worth mentioning that speckle can be modelled in spatial chaotic systems and characterized by its fractal dimension (Tzeng et al. 2007). In the case of SAR acquisitions, the standard detector is based on the ratio of images. Bujor et al. (2004) did a very interesting job by analyzing the higher order statistics for change detection in SAR images. They concluded that the ratio was useful for step changes and that the second and third order log-cumulants were beneficial for progressive changes appearing in consecutive images of multi-temporal series. Inglada & Mercier (2007) presented a similarity measure for automatic change detection in multi-temporal SAR images. This measure was based on the evolution of the local statistics for the images between two epochs. The local statistics were estimated using a cumulant-based series expansion which approximates the possible density functions in the vicinity of each pixel in the image. The evolution degree of the local statistics was measured using the Kullback-Leibler divergence. When only a Gamma distributed texture is considered, the first moment gave the complete evolution of the texture (Mercier et al. 2008). Unfortunately, texture in medium resolution SAR images does not always follow a Gamma distribution. Hence, using an improper model might result in poor performance. For interesting approaches related to the change measures in SAR images, the reader can refer to the works of Erten et al. (2012), Bovolo & Bruzzone (2008) and Shiyong et al. (2011).

The main problems of change detection in SAR images are as follows: 1) generating a change measure or a change indicator, 2) suppression of the speckle effect and 3) thresholding the change measure to produce a binary change map. The overall performance of the detection system will depend on both the quality of the change measure and the quality of thresholding plus the speckle effect. In order to deal with the speckle and the change measure problem, a new fractal measure is proposed. It combines the fractal dimension, which is computed by the wavelet multi-resolution analysis based on the concept of the fractional Brownian motion, with the intensity information provided by the original SAR images. Finally using a threshold, a binary decision is automatically taken at each pixel location to determine whether there is a change or not. This threshold is determined from the distribution of the fractal measures employing the well-known Otsu method (Otsu 1979). The main contribution of this paper is to propose a new fractal measure which utilizes both the original SAR image information and fractal dimensions simultaneously in an unsupervised change detection process.

Fractal geometry is able to describe complex forms and find out their underlying order. The concept of fractals was introduced by Mandelbrot (1982). It can be defined as an entity for which the Hausdorff-Besicovitch dimension exceeds the topological dimension. Simply speaking, the fractal dimension of a phenomenon is a measure of randomness or variability. This dimension is different from the traditional dimensions of Euclidian geometry. Another characteristic of fractals is self-similarity, which means that fractal dimension will be the same regardless of the measurement scale. Since 1989, fractals have been extensively adopted in satellite image processing (Cola 1989, Ramstien & Raffy 1989), and fractal models have been used in a variety of image processing and pattern recognition applications. For example, several researchers have applied fractal techniques to describe image textures, data fusion, and classification (De Jong & Burrough 1995, Myint 2003, Sun et al. 2005).

The rest of the paper is organized as follows: Section 2 introduces the proposed fractal measure and the Otsu method, section 3 presents the experimental results of applying the fractal measure to both simulated and real data, and section 4 concludes the paper, proposing some directions for future works.

2 Proposed Fractal Measure

As mentioned above, the main problems of change detection in SAR images are generating a change measure or some change indicators and thresholding the change measure so that a binary change map is produced. A new fractal measure is proposed to address the former and the speckle effect while the well-known Otsu method is adopted to deal with the latter. It is known that many natural surfaces show fractal behaviour within a certain range of scales. Such behaviour is summarized by the concept of fractal dimension, which can be related to the intuitive concept of surface roughness (Pentland 1984). Fractional Brownian motion (fBm) is the most suitable mathematical model for the random fractal found in nature. Specifically, a fBm surface function $V_H(x,y)$ is described by a random field having zero-mean Gaussian increments and satisfying the relation (Betti et al. 1997):

$$E\left[\left|V_H(x,y)-V_H(x+\Delta x,y+\Delta y)\right|\right]= \\ =\left\|(\Delta x,\Delta y)\right\|^H \quad (1)$$

In (1), $E[.]$ is the expected value, $\|.\|$ is the Euclidean norm, and H is he Hurst index, or persistence factor, controlling the roughness of the surface, with $0 < H < 1$. $H = 1$ corresponds to a smooth surface and $H = 0$, to a very rough texture; for $H = 0.5$ the ordinary Brownian motion is obtained. The fractal dimension D and the Hurst index H are related by (2.1), in which E is the Euclidean dimension. The Euclidean dimension for an image is 2 ($E = 2$), so the (2.1) can be written in the form of (2.2) (Peitgen & Saupe 1987):

$$D = E + 1 - H \quad (2.1)$$

$$D = 3 - H \quad (2.2)$$

Many researchers have already shown that the SAR signal is chaotic and follows fBm (Mcdonald et al. 2002, Goodman 1976). According to Tzeng et al. (2007), the SAR signals can be modelled by a nonlinear dynamic system and are characterized by their fractal dimension.

To find the changes between two SAR images that have been registered to each other, a new fractal change measure M_{fractal} is calculated from the normalized log-ratio of the intensities of two SAR images and the normalized difference of two fractal images (3).

$$M_{fractal}=\sqrt{\left|D_{I2}-D_{I1}\right|^2+\left|\log\left(\frac{I_2}{I_1}\right)\right|^2} \quad (3)$$

In (3), $|.|$ is the absolute value, I_2 and I_1 are the original SAR intensity images at two distinct times, and D_{I2} and D_{I1} are the corresponding fractal images. In addition to the intensity information, the proposed fractal measure considers the self-similarity character of SAR images via the fractal images. The fractal images provide information about the texture of the image, which means that the fractal measure is sensitive to texture changes.

To compute a fractal image for each pixel of the original SAR image, the fractal dimension D is estimated using the information inside a local window. Thus, the fractal dimension of each pixel depends on its neighbourhood. In this paper, a window of 7×7 pixels is used to measure D locally. Calculating the fractal dimension (or H) of remotely-sensed images with different methods gives different dimension values, because remotely-sensed images are not strictly self-similar and may, instead, be at most only statistically self-similar over a limited range of pixel sizes (Sun et al. 2006).

It has been shown that the wavelet analysis technique gives very accurate estimations of H in comparison to other classical methods (Stewart et al. 1993). The present method is derived from the peculiar form of the power spectrum of fBm. Since fBm is not a stationary process, fractional Brownian motion does not have a power spectrum defined in its classical sense. Nevertheless, fBm, being an isotropic random field, can be characterized by a random phase Fourier description that follows

a generalized power density of the form (Parra et al. 2003):

$$S(w_1, w_2) = \left| FFT(Window) \right|^2 . \quad (4)$$

In (4), w_1 and w_2 are the two axes in the frequency domain, S is the power spectrum and FFT is the fast Fourier transformation of the selected window. By filtering the frequency domain signal (S) with a wavelet filter, the resulting spectrum at a specific resolution j is (Mallat 1989):

$$S_{2^j}(w_1, w_2) = S(w_1, w_2) \left| \Psi_{2^j}{}^3(2^{-j}(w_1, w_2)) \right|^2 . \quad (5)$$

In (5), $\psi_{2j}{}^3(w_1,w_2) = \psi_{2j}(w_1)\ \psi_{2j}(w_2)$ corresponds to the 2-D wavelet associated to the diagonal details filter, and $\psi_{2j}(w_1)$ and $\psi_{2j}(w_2)$ are the one dimensional wavelet functions associated with the scaling functions $\phi(w_1)$ and $\phi(w_2)$ respectively (Mallat 1989). The subscript 2^j represents the specific resolution at which the wavelet filter is applied to the signal. The energy of the detailed signal (σ_{2j}) at a specific resolution j can be calculated by its summation in the support of $\psi_{2j}{}^3(w_1, w_2)$ of the chosen wavelet filter:

$$\sigma_{2^j}^2 = \frac{2^{-2j}}{4\pi^2} \sum_{-2^j\pi}^{2^j\pi} \sum_{-2^j\pi}^{2^j\pi} S_{2^j}(w_1, w_2) dw_1 dw_2 \quad (6)$$

The ratio of the energies corresponding to the detail signals at successive resolutions provides a solution for the computation of H as:

$$H = \frac{1}{2} \log_2 \left(\sigma_{2^j}^2 / \sigma_{2^{j+1}}^2 \right) . \quad (7)$$

In this work, H is computed using the energy of the detailed signal at the first two resolution levels ($j = 1$ and $j = 2$). After computing the Hurst index H according to (7), the local fractal dimension can be obtained by (2).

To sum up, the procedure for computing the fractal image is as follows.

In each location of the moving window:

1. Compute the power spectral density of the window according to (4).
2. Filter the computed power spectrum with a wavelet filter at two successive resolutions.
3. Measure the energy of the detailed signal at each resolution by summing up all of its elements (6).
4. Calculate fractal dimension related to the window using (7) and (2).

After computing the measure $M_{fractal}$ using (3), a binary decision is automatically made at each pixel location using a threshold derived from the histogram of $M_{fractal}$ using Otsu's method. Considering the fact that the change measure is presented by the intensity function $f(x,y)$ and the values of the measure are normalized between 0–255, the pixels on the measure can be divided into two classes $C_1 = \{0,1,\ldots,T\}$ and $C_2 = \{T+1, T+2,\ldots,255\}$ where the classes correspond to the foreground (objects of interest) and the background, respectively, and T is the desired decision threshold. The probabilities of the two classes are:

$$w_b(T) = \sum_{i=0}^{T-1} p(i), \quad w_f(T) = \sum_{i=T}^{255} p(i), \quad p(i) = \frac{n_i}{n} \quad (8)$$

In (8), w_b and w_f are the probabilities of background and foreground clusters, respectively, n_i is the number of pixels with the intensity i and n is total number of pixels in the given change measure image. Using discriminating analysis, Otsu (1979) showed that the optimal threshold T can be determined by minimizing the within-class variance (σ^2_{within}). This parameter is difficult to minimize, but it has been shown that the minimization of within-class variances is tantamount to the maximization of between-class variance ($\sigma^2_{between}$).

$$\sigma^2_{between}(T) = \sigma^2 - \sigma^2_{within}(T) = w_b(T)\ w_f(T)[\mu_b(T) - \mu_f(T)] \quad (9)$$

In (9), σ^2 is the variance of all image elements, which is constant (and not related to T), and μ_b and μ_f are the mean intensity values of background and foreground clusters, respectively. One should select the threshold T so that the between-class variance is maximized. Evaluating (9) for all possible values of T, the value that maximizes $\sigma^2_{between}$ is chosen as the final threshold.

3 Experimental Results

The proposed measure was compared to the classical log-ratio detector in order to evaluate its performance. Two other change measures, namely Gaussian Kullback-Leibler detector (Gaussian KLD) and cumulant-based Kullback-Leibler detector (cumulant-based KLD), introduced in (Inglada & Mercier 2007), are also compared. It should be noted that both Gaussian and cumulant-based KLD are computed using a 7 × 7 moving window. Experiments were carried out on both simulated and real data.

3.1 *Experiments with Artificial Change Image*

Simulations were performed to understand the behaviour of the detectors for a given type of change in a better way. As shown in Fig. 1(a), a HH polarized TerraSAR-X scene of Barcelona (Spain) (size: 400 × 400 pixels), taken on May 15, 2011 with 3 m spatial resolution was used. The images are publicly available at Astrium (2012). Three areas were changed by pasting values copied from some other area into the original image. This type of change can occur when there is a land-use change, anthropogenic activities, etc. (Inglada & Mercier 2007). The simulated change image is shown in Fig. 1(b). Changes in urban, agriculture, and water areas were simulated in the regions highlighted in Fig. 1(c). The change indicator or change measure can also be useful by itself. Indeed, the end-user of a change map often does not only want the binary information (changed vs. unchanged) but also an indicator for the intensity of change and eventually a confidence level. In this paper, the so-called receiver operating characteristics (ROC) curve is used to evaluate the quality of a change measure. The ROC plot shows the detection probability P_{det} as a function of the false alarm probability P_{fa} using different values of the threshold value T. The area under the ROC curve (AUC) is frequently used as a summary measure. The perfect ROC curve has an AUC of 1.

To evaluate the performance of change measures, different levels of speckle noise were artificially added to the SAR images to imitate the natural speckle in SAR images. The speckle noise was added using the multiplicative noise equation $J = I + \xi \cdot I$, where ξ is uniformly distributed random noise with mean 0 and variance v and J and I are the noisy and original images, respectively. In this work, the proposed fractal measure, log-ratio detector, Gaussian and cumulant-based KLD are computed from the TerraSAR-X images with noise added to them at three different levels corresponding to three values of v (0.01, 0.03, 0.05). Then the corresponding ROC curves are plotted in Fig. 2.

According to Figs. 2(a) to 2(c), the proposed fractal measure presents the best performance and the pixel-wise log-ratio detector shows the worst performance in all cases because, unlike

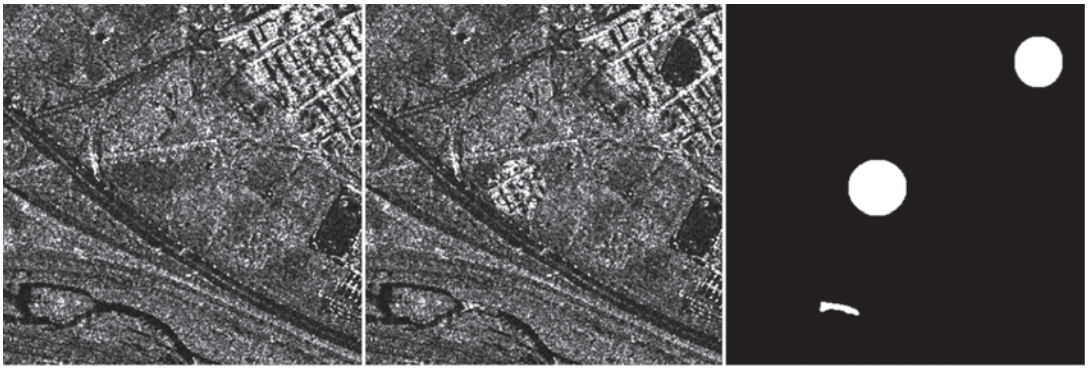

(a) Original SAR image (b) Artificial change image (c) Mask

Fig. 1: Simulation of changes on TerraSAR-X image.

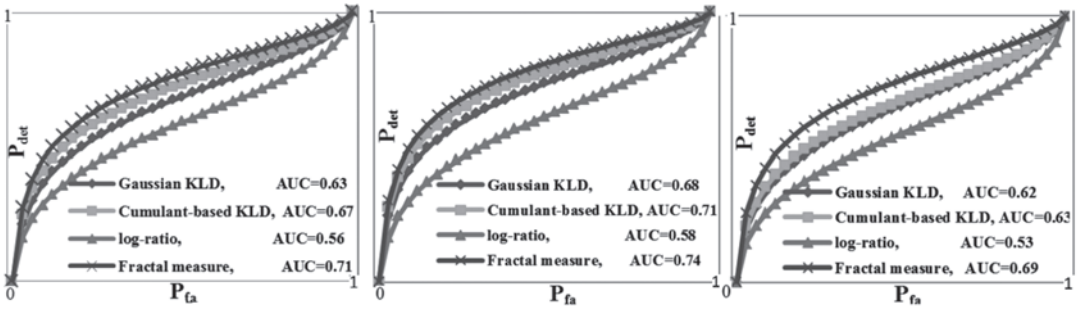

Fig. 2: ROC plot comparison of the four detectors for a simulated change in different speckle noise levels (ROC = receiver operating characteristics).

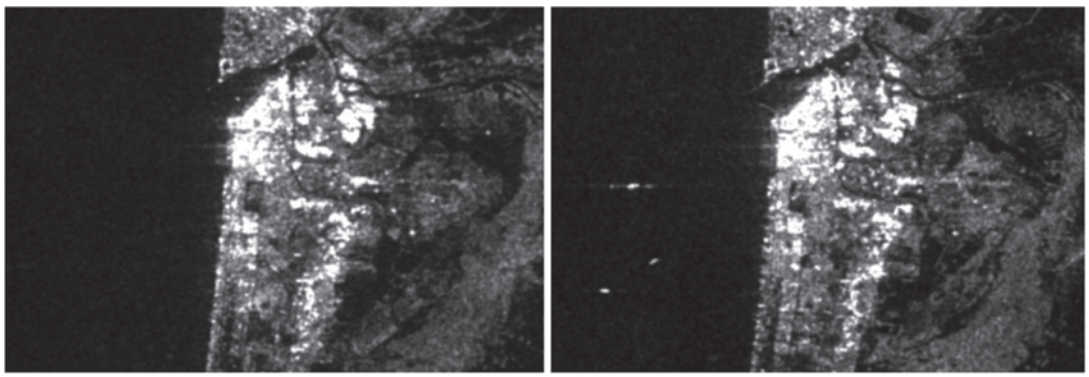

Fig. 3: Original JERS-1 images related to the first study area (Bandar-e-Anzali).

the other measures, the log-ratio image does not involve a window operation. The performance of each detector in different noise levels is quantitatively compared in Fig. 2 using AUC. Considering Fig. 2, it is clear that the fractal measure outperforms the others in different noise levels. Compared to other change detectors, the proposed fractal measure results in an improvement of up to 10 % in AUC (0.63 vs. 0.69 in Fig. 2(c)).

3.2 *Experiments with Real Data*

Two examples of applying the proposed method to real cases are presented in this subsection. The first study area is located in the north of Iran near the city of Bandar-e-Anzali. A pair of HH polarized JERS-1 images acquired in November 18, 1992 and April 4, 1997 with 18 m spatial resolution is shown in Figs. 3(a) and 3(b), respectively. The size of the images is 700 × 480 pixels. The proposed fractal measure, log-ratio detector, Gaussian and cumulant-based KLD are computed from the real dataset and a visual comparison of all measures is shown in Fig. 4. No speckle reduction was carried out, so that the resulting change measures are still affected by speckle. The quantitative comparison is made using the red and blue pixels, which are marked on the images showing the change measures (Fig. 4). The red and blue pixels represent the reference for change and unchanged regions, respectively. The reference regions for the change pixels (768 pixels) were selected in pier and residential areas, which were constructed in Anzali between 1992 and 1997, whereas the unchanged pixels (964 pixels in total) were obtained by manually analyzing the SAR images.

After determining the change measures, we derived a threshold according to the Otsu method for each measure (section 2), and we apply the thresholds to generate binary images showing at each pixel whether there is a

change according to the respective measure or not. Subsequently, all the resultant binary images are refined using a median filter with the size of 3 × 3 to remove single change pixels. The smoothed binary images are change maps in which changed and unchanged pixels are represented in white and black, respectively (Fig. 5). To compare the change detection performance quantitatively, user's and producer's as well as the overall accuracy of the change map are presented in Tab. 1.

As it can be seen in Figs. 4(a) and 5(a), the quality of the log-ratio detector is very poor and its result is unacceptable because it is seriously affected by the speckle. On the other hand, as demonstrated in Figs. 4(d), 5(d) and Tab. 1, the quality of the proposed fractal measure is more satisfactory than the other implemented methods. Apparently, speckle is modelled properly by the proposed fractal measure, and as a result its effect on the results is reduced. The change measure and change

Tab. 1: Quantitative comparison of the change maps in the first real dataset (Bandar-e-Anzali) (KLD = Kullback-Leibler Divergence).

	Unchanged		**Change**		
Overall Accuracy (%)	User's Accuracy (%)	Producer's Accuracy (%)	User's Accuracy (%)	Producer's Accuracy (%)	**Method**
73.2	93.0	56.1	63.2	94.7	**Log-Ratio**
83.3	82.1	89.6	85.3	75.4	**Gaussian KLD**
79.5	78.4	87.1	81.2	69.9	**Cumulant KLD**
89.7	85.7	97.8	96.7	79.4	**Fractal measure**

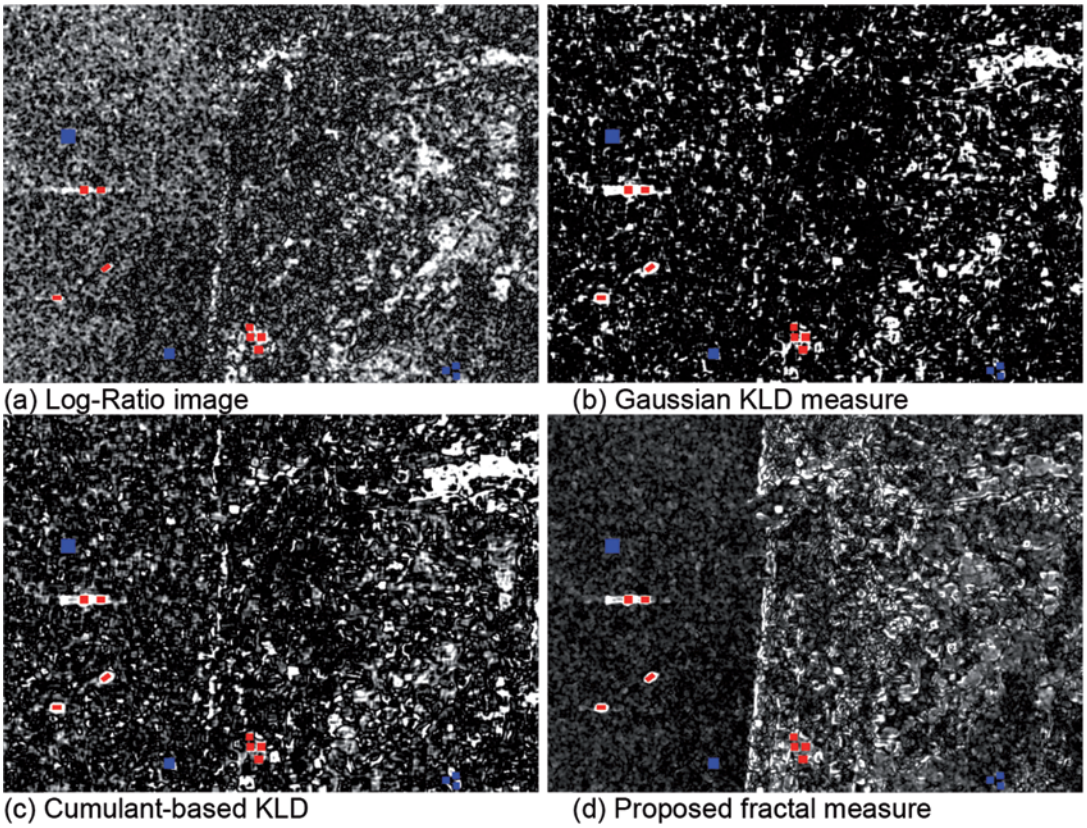

Fig. 4: Comparison of change measures. Red and blue pixels are reference regions for changed and unchange regions, respectively.

map of the Gaussian KLD are shown in Figs. 4(b) and 5(b), whereas the change measure and change map of the cumulant-based KLD are displayed in Figs. 4(c) and 5(c), respectively. The drawback of the Gaussian and cumulant-based KLD is that the SAR intensity statistics are not distributed normally and that employing an improper model might result in poor detection performance. The proposed fractal measure yields better performance in distinguishing changed and unchanged areas as compared to the Gaussian and cumulant-based KLD measures. It should be noted that the Gaussian and cumulant-based KLD and

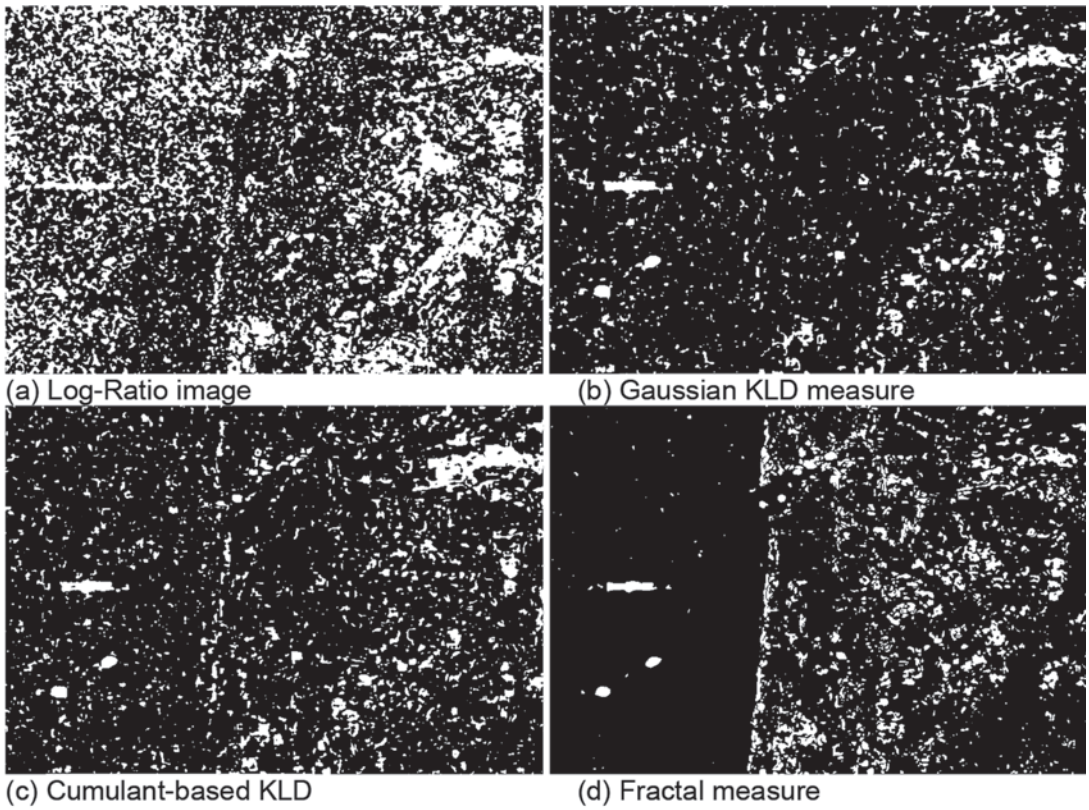

Fig. 5: Comparison of change maps obtained from different change measures for the change and unchange regions, respectively (KLD = Kullback-Leibler Divergence).

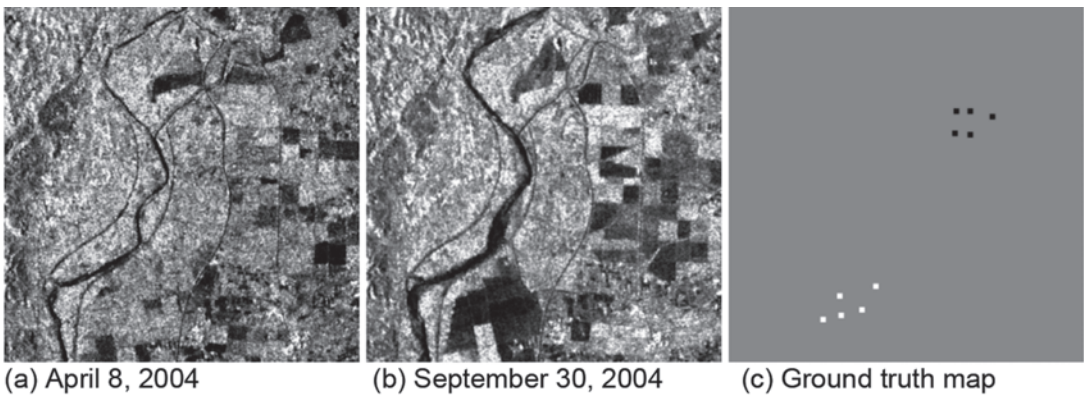

Fig. 6: Original ASAR alternative polarization mode (HV) images related to the second study area (Tuku).

also the proposed fractal measure are computed using the same window size (7×7). The high quality of the proposed fractal measure reveals that it can trace the changes regardless of the distribution model of the change intensity and gives satisfactory results in the presence of the speckle noise.

A quantitative comparison of the change detection algorithms is given Tab. 1, which is based on the reference regions in Fig. 4. The overall accuracy of the fractal measure (89.7 %) is better than the one achieved by the other implemented methods.

The second real dataset consists of a pair of ASAR images acquired in alternative polarization mode (HV) on-board ENVISAT in the area of Tuku (Taiwan). The original images were refined using enhanced Lee filter (Lopes et al. 1990) with a window size of 5 × 5 pixels. Fig. 6 displays the images of April 8, 2004 and September 30, 2004. The images have 30 m spatial resolution, and their size is 512 × 512 pixels. There are land cover changes due to both seasonal effects and agricultural practices. More than twenty survey sites located around a plantation field were identified

Tab. 2: Quantitative comparison of the change maps in the second real dataset (Tuku) (KLD = Kullback-Leibler Divergence).

	Unchanged		**Change**		
Overall Accuracy (%)	User's Accuracy (%)	Producer's Accuracy (%)	User's Accuracy (%)	Producer's Accuracy (%)	**Method**
92.8	96.9	94.2	76.7	86.3	**Log-Ratio**
97.0	96.9	99.5	97.5	85.3	**Gaussian KLD**
96.7	96.2	99.9	99.3	82.2	**Cumulant KLD**
97.6	97.3	99.9	99.3	87.5	**Fractal measure**

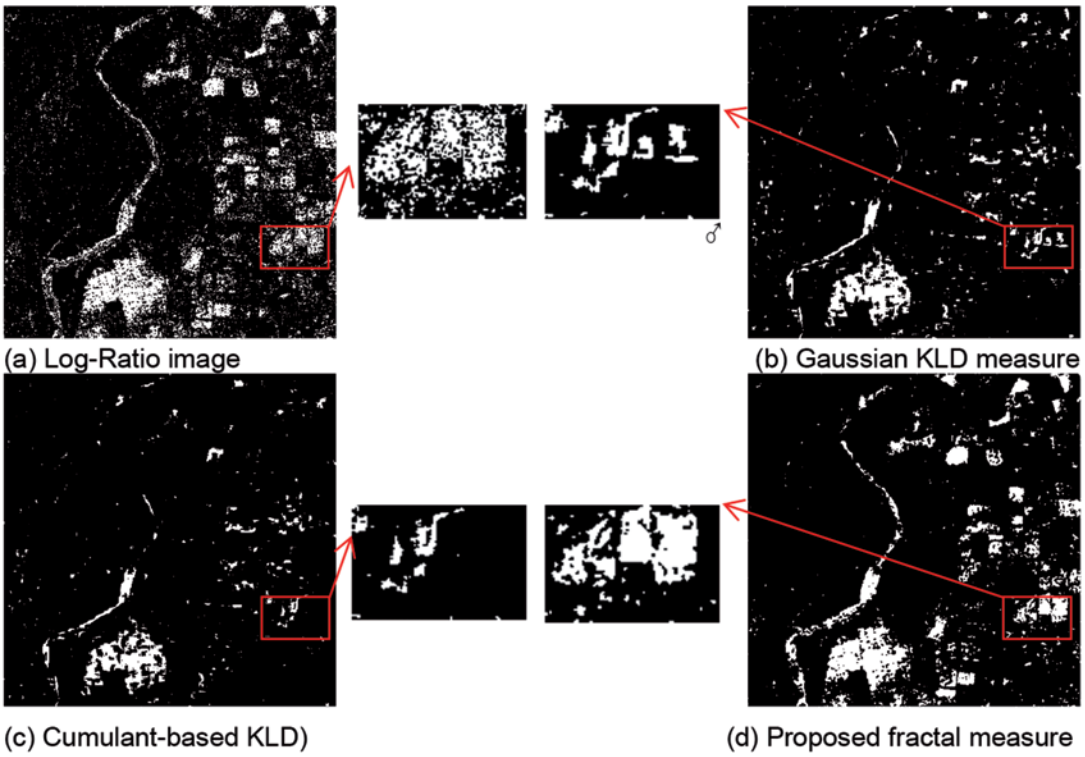

Fig. 7: Comparison of change maps obtained from different change measures.

for ground truth collections, aided by a land use map, an aerial photo, and SPOT images. In this test site, a total of seven land cover types were identified. They are: banana trees, grass, bare fields, rice fields, corn fields and rose fields. As these land cover types have changed frequently, the ground survey had to be conducted in accordance with the times the images were taken. There are 640 changed and unchanged pixels in the ground truth map (Fig. 6c), where white and black pixels correspond to the changed and unchanged areas, respectively. Each box contains 64 pixels.

Fig. 7 shows the change maps of the second test site using different change measures. As can be seen in Fig. 7 (a), the log-ratio gives many false detections. Comparing the results of Gaussian and cumulant-based KLD with the results of the fractal measure shows that the river and some landscape changes (in the right side of the image) were properly detected by the proposed measure because, unlike the statistical measure, the fractal measure can trace the changes regardless of a distribution model. A quantitative evaluation of the results is given in Tab. 2. The overall accuracy for the proposed method is 97.6 %. This value is slightly better than those achieved by the two KLD-based methods. The results of the evaluation based on the ground truth map shows the proposed measure's efficiency in comparison to the similarity measures and the classical log-ratio image.

4 Discussions and Conclusion

This paper proposed a new fractal measure for land use/cover change detection of SAR images. The proposed fractal measure is calculated by the combination of fractal and intensity information of original SAR images. Fractal dimension can be regarded as a statistical measure of the overall geometric complexity of image textures. So, the proposed fractal measure is sensitive to the texture changes. Applying a threshold to the proposed fractal measure, one can automatically take a binary decision at each pixel location to determine whether it is a change pixel or not. The threshold is computed from the distribution of the fractal measure using the well-known Otsu method. The proposed approach is compared to the classical log-ratio detector and other statistical similarity measures. Experiments have been carried out on both simulated and real data using different SAR images. Experimental results confirm the effectiveness of the proposed fractal measure. In particular, as expected, the proposed fractal measure is shown to be more suitable than the Gaussian and cumulant-based Kullback-Leibler detectors in distinguishing changed and unchanged areas. From the experimental results, it can be concluded that the main advantages of the proposed fractal measure are 1) that it uses both the fractal information and the intensity 2) that it is able to detect the change regardless of the distribution model of the change intensity, and 3) that it has high efficiency in change detection in various areas such as agriculture and water-bodies.

However, determining an optimal window size for fractal image computation is a question which still remains unanswered. Applying different window sizes may result in a different fractal dimension. It is more appropriate to use a smaller window in rough areas and a larger window for the smooth ones. Also, having the SAR images, the additional information like image coherence could be employed as a third index in the proposed measure. Such aspects will be studied as a future development of this work.

Acknowledgements

The authors would like to thank the venture business laboratory and the center for environmental remote sensing, Chiba University, Japan and National united university, Taiwan for the provision of the data. Also, we would like to extent our sincere appreciation to the reviewers and the editors for their great comments, which helped us to significantly improve the paper.

References

Astrium, 2012: http://www.astrium-geo.com/en/23-sample-imagery. – www.astrium-geo.com/en/23-sample-imagery (9.2.2013).

Bazi, Y., Bruzzone, L. & Melgani, F., 2005: An Unsupervised Approach Based on the Generalized Gaussian Model to Automatic Change Detection Multitemporal SAR Images. – IEEE Transaction on Geoscience and Remote Sensing **43** (4): 874–887.

Betti, A., Barni, M. & Mecocci, A., 1997: Using a wavelet-based fractal feature to improve texture discrimination on SAR images. – International conference on image processing **1:** 251–254.

Bovolo, F. & Bruzzone, L., 2008: An Adaptive Technique based on Similarity Measures for Change Detection in Very High Resolution SAR Images. – IEEE International Geoscience and Remote Sensing Symposium (IGARSS) **3:** 158–161.

Bujor, F., Trouvé, E., Valet, E., Niccolas, J. & Rudant, J., 2004: Application of log-cumulants to the detection of spatiotemporal discontinuities in multi-temporal SAR images. – IEEE Transaction in Geoscience and Remote Sensing **42** (10): 2073–2084.

Cola, L.D., 1989: Fractal analysis of classified Landsat scene. – Photogrammetric Engineering and remote sensing **55** (5): 601–610.

De Jong, S.M. & Burrough, P.A., 1995: A fractal approach to the classification of Mediterranean vegetation types in remotely sensed images. – Photogrammetric Engineering and Remote Sensing **61** (8): 1041–1053.

Erten, E., Reigber, A., Ferro-Famil, L. & Hellwich, O., 2012: A New Coherent Similarity Measure for Temporal Multichannel Scene Characterization. – IEEE Transactions on Geoscience and Remote Sensing **50** (7): 2185–2188.

Goodman, J., 1976: Some fundamental properties of speckle. – Journal of Optical Society of America **66** (11):145–1150.

Inglada, J. & Mercier, G., 2007: A new statistical similarity measure for change detection in multi-temporal SAR images and its extension to multi-scale change analysis. – IEEE Transactions of Geoscience and Remote Sensing **45** (5): 1432–1445.

Lopes, A., Touzi, R. & Nezry, E., 1990: Adaptive speckle filters and scene heterogeneity. – IEEE Transaction on Geoscience and Remote Sensing **28** (6): 992–1000.

Mallat, S.G., 1989: A theory for multi-resolution signal decomposition: the wavelet representation. – IEEE Transactions on Pattern Analysis and Machine Intelligence **11** (7): 674–693.

Mandelbrot, B.B., 1982: The Fractal Geometry of Nature. – W.H. Freeman and Company, New York.

Mercier, G., Moser, G. & Serpico. S.B., 2008: Conditional Copulas for Change Detection in Heterogeneous Remote Sensing Images. – IEEE Transactions of Geoscience and Remote Sensing **46** (5): 1428–1441.

Mcdonald, M.K., Varadan, V. & Leung, H., 2002: Chaotic behavior and non-linear prediction of airborne radar sea clutter data. – IEEE International conference of Radar: 331–337.

Myint, S.W., 2003: Fractal approaches in texture analysis and classification of remotely sensed data: Comparisons with spatial autocorrelation techniques and simple descriptive statistics. – International Journal of Remote Sensing **24** (9): 1925–1947.

Otsu, N., 1979: A Threshold Selection Method from Gray-Level Histograms. – IEEE Transactions on Systems, Man and Cybernetics **9** (1): 62–66.

Parra, C., Iftekharuddin, K. & Rendon, D., 2003: Wavelet Based Estimation of the Fractal Dimension in fBm Images. – IEEE International conference on neural engineering: 533–536.

Peitgen, H.O. & Saupe, D., 1987: The Science of Fractal Images. – Springer-Verlag, New York, USA.

Pentland, A.P., 1984: Fractal-based description of natural scenes. – IEEE Transaction on Pattern Analysis and Machine Intelligence 6 (6): 661–674.

Ramstien, G. & Raffy, M., 1989: Analysis of the structure of radiometric remotely-sensed images. – International Journal of remote sensing **10** (6): 1049–1073.

Shiyong, C., Mihai, D. & Gueguen, L., 2011: Information theoretical similarity measure for change detection. – Urban Remote Sensing Event (JURSE): 69–72.

Singh, A., 1989: Review Article: Digital Change Detection Techniques Using Remotely Sensed Data. – International Journal of Remote Sensing **10** (6): 989–1003.

Stewart, C.V., Moghaddam, B., Hintz, K.J. & Novak, L.M., 1993: Fractional Brownian motion models for Synthetic aperture radar imagery scene segmentation. – IEEE **81** (10): 1511–1522.

Sun, W., Xu, G., Gong, P. & Liang, S., 2006: Fractal analysis of remotely sensed images: A review of methods and applications. – International Journal of Remote sensing **27** (22): 4963–4990.

Sun, Y., Tian, J. & Liu, J., 2005: Two-band Infrared Data Fusion Method Based-on Fractal Dimension. – IEEE International Conference on Neural Networks and Brain **2:** 1197–1201.

Tzeng, Y.C, Chiu, S.H. & Chen, K.S., 2007: Change Detections from SAR Images for Damage Estimation Based on a Spatial Chaotic Model. – IEEE International Geoscience and Remote Sensing Symposium: 1926–1930, Barcelona, Spain.

Addresses of the Authors:

Hossein Aghababaee & Dr. Jalal Amini, Department of Surveying and Geomatic Engineering, University of Tehran, Iran, Tel.: +98-91-26443951, e-mail: {aghababaee}{jamini}@ut.ac.ir

Prof. Dr. Yu Chang Tzeng, Department of Electronic Engineering, National united university, Maio-Li, Taiwan, e-mail: john@nuu.edu.tw

Prof. Josaphat Tetuko Sri Sumantyo, Microwave Remote Sensing Laboratory, Center for Environmental Remote Sensing, Chiba University, Japan, e-mail: jtetukoss@faculty.chiba-u.jp

Manuskript eingereicht: Juni 2012
Angenommen: Januar 2013

PFG 2013 / 3, 0221 – 0237
Stuttgart, June 2013

Report

Automatic Detection and Classification of Objects in Point Clouds using multi-stage Semantics

Hung Quoc Truong, Helmi Ben Hmida, Frank Boochs, Mainz, Adlane Habed, Christophe Cruz, Yvon Voisin & Christophe Nicolle, Dijon, France

Keywords: 3D processing, point clouds, knowledge modelling, ontology, scene object classification

Summary: Due to the increasing availability of large unstructured point clouds obtained from laser scanning and/or photogrammetric data, there is a growing demand for automatic processing methods. Given the complexity of the underlying problems, several new methods try to use semantic knowledge in particular for supporting object detection and classification. In this paper, we present a novel approach which makes use of advanced algorithms to benefit from intelligent knowledge management strategies for the processing of 3D point clouds and for object classification in scanned scenes. In particular, our method extends the use of semantic knowledge to all stages of the processing, including the guidance of the 3D processing algorithms. The complete solution consists of a multi-stage iterative concept based on three factors: the modelled knowledge, the package of algorithms, and the classification engine. Two case studies illustrating our approach are presented in this paper. The studies were carried out on scans of the waiting area of an airport and along the tracks of a railway. In both cases the goal was to detect and identify objects within a defined area. With our results we demonstrate the applicability of our approach.

Zusammenfassung: *Automatische Detektion und Klassifikation von Objekten in Punktwolken unter Nutzung mehrschichtiger Semantik*. Infolge der zunehmenden Verfügbarkeit großer unstrukturierter Punktwolken aus Laserscanning und Photogrammetrie entsteht wachsender Bedarf für automatisierte Auswerteverfahren. Angesichts der häufig hohen Komplexität der in den Punktwolken enthaltenen Objekte stoßen rein datengetriebene Ansätze an ihre Grenzen. Es entstehen vermehrt Konzepte, die auf verschiedene Weise auch Gebrauch von der Semantik machen. Semantik und Algorithmik sind dabei oft eng miteinander verwoben und führen zu Limitationen in Art und Umfang der nutzbaren Semantik. Mit der vorgestellten Lösung werden Algorithmik und Semantik klar getrennt und mit den exakt auf diese Domänen zugeschnittenen Werkzeugen behandelt. Deren prozedurale Verknüpfung führt dann zu einem neuen Verarbeitungskonzept, das eine nach unserem Kenntnisstand bislang nicht erreichte Flexibilität und Vielseitigkeit in der Nutzung unterschiedlichster Semantiken besitzt und auch die Steuerung der Algorithmen integriert. Die iterative Gesamtlösung fußt auf drei Säulen, nämlich dem modellierten Wissen, dem Pool der Algorithmen und dem Identifikationsprozess. Erreichbare Resultate werden an zwei Beispielen dokumentiert. Ein Beispiel befasst sich mit der Analyse von Punktwolken aus dem Bereich der Lichtraumvermessung an Bahntrassen, das zweite mit Räumlichkeiten in einem Flughafen. In beiden Fällen müssen bestimmte Objektarten aufgefunden und klassifiziert werden.

1 Introduction

Object detection, recognition and reconstruction from digitized data, typically images and point clouds, are important tasks that find applications in many fields. Because such processing tasks are extremely laborious and difficult when carried out manually, it is of the utmost importance that they benefit from the support – or even be entirely performed

www.schweizerbart.de
DOI: 10.1127/1432-8364/2013/0172
1432-8364/13/0172 $ 0.00

through – numerical algorithms. Most existing algorithms are data-driven and rely both on extracting discriminating features from the dataset, and also on numerical models characterizing either geometric, e.g. flatness and roughness, or physical, e.g. colour and texture, properties of the sought objects. The numerical model and the extracted features are combined to form a decision. These methods are generally affected by the nature of dataset and the behaviour of the algorithms. Instead, it is up to the user to decide, often subjectively but generally based on one's experience, which algorithms are better suited for any particular kind of objects and/or the datasets. It goes without saying that the success of these approaches is significantly compromised by the increasing complexity of the objects and the decreasing quality of the data. Furthermore, relying on only a restricted set of features and individual algorithms to process the data might lead to unreliable results. One way to overcome the drawbacks of the data-driven approaches is to resort to the use of additional knowledge. For instance, knowledge characterizing the objects to be detected with respect to the data at hand or their relationships to other objects may generally be derived beforehand. Such knowledge not only allows for a systematic characterization and parameterization of the objects but also supports the quantification of the effectiveness of the algorithms to be used.

The work presented in this paper precisely aims at efficiently exploiting additional knowledge in the processing of point clouds. In particular, our work bridges semantic modelling and numerical processing strategies in order to benefit from knowledge in any or all parts of an automatic processing chain. Our approach is based on structuring various knowledge components into ontology containing a variety of elements taken from multiple sources such as digital maps and geographical information systems. However, we do not only rely on information about objects potentially present in the scene, i.e. their characteristics, a hierarchal description of their sub-components, and spatial relationships, but also on the characteristics of the processing algorithms at hand. During processing, the modelled knowledge guides the algorithms and supports both the analysis of the results and the object classification. Knowledge is also used to support the choice among different algorithms, the combination of these, and the adopted strategies. Our main contribution is a comprehensive set-up to model and use knowledge from various domains and to let it interact and contribute to all steps of an object detection process. This starts with inferring steps controlling algorithms based on object and scene related knowledge in order to select adapted algorithmic strategies and ends with a knowledge-based object classification and simultaneous extension and updating of the knowledge base (KB).

Our paper is structured as follows. An overview of the relevant literature on the topic is presented in section 2. Our proposed solution is outlined in section 3. Knowledge building and knowledge management are discussed in section 4. Section 5 is dedicated to our knowledge-based strategy for object detection and classification. This is followed by two case-studies involving real-world examples in section 6. Our conclusion and future work are given in section 7.

2 State of the Art

Early 3D processing techniques were either data-driven or model-driven and often based on statistical approaches. Many such methods, generally based on fitting techniques employing local or global optimization and statistical regression, often in conjunction with the random sampling consensus (RANSAC) algorithm for robustness, have attracted and continue to attract significant attention (Nurunnabi et al. 2012). However, many data-driven methods, in particular those relying on the segmentation of data into primitive shapes, are known to be highly sensitive to noise as well as to local deformations (Tarsha-Kurdi et al. 2007). Model-driven approaches, while less sentitive to local irregularities, require reliable geometrical models which are often difficult to obtain especially when dealing with complex scenes (Huang et al. 2011). However, despite of the robustness and efficiency of many such processing algorithms, they cannot resolve ambiguities when assigning semantic

labels to objects in a scene. Such ambiguities can be efficiently dealt with when integrating semantic knowledge with data processing (see for instance Busch et al. 2005, Helmholz et al. 2012).

As far as feature-based object recognition is concerned, some of the approaches have been used both in 2D images and in 3D data. For instance, Vosselman & Dijkman (2001) made use of higher level 3D features such as simple roof shapes, i.e. flat roofs, gable roofs and hip roofs, which are generally present in building structures. The authors relied on the use of the 3D Hough transform to detect planar roof faces in point clouds, and hence reconstructed the scene in a higher level of abstraction. Their segmentation strategy was based on detecting intersecting lines and "height jump edges" between planar faces. Pu & Vosselman (2006) used segmentation and feature extraction algorithms to recognize building components such as doors, walls, windows from point clouds. Based on constraints on these components, they were able to determine the categories to which each extracted feature belonged. However, the results were not satisfactory if the data did not clearly describe an object due to either the presence of noise or occlusions.

An important processing approach, which partly solves some limitations of data-driven methods, makes use of artificial intelligence techniques to enforce the robustness of the processing and to allow for the recognition of more complex objects. A typical work in this category is the one presented by Anguelov et al. (2005) in which object segmentation and classification are obtained by a learning procedure employing Markov random fields and quadratic programming. Such methods generally require a large number of training datasets in order to obtain good results.

Building on the above results, significant improvements have been achieved in 3D data processing by additionally incorporating semantic aspects. The method proposed by Cantzler et al. (2002) relies on a semantic network defining the relationships between objects in a scene such as walls being perpendicular to the floor and rules which the extracted features must obey. However, problems arise when dealing with complex indoor scenes possibly including many types of objects. Hedau et al. (2010) located objects of a specific geometry in an indoor scene. The detector computes the 3D location of an object along with its orientation using the geometry and the mutual arrangement of the object and the scene as well as a single image. Although quite useful for scene understanding, such an approach is limited to dealing with the case of a single object in the scene.

Localizing multiple objects in a scene has proved to be a difficult and challenging problem that often requires considering spatial and/or semantic relationships between objects. One way to address such problem is to resort to the use of semantic knowledge. The ability to exploit semantic knowledge is limited when the number of objects becomes large as it requires an adequate way of structuring properties of objects and relationships between them. In some approaches, this is carried out through a hierarchical description of the attributes of each object and those of the scene. For instance, Teboul et al. (2010) segmented building facades using a derivation tree representing the procedural geometry, and connected knowledge representation by grammars with machine learning. Furthermore, this approach proposed a dynamic way of performing a search through a perturbation model. Ripperda & Brenner (2006) also extracted building facades using a structural description and used reversible jump Monte Carlo Markov chains (Green 1995) to guide the application of derivation steps during the building of the tree. Another application of using knowledge is to infer the missing parts with detected parts. For example, Pu & Vosselman (2009) reconstructed building facades from terrestrial laser scanning data. Knowledge about size, position, orientation and topology is used to recognize features, e.g. walls, doors and windows, and also to hypothesize the occluded parts. In a similar work (Scholze et al. 2002), a model-based reconstruction method was proposed. In this method, semantic knowledge is also used to infer missing parts of the roof and to adjust the overall roof topology. These approaches use knowledge to evaluate results of numerical processes, but do not integrate it into the processing as such.

Since the use of knowledge is also useful within the processing chain, other works have

focused on knowledge management within computation. For example, Maillot & Thonnat (2008) used a visual concept ontology composed of visible features such as spatial and relationships, colour and texture to recognize objects by matching numerical features and visual concepts. Durand et al. (2007) proposed a recognition method based on an ontology which has been developed by experts of the domain; the authors also developed a matching process between objects and the concepts of ontology to provide objects with a semantic meaning. Interest also grows in developing knowledge-based system for various data processing tasks such as data segmentation and registration but also for scene understanding and interpretation. For instance, Trinder et al. (1998) proposed a knowledge-based method which automatically extracts roads from aerial images. The description of roads includes radiometric, geometric properties and spatial relationships between road segments, all formulated as rules in PROLOG. The knowledge base stores structures of roads and relationships between them extracted from images. By using topological information of road networks, the method is able to predict missing road segments. However, the used semantic model is limited to one type of objects (roads). Growe & Tonjes (1997) presented a knowledge-based approach for the automatic registration of remotely sensed images. Knowledge is explicitly represented using semantic nets and rules. Prior knowledge about scene objects and a geographic information system (GIS) are used to select and match the best set of features. Matsuyama (1987) proposed a method for automatic interpretation of remotely sensed images. The approach emphasises the use of knowledge management and control structures in aerial image understanding systems: a blackboard model for integrating diverse object detection modules, a symbolic model representation for 3D object recognition, and integration of bottom-up and top-down analyses. Two kinds of knowledge are considered in their expert system: knowledge about objects and knowledge about analysis tools, e.g. image processing techniques. Rost & Münkel (1998) proposed a knowledge-based system that is able to automatically adapt image processing algorithms to changes in the environment. The method uses expert knowledge that is explicitly formulated by rules. Depending on a given task, the system selects a sequence of relevant image processing tools and adjusts their parameters to obtain results with some predefined quality goals. Results on object contour detection, carried out in various conditions, show the benefit of taking into account expert knowledge for adjusting the parameters of various image processing operators. However, knowledge in these approaches has not been fully exploited: other capabilities, such as processing guidance, have not been explored.

Knowledge-based methods have the ability to not only manage and exploit geometric and/or topological relations between objects, but also to embed scene structures into semantic frameworks. Such knowledge is often translated into geometric constraints that can be used to improve object detection. Various kinds of knowledge-based methods have appeared for applications in object detection, demonstrating a clear and increasing interest for such approaches. This expresses a certain expectation about the role of semantics in future processing solutions. A step forward towards benefiting from the use of knowledge in such solutions would be a comprehensive approach that exploits knowledge in all processes, i.e. in guiding the numerical processing, evaluating, and classifying detected objects. Such an approach is proposed in this paper.

3 System Overview

When attempting to build an integrated approach with knowledge directing all parts of the process, several aspects have to be considered. At first, the whole process needs to be incorporated into a knowledge management tool. Therefore, it is necessary to have a process guiding all individual steps, leading from an initial situation to the final result. Inside this overall process, one part has to cover the numerical processing and another part has to handle the processing results. This latter part has to evaluate the results, draw conclusions about what has been found, and also what this means for further processing. This includes the need to update the content of the database

with the objects that have been found. This database has to be managed in a way that every detected object is transferred from some initial state to a final one within the framework of a rule-based system.

The main components of our system are illustrated in Fig. 1. The adopted strategy is applied to the analysis of 3D point clouds, but can also be extended to other data sources. It is based on explicitly formulating prior knowledge of the scene, on spatial relations of objects and on processing algorithms. It is a multi-stage concept based on three components: the modelled knowledge (Fig. 1 left), the package of algorithms (Fig. 1 top-right) and the classification engine (Fig. 1 bottom-right). In the initial stage, the available knowledge is transferred into a KB. Starting from this initial stage, an update process, which invokes the algorithms and the classification engine, is launched. Here, the algorithm selection module (ASM) guides the processing via selecting a set of processing algorithms based on the nature of the target objects, and produces new elements which can be identified. These elements are passed on to the classification engine, which, based on the existing knowledge expressed in the ontology, attempts to apply Semantic Web Rule Language (SWRL) (Horrocks et al. 2004) rules and description logic (DL) constraints in order to identify the nature or object category of the elements. This classification handles the output obtained from the algorithms. The result of the classification step updates the KB by inserting newly classified or updating already existing elements before running the next stage of processing. The process ends either when all objects are detected and classified or in absence of any change in the annotation process for a predetermined number of iterations (whose values remain at the discretion of the user).

Objects are represented by a point cloud or possibly data from other sources. Such data depend on many factors such as the type of the sensing system and the measuring/capturing conditions. This representation has to be handled by algorithms which also depend on many additional factors, e.g. noise, other data characteristics, and already existing objects. Strong interrelationships among these factors have a direct influence on the efficiency of the detection and classification processes. The more flexibly these factors and interactions are controlled, the better results are to be expected. For these reasons, knowledge from different domains is required and the quality of these various knowledge sets has significant impact on the results (Ben Hmida et al. 2011). Our solution relies on four main knowledge categories to construct the core of the KB: the scene knowledge, the spatial knowledge, the data knowledge and the algorithm knowledge. Each field of knowledge is represented by circles in Fig. 1, and relationships between these concepts are represented by directed edges. The scene knowledge contains information related to the content of the scene to be processed, important characteristics of objects, e.g. geometric features, appearance

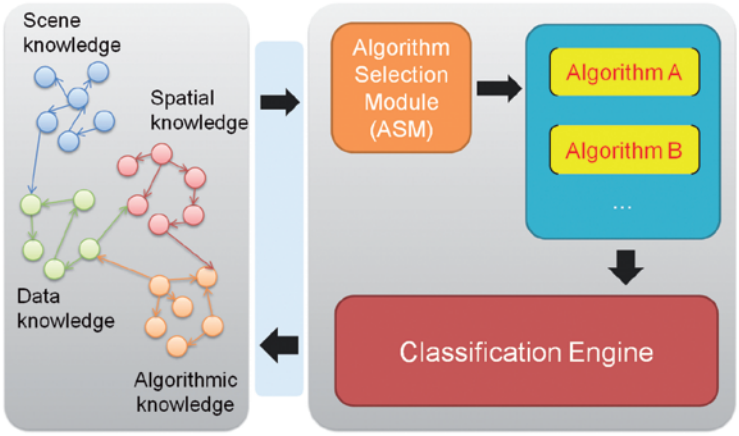

Fig. 1: System architecture.

and texture, and the geometry that composes its structure. Such knowledge is not only important for identification and classification processes but also supports the selection and guidance of the algorithms. The spatial knowledge models the relationships between objects in the scene. It is an important factor for the classification process because it supports an object's state disambiguation based on its relationship with the common environment. The data knowledge expresses important characteristics of the data itself. Finally, algorithm knowledge characterizes the behaviour of algorithms and determines which purpose they fulfil, which input is expected, which output is generated, and which geometries they are designed for. Based on this knowledge, a dynamic algorithm selection is possible allowing for a dynamic adaptation to processing situations given from other domains (Fig. 1).

4 Building Knowledge

The concept requires efficient methods for knowledge representation, management and interaction with algorithms. Efficient knowledge representation tools are available from the semantic web framework, which expresses knowledge through the web ontology language (OWL) (Bechhofer et al. 2004). The encapsulation of semantics within OWL through description logics (DLs) axioms has made it an ideal technology for representing knowledge from almost any discipline. We use the OWL to represent expert knowledge about the scene of interest and for algorithmic processing. With OWL ontology, we are able to describe complex semantics of a scene. For instance, the statement "A railway track is a linear feature with two linear structures running parallel to each other within a certain distance" can be expressed through logical statements. Likewise, we define the semantics of algorithmic processing within OWL. For example, the *CheckParallel* algorithm is designed for detecting a *Signal*, which contains parallel linear structures.

$$CheckParallel \exists isDesignedFor.Signal \sqcap Signal.hasParallel.\{true\} \quad (1)$$

As an additional technology, SWRL is available. It is a program which infers logic from the KB to derive a conclusion based on observations and hypotheses. For instance, the following rule (2) asserts that a detected element of class *Geometry* which has a distance from *DistanceSignal* of 1000 m, has a height equal to or greater than 4 m, and which has a linear structure, will be inferred as a *MainSignal*.

$$\begin{aligned} &Geometry(?x) \wedge hasLine(?x, ?l) \\ &\wedge line(?l) \wedge DistanceSignal\ (?y) \\ &\wedge DistanceFrom(?x, ?y, ?dis) \\ &\wedge swrlb{:}GreaterThan\ (?dis,1000) \\ &\wedge hasHeight(?x, ?h) \wedge swrlb{:}GreaterThan \\ &(?h, 4) \rightarrow MainSignal(?x) \end{aligned} \quad (2)$$

Variables are indicated by the standard convention in which they are prefixed by a question mark symbol (e.g. *?x*). An important SWRL feature is its ability to allow user-defined built-ins, i.e. user-defined predicates, such as, *swrlb:equal* and *swrlb:lessThan*, that can be used in SWRL rules, which help in the interoperation of SWRL with other formalisms and provide an extensible infrastructure for knowledge-based applications.

The techniques mentioned above serve as tools to formalize the identified and acquired knowledge. As explained, the actual solution handles four separate domains: the scene knowledge, the spatial knowledge, the data knowledge and finally the algorithm knowledge. All these knowledge domains have their representations in the domain ontology and participate in the whole processing cycle. The graphical structure of the top-level concepts of the ontology is given in Fig. 2, where we find four main concepts, called *Classes* in the next paragraphs. In order to proceed, these classes have to describe the different actors used during the detection and the classification process in a structured hierarchical way. The main factors that have to be modeled are: processing algorithms, point cloud data or image resources, and target objects with their geometry and characteristics. The class *DomainConcept* represents the different objects found in the target scene and can be considered the main class in this ontology. This class is further specialized into classes representing the different

detected objects. The other classes are used to either describe the object geometry through the *Geometry* class by defining its geometric component or to describe its characteristics through the *Characteristics* class. Ultimately, the system selects algorithms for the processing chain based on their compatibility with the object geometry and characteristics read from the *Algorithm* class.

Knowledge of different domains is acquired from the relevant sources. Domain experts are the most reliable knowledge sources. However, information sources such as CAD, GIS data, or other available documents in the case of detailed input can also be used to extract knowledge. In our case, the algorithm knowledge is acquired by experts in numerical processing and the scene knowledge is acquired from existing digital documents as a CAD drawing or GIS dataset.

The scene knowledge is described in the schema of ontology and includes semantics of the objects such as properties, restrictions, relationships between objects and geometries. The more information about an object is created and used, the more accurate the detection and classification process is. An example of defining a semantic object is the following: an electric pole (type 2) along a railway track has a height above ground between 4 m and 6 m; it comprises a vertical structure that connects to a cube on the ground; at the top, there are two parallel linear structures; and along the tracks, the distance from an electric pole (type 2) to a signal column is 1000 m within the bounds of a predefined tolerance, for example ± 0.5 m, depending on the quality of data, measurement uncertainty and noise.

Knowledge about 3D spatial relationships is used to enhance the classification process. Information about how objects are scattered in a 3D scene makes the detection and classification easier. For instance, given the detection of a wall, the probability of detecting doors or windows is higher. 3D spatial knowledge includes standards like the 3D topologic knowledge, 3D metric knowledge and 3D processing knowledge. Spatial knowledge contains relationships such as *disjoint*, *contain*, *inside*, *cover*, *equal*, *overlap*. The terms represent the geometric relations between components of an object or between objects. Each of the mentioned types of spatial knowledge contains a variety of relations modelled in the ontology structure. The top level ontology is designed to include the topological relationships. This is used to enrich an existing KB to make it possible to define topological relationships be-

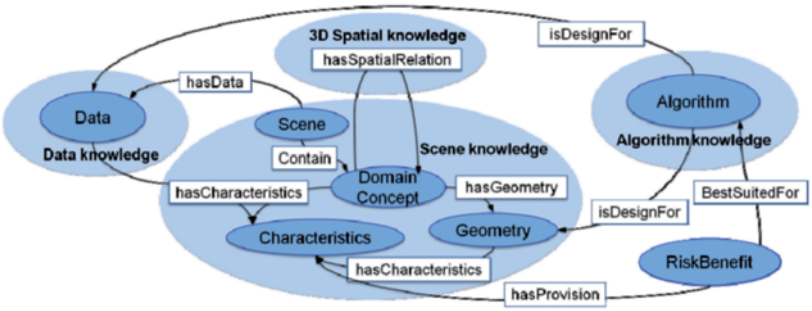

Fig. 2: General ontology schema overview.

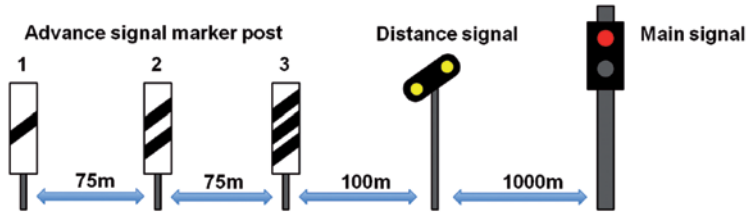

Fig. 3: Metric rules.

tween objects in a specific case. Metric knowledge presents important information, because the different elements fulfil very strict metric rules which can also be used for the detection and classification process. In the example of scenes specific for railways, Fig. 3 shows an ontological structure supported by the SWRL rules which can automatically specify that an object with certain characteristics that has a distance of 1000 ± 0.5 m from *Distance signal,* can be a *Main signal.*

Regarding the numerical processing algorithms, effectiveness depends on the quality of the data (resolution, noise), the characteristics of the object that needs to be detected, or other factors depending on a specific case. Algorithms are modelled under specialized classes of algorithms, sharing certain taxonomical and relational behaviour. The hierarchical representation of the algorithms is addressed by dividing the algorithms according to the context in which they are executed. Classes, including *GeometryDetection*, *AppearanceDetection*, *ImageProcessing* and *NoiseReduction*, follow such a hierarchal structure. Likewise, relational semantics are represented by properties. In broader terms, there are two types of relationships: one which applies to the geometry that an object in *Domain Concept* possesses, and one which relates distinct objects. The first category of relationships is used for detecting geometries. The object property *isDesignedFor* maps algorithms to the respective geometries. For example: *LineDetection1 isDesignedFor lines*. The second set of algorithm properties *hasInput/hasOutput* are inter-relational properties to connect algorithms based on the compatibility of output from an algorithm to the inputs of others.

It is necessary to adapt the processing parameters depending on data, scene and characteristics of objects to enable a well focussed detection and classification. The concept allows for these interactions, as it is able to automatically change the strategy based on a compromise between quality and risks. A part of the KB is dedicated to risk-benefit factors that have an influence on the algorithms. This was derived from "trial and error" simulations with every individual algorithm. Since an algorithm may perform best with some given parameters in one setting, and fail to deliver the same quality in other settings, it is important to assess the risk-benefit factors of every algorithm with various possible settings. The class *RiskBenefits* includes all identified risks and benefits. The class contains the four instances *Distinct*, *Illusive*, *Noise*, and *DetectionError*. The instances are the risks or the benefits with some influence on the algorithms or at least on the parameters of the algorithms. Note that the classes above form an ontology, which can also be used for other domains, such as creation of semantic annotated maps by a mobile robot, mobile mapping of street furniture or forests, and semantic place labelling from airborne laser data.

Knowledge modelling and human interaction: The process of modelling knowledge requires the user to collect "information" from related domains. This process is currently carried out manually. "Collecting information" can imply extracting knowledge from various sources or filling the ontology with objects corresponding to specific classes, object properties, algorithms, algorithmic properties, etc. Some of these tasks such as data extraction from technical documents have the potential to be done automatically using specialized processing tools borrowed from the document analysis community (Tang et al. 1996). Depending on the available tools and target application including its related domains, the knowledge modelling process may take a single person from one to several days of work (data extraction and ontology modelling) including interaction with domain experts and modelling all relationships. Examples for the length of this process and the amount of human interaction are given in section 6. However, although such figures may seem significant, one has to keep in mind that knowledge modelling for a given application is done only once and used for processing numerous point clouds with virtually very little or no changes to the ontology. Other approaches such as those based on machine learning would also require a significant amount of preparation to extract training data and carry out annotations generally from large amounts of scans, which may require at least as much time as modelling an ontology. This is especially true when dealing with special environments such as railways or industrial plants, which are often

subject to regulations, which require a certain level of expertise.

5 Knowledge Guidance for the Object Detection and Classification Process

5.1 *Knowledge-driven Strategy*

The knowledge formalization is based on the understanding of the underlying semantics and processes it using technologies such as OWL. The top-level ontology presents the main knowledge framework and holds generic semantics for all addressed domains. Regarding the case studies, this framework contains the scene, object geometries, spatial relations and algorithms and originates from existing knowledge sources, such as information systems, or guidelines of the Deutsche Bahn (DB, German Railways), and an extensive study of the sample scenarios. Obviously, quality and completeness of such formalized knowledge strongly influence the quality of the results, and have to be adapted to the individual application. In the general case, such a framework only contains the abstract and general knowledge of object categories, the structure of a scene, geometric relations between objects, the structure of data, the nature of algorithms and the potential relationships between these components. In a simpler scenario with specific information about potentially existing objects, for example known through CAD or Industry Foundation Class (IFC) files, the detection strategy can be guided more easily and may be reduced to a change detection problem.

Starting from the initial situation, the process iteratively updates the KB at certain stages. At the beginning of each iteration, the content of the KB is used to detect new features, may it be a new object or a component of it. These new geometric features are passed on to the KB in order to extend the KB for the following classification. This classification is guided by the content and the structure of the KB, which has reasoning capabilities based on property restrictions or rule languages (such as SWRL) and refines the actual content. This refined content is used in the next iteration. The process is repeated until all entities have been completely annotated and meet the following convergence conditions: (1) All objects defined on the KB are detected and annotated (simple change detection). (2) A predefined number of iterations without refinement for any entity has been reached.

5.2 *Usage of Algorithms guided by Knowledge*

Object related knowledge does not influence classification only, but also algorithmic processing. Different algorithms are designed for different contexts. The differences can be addressed and properly modelled. The KB holds the algorithm knowledge in the class *Algorithm*. This class is related to other classes inside the KB, such as objects. This allows for the modification of the role of algorithms, e.g. parameter, sequences, corresponding to the KB details. The interrelationships among different algorithms are mapped through compatibility of their input and output characteristics (Fig. 4). Fig. 4 illustrates that more than one path from an initial algorithm to a desired one exist. We use the well-known Djikstra's algorithm (Djikstra 1959) for finding the shortest path in the graph leading to the desired algorithm. This approach has the advan-

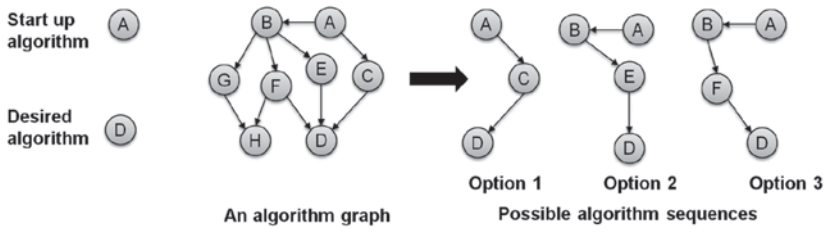

Fig. 4: Algorithm sequences extracted from the graph.

tage of preventing the sequence of algorithms to form an endless loop and allows for finding an appropriate sequence.

At any given iteration, each entity in the KB may be assigned a new label: *identified*, *unknown* or *ambiguous*. This label may change in the course of an iteration. Based on this information, the ASM chooses the best algorithm for generating new characteristics, which will help in the next classification step. This selection also integrates the choice of an optimal sequence out of several possible ones (routes) of algorithms (or nodes). Various knowledge components can have an impact here, e.g. data (noise, point density, point of view), object (size, shape, orientation), and scene (possible objects, neighbourhood).

5.3 *Classification Step*

As discussed in section 4, the ontology schema holds the semantics of the objects such as its geometries and other spatial characteristics. This information supports identifying detected entities and is used in the inference process. The complexity of the required rules directly depends upon the complexity of the processed situation. In simple cases, even very simple rules are sufficient to produce a correct result. However, this concept also allows to handle more complex situations. A simple classification of an entity (*Geometry*) based on a SWRL rule annotates an electric pole (type 2), as found along railway tracks:

Geometry (?x) ^ hasHeight(?x, ?ht) ^ swrlb:greaterThan(?ht, 4) ^ swrlb:lessThan(?ht, 6)
→ ElectricPole2(?x) (3)

The use of spatial relations (Metric, Topologic, and Directional) between the detected entities is one possible extension of such simple geometry (Ben Hmida et al. 2012). It only requires the appropriate algorithms and then provides the result for the topological operation. Zlatanova et al. (2002) gives a survey of different 3D models and relations. The spatial operators available for a spatial query language consist of 3D topological operators (Borrmann & Rank 2008), 3D metric operators (Borrmann et al. 2009), 3D directional operators (Borrmann & Rank 2009) and finally 3D Boolean operators (Borrmann et al. 2006). In a simplified example, the following rule specifies that a "Building" that overlaps a "Railway" (both defined in the ontology), is a "RailwayStation".

Building(?b) ^ Railway(?r) ^ topo: overlaps(?b, ?r) → RailwayStation(?b) (4)

Fig. 5 shows our process guided by various knowledge domains in object detection and classification. In this figure, object classes are referred to as A, B, C, D, and E. We recall here that the process iterates until convergence, i.e. all objects are labelled, or stopping conditions, i.e. maximum number of iterations without refinement, are met.

6 Case Study

Two case studies illustrating our approach are presented in this section: Deutsche Bahn (DB) and Frankfurt Airport (Fraport). The goal in both cases was to detect and check relevant objects inside a defined work area.

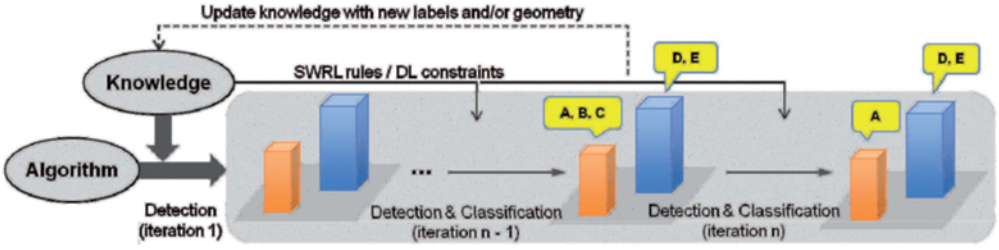

Fig. 5: Knowledge-driven method for object detection and classification process.

6.1 *Object Classification in the Railway System (DB)*

In the DB example, we used scans in the vicinity of the tracks. Data were captured from LIMEZ III, a surveying train equipped with a laser scanner mounted at its front-end. Two non-domain experts worked for approximately 20 days to build the DB example ontology. They were supported by experts of the German railway (DB). The available knowledge is used to classify the entities as:

- *Identified*: as soon as a feature value is in the range of a class. This annotation has to be supported by subsequent classifications and remains valid as long as no conflict is detected.
- *Ambiguous*: as soon as a feature value satisfies more than one class. Both annotations are stored and have to be separated by subsequent classifications and remain doubtful as long as no separation is possible.
- *Unknown*: indicates that a feature value does not match any existing class. Further processing requires the ASM to select other properties in order to continue the process.

Although a simple example, this nevertheless shows the general logic, which can then be further extended with other considerations among entities. Success is directly related to the ability to detect entities and the significance of the feature values chosen. Less characteristic features can also be used. However, these will require more iterations and additional rules in order to achieve a stable classification.

The aspect of quality can also be incorporated into the concept. This may either be realized by thresholds modelling data noise or by changing the strategy of selecting a path through the graph. The latter case handles situations in which features are sensitive to noise and corresponding algorithms might fail. For instance, an electric pole (type 2) is represented by parallel vertical supports. ASM searches and selects the relevant algorithm – *CheckParallel* – from the algorithmic library. This library is described by a graph (see Fig. 6) representing all allowed connections, based on input and output between algorithms. Based on some data quality thresholds, the sequence may or may not include pre-processing algorithms (e.g. *NoiseReduction*). On the path from the starting algorithm (in this case, *PositionDetection*) to the desired algorithm (*CheckParallel*), ASM infers and invokes all concerned algorithms based on the *hasInput/hasOutput* property. *Segmentation*, *NoiseReduction* and *LineDetection1* are the selected ones. Afterwards, ASM links them together to create a proper sequence: it then looks as follows (result illustrated in Fig. 7c):

PositionDetection → *Segmentation* → *NoiseReduction* → *LineDetection1* → *CheckParallel*.

The execution of this sequence provides a list of recognized object entities, which then

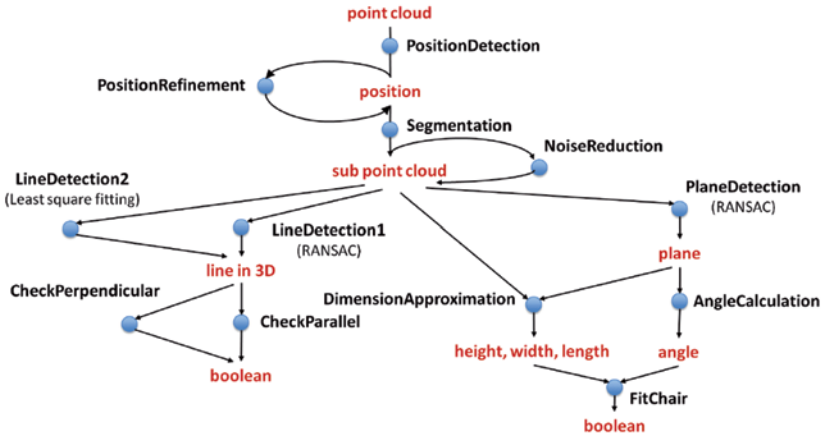

Fig. 6: Graph of possible algorithmic paths generated by ASM and used for detecting objects in both DB and Fraport cases.

are classified. Further sequences are used to improve the quality and to reduce the ambiguity within the results (Fig. 7d). Iterations are repeated until a complete annotation for all entities is performed. The convergence conditions are applied to terminate the detection process for entities.

We have processed a 500 m section along the railway. Out of 12 algorithms modelled in the KB (Fig. 6), the following ones were used by the system to classify objects (Tab. 1): *PositionDetection*, *Segmentation* (cropping points surrounding a given position), *DimensionApproximation*, *NoiseReduction*, *LineDetection1* (using RANSAC) and *AngleCalculation*. Knowledge was collected carefully in order to provide a reliable KB related to objects, scene, the nature of the data, algorithms and relationships between them. The base was progressively extended with new knowledge gained either from the analysis of the detected geometries or from classification results. Initially, 17 classes were defined as subclasses of the 5 classes in Tab. 1. These classes represent different types of signals and electric poles that can be found along the tracks and are of interest to our study. A total of approximately 500 geometries such as 3D line segments, angles and points of interest were recognized, 10 SWRL rules are used and 63 entities (possible object positions) were identified after the initialization step shown in (Fig. 7b). All entities include possible objects in the scene but also noise and objects of no interest. The true number of railway objects was 13 (Tab. 2). With the second iteration, the process tries to refine the results and classify the objects. At the end, 10 out of 13 real railway objects were correctly classified, 50 entities which represent non-railway objects were classified as *unknown*, and 3 railway objects could not be unambiguously classified with the rules implemented. The results in Fig. 7d were obtained by our software system. Computation took about 10 minutes on an Intel Xeon 2.4 GHz with 12G RAM. Note that our software is a prototype and has not been optimized for performance. In our experiments, we used the "shortest path" criterion from starting the algorithm to the desired algorithm in order to find the optimal algorithm sequence. Our system assumes equal weights for all edges in the algorithms graph, i.e. factors that are intrinsic to algorithms such as time and memory requirements are not taken into account at this stage. Results can be improved by applying more complex rules, possibly using additional geometric constraints such as line or plane orientation, angle between lines or number of lines expressed in the rule (5):

Tab. 1: Classes and properties used in DB scenario.

Class	Object properties
Electric pole (type 1)	Vertical structure, height, perpendicular lines
Electric pole (type 2)	Vertical structure, height, parallel lines
Electric pole (type 3)	Vertical structure, height, oblique line
Main signal (mechanical)	Vertical structure, height, perpendicular lines, parallel line, number of lines
Main signal (light)	Vertical structure, height, perpendicular lines, parallel line, oblique line, number of lines

$$\begin{aligned} &Geometry(?x) \wedge hasLine(?x, ?l) \wedge line(?l) \wedge \\ &DistanceSignal\ (?y) \wedge DistanceFrom(?x, ?y, \\ &?dis) \wedge swrlb:GreaterThan\ (?dis,1000) \wedge \\ &hasHeight(?x, ?h) \wedge swrlb:GreaterThan \\ &(?h, 4) \wedge hasVerticalLineNumber(?x, ?vn) \\ &\wedge swrlb:lessThanOrEqual(?vn, 2) \wedge \\ &hasObliqueLineNumber(?x, ?on) \wedge \\ &swrlb:equal(?on, 0) \rightarrow MainSignal(?x) \end{aligned} \quad (5)$$

In order to relate the classification to human interpretation the point cloud was presented to test persons. They identified 8 of 13 railway objects based on a visual inspection of the cloud and without taking into account topological or descriptive knowledge. This just shows the limited representation of objects inside such types of point clouds. One major reason for the poor quality of the point cloud is the fact that only the side of the object facing the tracks is captured due to the scanner on the train. However, this also shows the usefulness of additional knowledge.

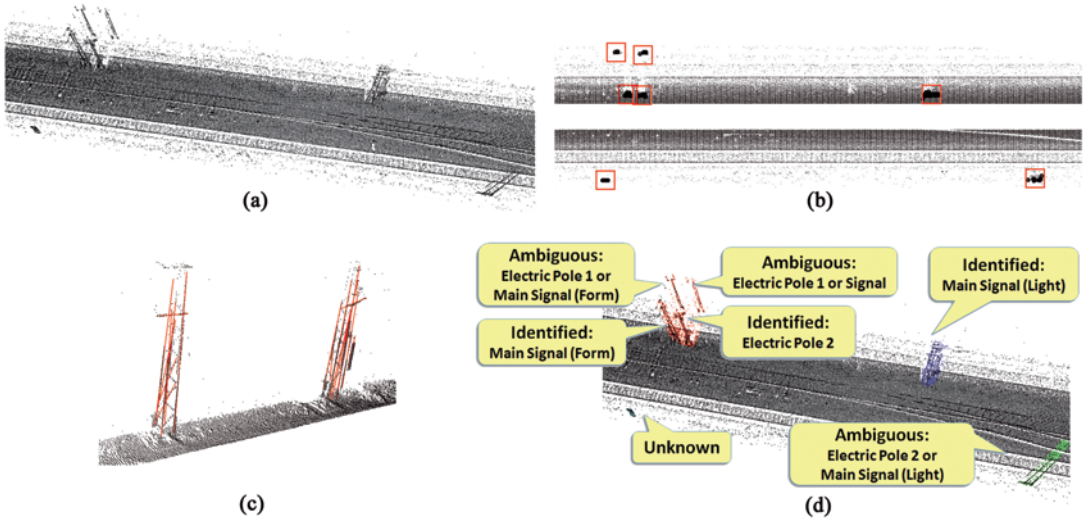

Fig. 7: (a) Point cloud representation of a section of a railway; (b) Results after executing the initialization step, projecting the point cloud to the ground plane, rectangles denote possible object positions; (c) Results from detecting 3D lines of a signal and electric pole (type 3) along the railway; (d) Positions of objects and annotation results after the first iteration.

Tab. 2: Experiment in a section of DB railway, comparison result between two approaches: Visual inspection using the standard software tool of DB, and knowledge-based data processing.

Object	Visual inspection	Knowledge-based data processing
Electric pole (type 1)	1/1*	1/1
Electric pole (type 2)	2/4	4/4
Electric pole (type 3)	1/1	1/1
Main signal (mechanical)	2/4	2/4
Main signal (light)	2/3	2/3
Total	8/13 (61.53 %)	10/13 (76.92 %)
(*) Number of detected objects over number of ground-truth objects.		

Results obtained after the processing along the tracks are shown in Tab. 2. Remarkable to see that the only failures using knowledge were Main Signals (light) that could also not be recognized by visual inspection. This is mainly caused by the poor quality of the data, especially in terms of point density, which made such structures hardly visible and undistinguishable. Some objects, the type 2 electric poles, were successfully identified using the automated detection and classification whereas visual inspection failed.

6.2 *Object Detection inside Airport Building (Fraport's Waiting Area)*

In the second case, we used scans from an environment inside the airport buildings, typically a waiting area. Changes in the technical infrastructure were of main interest. Data were obtained from classical terrestrial laser scanning. The Fraport scenario is different from the DB test example because a data base of expected objects in the scene exists and can be used as a-priori knowledge. Two persons worked for about 10 days to fill the ontology with knowledge such as properties of

Tab. 3: Classes and properties used in the Fraport scenario.

Class	Object properties
Wall	Vertical plane, length, height
Separation panel	Vertical plane, length, height
Advertising panel	Vertical plane, length, height, number of planes
Chair	Horizontal plane, leaning plane, angle between planes, length of chair

objects, scene, nature of data and characteristics of buildings. The data sources were CAD plans, related documents from the experts and observations from the real scene. The process first attempted to validate the presence of static objects such as walls, and separation or advertising panels in the point cloud that were supposed to exist according to the data base (Tab. 3). After that, moveable objects like chairs, trash bins, were detected and also fed into the KB. The initialization was different from the DB case because of more complex objects and the prominent role of many vertical planes. Therefore, we first detected vertical planes (Fig. 8a, b). This was possible by a vertical projection of the point cloud followed by Hough Line detection to locate the static objects' position on the ground plane. *VerticalProjection* and *HoughLineDetection* are included in *PositionDetection* algorithm. Points with a vertical projection in the vicinity of these lines were used to define segments corresponding to vertical planes. The following step was used to verify walls, separation panels or advertising panels defined in the data base based on their particular length and height (Fig. 8e). However, there are also many moveable objects like chairs, tables, counters, or trash bins, which also need to be detected to update the KB. All objects already available from the first validation phase gave a geometric and semantic frame helping to support the detection of unknown moveable objects. For example, chairs were searched for in a specific area defined within a certain distance from the wall (5 m in our experiments) and 0.7 m above the floor. Note that the reference frame of our point cloud is attached to the floor such that the latter is simply determined by fitting a horizontal plane (initialized at height Z = 0) using the *PlaneDetection* algorithm. We focussed on detecting walls in the border region of the check-in area. The static structures obtained

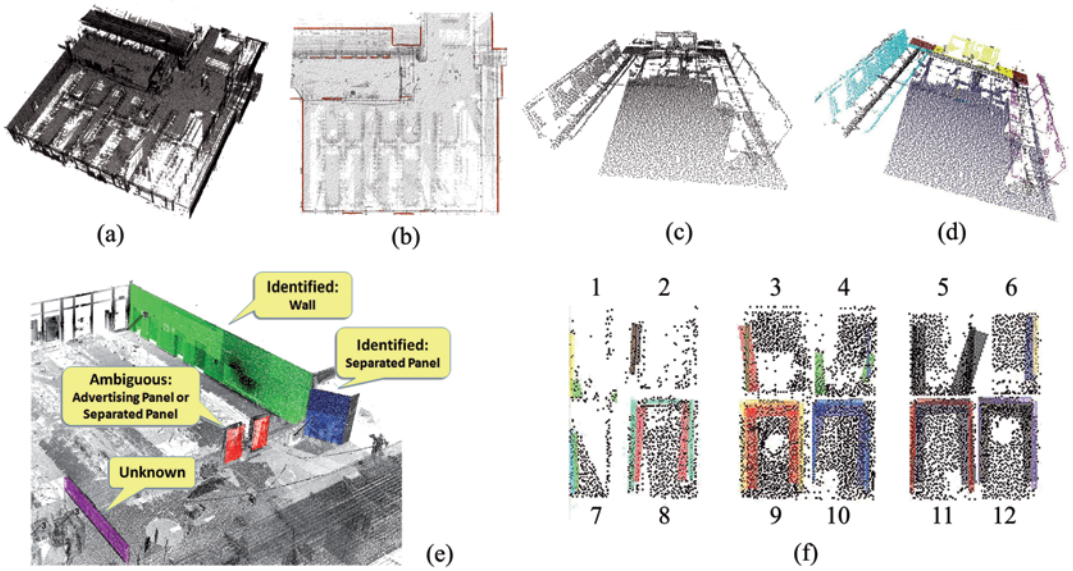

Fig. 8: Fraport scenario: (a) 3D scan of a check-in area, (b) detected walls, (c) point cloud exhibiting chairs, (d) detection results of a chair set, (e) annotated static objects, (f) identification results obtained on 12 chair sets in a waiting area (failures 1–2, partial detection 3–7, successful identification 8–12).

from the point cloud are shown in Fig. 8e. Only two walls exist in the scene and the remaining larger static structures are either separation or advertising panels, which are easily distinguishable from walls by their height. Both walls were successfully identified.

After the walls were detected, ASM generated, based on the properties of a chair, i.e. chair's length, horizontal plane, leaning plane, angle between two planes, an appropriate sequence of algorithms to invoke:

PositionDetection → *Segmentation* → *PlaneDetection* → *DimensionApproximation* → *AngleCalculation* → *FitChair*

FitChair is used to combine the detected geometries of a chair as depicted in Fig. 8d, f. A rule is also applied to classify chairs:

$$\begin{aligned} &Geometry(?x) \wedge hasCorrespondingGeo(?x, ?l) \\ &\wedge LeaningPlane(?l) \wedge \\ &hasCorrespondingGeo(?x, ?s) \\ &\wedge HorizontalPlane(?s) \wedge \\ &hasAngle(?x, 120) \wedge hasLength(?x, ?len) \\ &\wedge swrlb{:}greaterThan(?len, 370) \wedge \\ &swrlb{:}lessThan(?len, 380) \rightarrow Chair(?x) \end{aligned} \quad (6)$$

Chair sets are arranged parallel to the walls and represented by very sparse point clouds (Fig. 8c). Nevertheless, it is possible to detect, model and identify chair sets based on a sequence of algorithms making use of topological and geometrical constraints arising from previously detected elements. Six algorithms were used (out of the 12 in Fig. 6) such as: *PositionDetection*, *Segmentation*, *DimensionApproximation*, *PlaneDetection* (based on RANSAC), *AngleCalculation* and *FitChair* (which verifies a chair by two connected planes in an angle of 120°).

The results obtained are shown in Fig. 8f in which the five chair sets 8-12 were successfully identified, the five chair sets 3–7 were only partly detected and the two chair sets "1" and "2" could not be identified due to missing points. In the next stage of processing, objects were verified using topological constraints, such as a distance-based identification from the identified objects. Finally, 10 out of 12 chair sets could be correctly classified even in an insufficient dataset. The results reported here were obtained with an ontology that had been filled with approximately 350 detected geometries (planes, line segments…) and used 4 SWRL rules. The process took about 7 minutes on an Intel Xeon 2.4 GHz with 12G RAM when using our prototype software. The full process of detecting chair sets including wall identification is depicted in Fig. 9.

7 Conclusion

This paper presents a knowledge-driven approach to detect objects in point clouds. It is based on the semantics of different associated domains which assist in detecting and classifying objects. Knowledge supports all processing steps including the arrangement of the data processing. This allows inter-relating the characteristics of algorithms with those of the objects in the domain of the application. Our system also provides the flexibility to infer the strategy from existing knowledge, and to adapt the processing to the application-specific requirements. The permanent interaction between the algorithms and the KB allows for a smooth and gradual construction of the KB which contains at the end of the process all entities which can be detected and identified. Admittedly, it takes time to collect the knowledge at the beginning. However, it has only to be collected once and is later always available

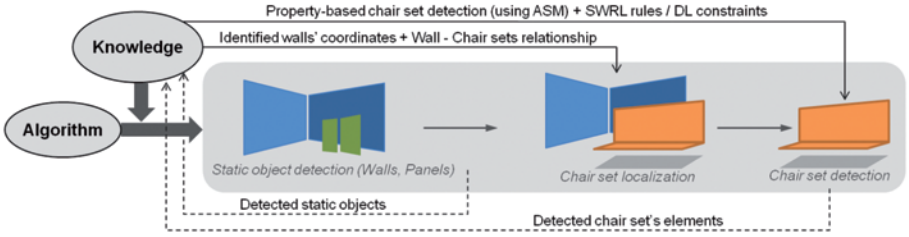

Fig. 9: Chair set detection process.

when needed. In addition, the KB can be iteratively extended by the operator at many practical waypoints. The quality of results depends on the robustness of the implemented algorithms, the selected strategy and the amount of knowledge integrated. In practice, the solution is oriented towards the requirements of a specific application. Further development is needed to make algorithms more robust to quality variations in the data, and to segment more complex objects. Furthermore, the knowledge sources (data features, object properties and scene characteristics) have to be extended in order to enhance the classification processing, especially regarding ambiguous cases. Lastly, both an expansion of the ontology and further implementation and testing of rules are currently considered and subject to investigation.

Acknowledgements

The work presented in this paper is part of the research project WiDOP – Wissensbasierte Detektion von Objekten in Punktwolken für Anwendungen im Ingenieurbereich, funded by the German Federal Ministry for Research and Education (grant no. 1758X09). Project partners are Metronom Automation GmbH, DB Netz AG (railway) and Fraport AG (facility management).

References

Anguelov, D., Taskarf, B., Chatalbashev, V., Koller, D., Gupta, D., Heitz, G. & Ng, A., 2005: Discriminative learning of markov random fields for segmentation of 3d scan data. – Computer Vision and Pattern Recognition (CVPR) **2:** 169–176.

Bechhofer, S., Van Harmelen, F., Hendler, J., Horrocks, I., McGuinness, D.L., Patel-Schneider, P.F. & Stein, L.A., 2004: OWL web ontology language reference. – W3C recommendation 10.

Ben Hmida, H., Cruz, C., Nicolle, C. & Boochs, F., 2011: From 3D Point Clouds To Semantic Objects An Ontology-Based Detection Approach. – International Conference on Knowledge Engineering and Ontology Development, Paris, France.

Ben Hmida, H., Cruz, C., Nicolle, C. & Boochs, F., 2012: From Quantitative Spatial Operator to Qualitative Spatial Relation Using Constructive Solid Geometry, Logic Rules and Optimized 9-IM Model. – International conference on computer sciences and automation engineering **2:** 453–458, Zhanjiajie China.

Borrmann, A., Van Treeck, C. & Rank, E., 2006: Towards a 3D spatial query language for building information models. – Computing and Decision Making in Civil and Building Engineering.

Borrmann, A. & Rank, E., 2008: Topological operators in a 3D spatial query language for building information models. – Conference on Computing in Civil and Building Engineering.

Borrmann, A. & Rank, E., 2009: Specification and implementation of directional operators in a 3D spatial query language for building information models. – Advanced Engineering Informatics **23:** 32–44.

Borrmann, A., Schraufstetter, S. & Rank, E., 2009: Implementing metric operators of a spatial query language for 3D building models: octree and B-Rep approaches. – Journal of Computing in Civil Engineering **23** (1): 34–46.

Busch, A., Gerke, M., Grünreich, D., Heipke, C., Liedtke, C. & Müller, S., 2005: Automatisierte Verifikation topographischer Geoinformation unter Nutzung optischer Fernerkundungsdaten. – PFG – Photogrammetrie, Fernerkundung, Geoinformation **2:** 111–122.

Cantzler, H., Fisher, R. & Devy, M., 2002: Quality enhancement of reconstructed 3D models using coplanarity and constraints. – Pattern Recognition: 34–41.

Dijkstra, E.W., 1959: A Note on Two Problems in Connexion with Graphs. – Numerische Mathematik **1:** 269–271.

Durand, N., Derivaux, S., Forestier, G., Wemmert, C., Gancarski, P., Boussaid, O. & Puissant A., 2007: Ontology-based Object Recognition for Remote Sensing Image Interpretation. – Tools with Artificial Intelligence (ICTAI 2007): 472–479.

Green, P.J., 1995: Reversible jump Markov chain Monte Carlo computation and Bayesian model determination. – Biometrika **82** (4): 711–732.

Growe, S. & Tonjes, R., 1997: A knowledge based approach to automatic image registration. – International Conference on Image Processing **3:** 228–231.

Hedau, V., Hoiem, D. & Forsyth, D., 2010: Thinking Inside the Box: Using Appearance Models and Context Based on Room Geometry. – The European Conference on Computer Vision (ECCV): 224–237.

Helmholz, P., Becker, C., Breitkopf, U., Büschenfeld, T., Busch, A., Braun, C., Grünreich, D., Heipke, C., Müller, S., Ostermann, J., Pahl, M.,

Rottensteiner, F., Vogt, K. & Ziems, M., 2012: Semi-Automatic Quality Control of Topographic Datasets. – Photogrammetric Engineering & Remote Sensing **78** (9): 959–972.

Huang, H., Brenner, C. & Sester, M., 2011: 3D building roof reconstruction from point clouds via generative models. – International Conference on Advances in Geographic Information Systems: 16–24.

Horrocks, I., Patel-Schneider, P.F., Boley, H., Tabet, S., Grosof, B. & Dean, M., 2004: SWRL: A semantic web rule language combining OWL and RuleML. – W3C Member submission **21:** 79.

Maillot, N. & Thonnat, M., 2008: Ontology Based Complex Object Recognition. – Image and Vision Computing (IVC) **26** (1): 102–113.

Matsuyama, T., 1987: Knowledge-based aerial image understanding systems and expert systems for image processing. – Geoscience and Remote Sensing **3:** 305–316.

Nurunnabi, A., Belton, D. & West, G., 2012: Diagnostic-robust statistical analysis for local surface fitting in 3D point cloud data. – ISPRS Annals of the Photogrammetry, Remote Sensing and Spatial Information Sciences **I-3**, Melbourne, Australia.

Pu, S. & Vosselman, G., 2006: Automatic extraction of building features from terrestrial laser scanning. – International Archives of Photogrammetry, Remote Sensing and Spatial Information Sciences **36:** 25–27.

Pu, S. & Vosselman, G., 2009: Knowledge based reconstruction of building models from terrestrial laser scanning data. – Journal of Photogrammetry and Remote Sensing **64** (6): 575–584.

Ripperda, N. & Brenner, C., 2006: Reconstruction of Facade Structures Using a Formal Grammar and RjMCMC. – The **28th** conference on Pattern Recognition: 750–759.

Rost, U. & Münkel, H., 1998: Knowledge based configuration of image processing algorithms. – International Conference on Computational Intelligence & Multimedia Applications.

Scholze, S., Moons, T. & Van Gool, L., 2002: A probabilistic approach to building roof reconstruction using semantic labelling. – Pattern Recognition: 257–264.

Tang, Y., Lee, S.W. & Suen, C., 1996: Automatic document processing: A survey. – Pattern Recognition **29** (12): 1931–1952.

Tarsha-Kurdi, F., Landes, T., Grussenmeyer, P. & Koehl, M., 2007: Model-driven and data-driven approaches using LIDAR data: analysis and comparison. – International Archives of Photogrammetry, Remote Sensing and Spatial Information Systems: 87–92.

Teboul, O., Simon, L., Koutsourakis, P. & Paragios, N., 2010: Segmentation of Building Facades Using Procedural Shape Priors. – Computer Vision and Pattern Recognition: 3105–3112.

Trinder, J.C. & Wang, Y., 1998: Knowledge-based road interpretation in aerial images. – International Archives of Photogrammetry and Remote Sensing **32:** 635–640.

Vosselman, G. & Dijkman, S., 2001: 3D building model reconstruction from point clouds and ground plans. – International Archives of Photogrammetry Remote Sensing and Spatial Information Sciences, **34** (3/W4): 37–44, Athens, Georgia, USA.

Zlatanova, S., Rahman, A. & Shi, W., 2002: Topology for 3D spatial objects. – International Symposium and Exhibition on Geoinformation: 22–24.

Addresses of the Authors:

M.Sc. Hung Truong & M.Sc. Helmi Ben Hmida, University of Applied Sciences Mainz und University of Burgundy, e-mail: {truong}{helmi.benhmida}@geoinform.fh-mainz.de und {quoc-hung.truong}{helmi.benhmida}@u-bourgogne.fr

Prof. Dr. Frank Boochs, i3mainz, University of Applied Sciences Mainz, Lucy-Hillebrand-Str. 2, 55128 Mainz, Tel.: +49-6131-628-1489, Fax: +49-6131-628-91489, e-mail: frank.boochs@geoinform.fh-mainz.de

Prof. Dr. Adlane Habed, Prof. Dr. Christophe Cruz, Prof. Dr. Yvon Voisin & Prof. Dr. Christophe Nicolle, University of Burgundy, Le2i, Route des Plaines de l'Yonne, BP 16, 89010 Auxerre cedex, France, Tel.: +33-3-86-49-28-51, Fax: +33-3-86-49-28-50, e-mail: {adlane.habed}{christophe.cruz}{yvon.voisin}{christophe.nicolle}@u-bourgogne.fr

Manuskript eingereicht: März 2012
Angenommen: März 2013

Hochschulnachrichten

Fachhochschule Mainz, Akademiepreis des Landes Rheinland-Pfalz für Prof. Frank Boochs

Prof. Dr.-Ing. Frank Boochs von der Lehreinheit Geoinformatik und Vermessung der FH Mainz ist im November 2012 mit dem Akademiepreises des Landes Rheinland-Pfalz ausgezeichnet worden. Mit dem Preis werden Persönlichkeiten von Hochschulen geehrt, die herausragende und vorbildhafte Leistungen in Lehre und Forschung erbracht und maßgebend den wissenschaftlichen Nachwuchs gefördert haben.

Frank Boochs ist seit 1993 Professor für Angewandte Informatik an FH Mainz. Er ist Mitbegründer des seit 1998 bestehenden i3mainz – Institut für Raumbezogene Informations- und Messtechnik an der FH Mainz. Seit 2002 ist er Geschäftsführender Leiter des i3mainz.

Der Akademiepreis wird seit 2001 vom Land Rheinland-Pfalz in Kooperation mit der Akademie der Wissenschaften und der Literatur Mainz vergeben. Den Vorsitz der Jury hatte Prof. Dr. Peter Strohschneider, der seit dem 1. Januar 2013 auch Präsident der Deutschen Forschungsgemeinschaft ist. Die Jury lobte die große Bandbreite von Boochs Forschungsarbeit, die sich mit Projekten sowohl in der Industrie und Logistik als auch in Archäologie und Denkmalschutz beschäftigt. Dazu ist seine Arbeit sehr international ausgerichtet. Im November 2012 startete beispielsweise das von ihm initiierte EU-Projekt COSCH, bei dem es um den optimierten Einsatz von Messtechnik für die Dokumentation von Bauwerken und Kunstgegenständen geht und an dem sich mehr als 90 Wissenschaftler aus 21 Ländern beteiligen. Seine Kollegen betonten Boochs Fähigkeiten als Hochschullehrer. Es gelänge ihm, „die jungen Menschen für komplexe wissenschaftliche, bisweilen abstrakte Inhalte zu begeistern."

Der Akademiepreis ist mit 25.000 Euro dotiert, die der Preisträger für Forschung und Lehre einsetzen kann.

Persönliches

Nachruf auf Otto Hofmann, Ehrenmitglied der DGPF

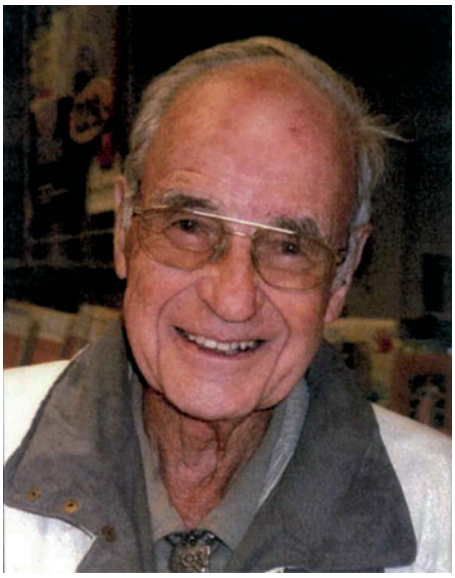

Am 17.1.2013 starb Dr.-Ing. Otto Hofmann, seit 2002 Ehrenmitglied der Deutschen Gesellschaft für Photogrammetrie, Fernerkundung und Geoinformation, im gesegneten Alter von 90 Jahren in seiner Heimatstadt Brunnthal bei München. Hofmanns große Verdienste um die Photogrammetrie wurden in dieser Zeitschrift anlässlich seines 65. und seines 80. Geburtstags von Heinrich Ebner ausführlich gewürdigt (BuL 5/1987 und PFG 3/2002).

Hofmann wurde am 11. Juli 1922 in Dippoldiswalde im Erzgebirge geboren. Nach dem Studium des Vermessungswesens in Dresden begann er eine Tätigkeit beim VEB Carl Zeiss

DOI: 10.1127/1432-8364/2013/0173 1432-8364/13/0173 $ 2.00

Jena, während der er 1957 an der TU Dresden promovierte. Nach der Übersiedlung in die Bundesrepublik und einer kurzen Selbständigkeit kam Hofmann 1965 zu Bölkow, später MBB in Ottobrunn bei München, wo er bis zu seiner Pensionierung 1987 die Geschicke der digitalen Photogrammetrie maßgeblich beeinflusste. Dies geschah zu einem Zeitpunkt, als die Luftbildphotogrammetrie noch ausschließlich mit analogen Bildern arbeitete. Sein Name ist vor allem mit der 3-Zeilengeometrie und den zugehörigen Kameraentwicklungen MOMS-01, MOMS-02/D2 und DPA verknüpft.

Auch im hohen Alter war Hofmann noch beruflich aktiv. Sein brillanter Vortrag auf der Photogrammetrischen Woche 2005 zum Thema *Calibration and Georeferencing of Aerial Digital Cameras* wird vielen Zuhörern noch in Erinnerung sein. Für mich war der Vortrag Anlass, den fachlichen Kontakt zu Hofmann zu suchen. Ich war von seinen Vorstellungen begeistert und wollte sehen, was sich damit anfangen ließe. In einem zweijährigen Forschungsprojekt stellte sich sehr schnell heraus, dass Hofmann seine Ideen bereits in mathematische Gleichungen übertragen hatte, so dass wir unverzüglich mit der Umsetzung beginnen konnten. Unser Kontakt war geprägt von seinem umfangreichen Wissen über verschiedenste Aspekte der Photogrammetrie und seiner ausgeprägten Freude am wissenschaftlichen Arbeiten, das immer an bewährten Ansätzen anknüpfte und zielorientiert neue praxistaugliche Lösungen suchte. Otto Hofmann hat mich in diesen Diskussionen tief beeindruckt und mich immer wieder vergessen lassen, dass mir ein hochbetagter Herr von weit über 80 Jahren gegenüber saß.

Mit Otto Hofmann verliert die deutsche Photogrammetrie einen ihrer profiliertesten Vertreter, der die digitale Photogrammetrie entscheidend geprägt hat. Er hat in seinen Arbeiten immer wieder Neuland betreten und war seiner Zeit in Vielem weit voraus. Die deutsche Photogrammetrie wird ihm ein ehrendes Andenken bewahren.

Christian Heipke, Hannover

Nachruf auf Ákos Detreköi

Am 18.12.2012 verstarb im 74. Lebensjahr Prof. Dr. Ákos Detreköi, Professor Emeritus, Altrektor der Technischen und Wirtschaftswissenschaftlichen Universität Budapest (Budapesti Müszaki és Gazdaságtudományi Egyetem – BME).

Ákos Detreköi wurde am 27.11.1939 in Budapest (Ungarn) geboren. Seine Laufbahn in Forschung und Lehre begann Detreköi 1963 am Lehrstuhl für Vermessungskunde der BME. Sein Interesse konzentrierte sich vorerst auf die Ingenieurgeodäsie. Um auch die Praxis kennenzulernen, arbeitete er von 1964 – 1965 im VEB Ingenieurvermessungswesen Dresden. Nach seiner Rückkehr bekam er in der Lehre in den Fächern Instrumentenkunde und Ingenieurgeodäsie neue Aufgaben in der Ausgleichungsrechnung am Lehrstuhl für Höhere Geodäsie.

Daneben hat Detreköi sein Interesse für die Ingenieurgeodäsie nicht vernachlässigt. Seine Erfahrungen in Absteckungen und Deformationsmessungen zusammen mit seinen Kenntnissen in der Ausgleichungsrechnung führten 1967 zu seiner Promotion zum Thema „Untersuchungen der Genauigkeit von Absteckungen“. Weitere Forschungen zu Deformationsbeobachtungen folgten, um schließlich in sei-

ne zusammenfassende Arbeit „Entwurf, Aufarbeitung und Analyse von ingenieurgeodätischen Deformationsmessungen“ einzumünden.

Nach seiner Berufung 1980 zum Ordinarius auf den Lehrstuhl für Photogrammetrie und Fernerkundung kamen zu seinen ursprünglichen Arbeitsgebieten noch Fernerkundung und Geoinformationssysteme hinzu. So erschienen zusammen mit György Szabó 1995 und 2002 zwei grundlegende Werke zur Rauminformatik.

Als Humboldt-Stipendiat hielt sich Ákos Detreköi zu Studienaufenthalten an den Universitäten Bonn, Karlsruhe, München und Stuttgart auf und pflegte in der Folgezeit intensive Kontakte. Besonders enge Zusammenarbeit ergab sich mit Karl Kraus, Lehrstuhl für Photogrammetrie der TU Wien. 1994 wurde Detreköi zum Vorsitzenden, 1997 zum Vorsitzenden Ehrenhalber des Vereins der Ungarischen Humboldt Stipendiaten gewählt.

Detreköi war Verfasser von 3 Büchern (eines davon in zwei Auflagen) und mehr als 170 Veröffentlichungen in verschiedenen Fachzeitschriften in ungarischer, deutscher und englischer Sprache. Er war Mitglied im Beirat der Fachzeitschriften „Geodézia és Kartográfia“ und „Acta Geodetica et Geophysica”. Weiter beteiligte er sich aktiv an der Herausgabe der „Zeitschrift für Photogrammetrie“.

Ákos Detreköi liebte es, in Gesellschaft zu sein und sorgte dabei stets für Humor. Sein hohes Fachwissen betraf nicht allein die Geodäsie in ihren zahlreichen Teilbereichen. Er wusste sich auch in Kunst und Literatur auf hohem Niveau zu bewegen. Sein persönlicher Einsatz und seine unermüdliche Unterstützung galten dem wissenschaftlichen Nachwuchs. Zahlreiche junge Kollegen konnten von seinem Wissen und seiner positiven Art zu denken und zu handeln profitieren.

Die Gemeinschaft der Geodäten hat durch seinen Tod einen wissenschaftlich profilierten und persönlich allseits geschätzten Kollegen verloren.

József Ádám und Péter Biró, Budapest, Ungarn

Neuerscheinung

Fischer-Stabel, P. (Hrsg.) 2013: Umweltinformationssysteme, Grundlegende Konzepte und Anwendungen (2. neu bearbeitete Auflage). – Wichmann-Verlag, 364 Seiten. ISBN 978-3-87907-517-1.

Umweltinformationssysteme (UIS) der verschiedensten Dimensionen stellen heute wichtige Hilfsmittel dar, um angesichts der ständig wachsenden Anforderungen im Umweltbereich ein schnelles und qualifiziertes Handeln sicherzustellen. Mit Inkrafttreten der EG-Richtlinie zum Zugang zu Umweltinformationen und der damit verbundenen Erweiterung des Informationsanspruchs gegenüber den (Umwelt-)Verwaltungen sind UIS auch im Rahmen einer aktiven, systematischen Informationspflicht gegenüber der Öffentlichkeit gefordert.

Die Publikation ist ein interdisziplinär angelegtes Lehrbuch, dessen Inhalte die Konzeption und Entwicklung von Umweltinformationssystemen vermitteln. Sie wendet sich an Praktiker und Studierende der Fachgebiete Geoinformatik, Geowissenschaften, Informatik sowie dem Planungs- und Umweltbereich.

Veranstaltungskalender

2013

21.–23. April: **Joint Urban Remote Sensing Event (JURSE 2013)** in **São Paulo**, Brasilien. inpe.br/jurse2013/

30. April – 2. Mai: 8th **International Symposium on Mobile Mapping Technology** 2013 in **Tainan**, Taiwan. conf.ncku.edu.tw/mmt2013/

6.–7. Mai: **19. Workshop Computer-Bildanalyse in der Landwirtschaft / 2. Workshop Unbemannte autonom fliegende Systeme (UAS) in der Landwirtschaft,** Beuth Hochschule für Technik in **Berlin**. atb-potsdam.de/workshop-cba-uas.

6.–8. Mai: **Symposium Königslutter** 2013 der DGfK in **Königslutter am Elm**. angewandte-kartographie.de/

13.–16. Mai: **SPIE Optical Metrology** in **München** – ***Videometrics, Range Imaging and Applications XII***. spie.org/x6506.xml

21.–23. Mai: **IAPR Conference on Machine Vision Applications (MVA 2013)** in **Kyoto**, Japan. mva-org.jp/mva2013/

21.–24. Mai: **ISPRS Hannover-Workshop "High-Resolution Earth Imaging for Geospatial Information"** in **Hannover**. ipi.uni-hannover.de

3.–6. Juni: 33rd **EARSeL Symposium** in **Matera**, Italien. earsel.org/symposia/2013-symposium-Matera/

5.–7. Juni: **International Conference on Earth Observation for Global Changes (EOGC'2013)** in **Toronto**, Canada. eogc2013.blog.ryerson.ca/

19.–20. Juni: **Fachtagung Mobile Mapping** in **Mainz**. 3dgi.ch/mm2013/

23.–28. Juni: **Computer Vision and Pattern Recognition (CVPR 2013)** in **Portland**, Oregon, USA. pamitc.org/cvpr13/

2.–5. Juli: **GI_Forum 2013** in **Salzburg**, Österreich. gi-forum.org

14.–20. Juli: **International Computer Vision Summer School** in **Punta Sampieri**, Italien. svg.dmi.unict.it/icvss2013/

21.–26. Juli: **IGARSS 2013** in **Melbourne**, Australien. igarss2013.org/

25.–30. August: 26th **International Cartographic Conference (ICC)** in **Dresden**. icc2013.org/

2.–6. September: XXIVth **CIPA Heritage Documentation Symposium** in **Strasbourg**, Frankreich. cipa.icomos.org

4.–6. September: **UAV-g Workshop** in **Rostock**. uav-g.org

9.–13. September: 54. **Photogrammetrische Woche** in **Stuttgart**. ifp.uni-stuttgart.de/phowo

9.–13. September: **British Machine Vision Conference (BMCV 2013)** in **Bristol**, England. bmvc2013.bristol.ac.uk

15.–18. September: **International Conference on Image Processing (ICIP 2013)** in **Melbourne**, Australien. www.ieeeicip.org

12.–13. November: **CMRT2013**, City Models, Roads, and Traffic, in **Antalya**, Türkei. pf.bv.tum.de/isprs/cmrt13/

26.–29. November: **3D GeoInfo 2013** in **Istanbul**, Türkei. 3dgeoinfo.com

8.–15. Dezember: **ICCV 2013**, International Conference on Computer Vision, **Sydney**, Australien. iccv2013.org

10.–11. Dezember: **LowCost 3D** in **Berlin**. lc3d.net

2014

13.–14. Februar: **Oldenburger 3D Tage** in **Oldenburg**. jade-hs.de/fachbereiche/bauwesen-und-geoinformation/geoinformation/oldenburger-3d-tage/

Weitere Konferenzen und Workshops finden sich beispielsweise unter:
isprs.org/calendar/
iris.usc.edu/Information/Iris-Conferences.html

Korporative Mitglieder

Firmen

AEROWEST GmbH
AICON 3D Systems GmbH
aphos Leipzig AG
Becker GeoInfo GmbH
Bernhard Harzer Verlag GmbH
Blom Deutschland GmbH
Brockmann Consult GmbH
bsf swissphoto GmbH
Büro Immekus
CGI Systems GmbH
con terra GmbH
DB Netz AG
DELPHI IMM GmbH
Deutsches Bergbau-Museum
EFTAS Fernerkundung Technologietransfer GmbH
ESG Elektroniksystem- und Logistik-GmbH
Esri Deutschland GmbH
EUROPEAN SPACE IMAGING
Eurosense GmbH
fokus GmbH
g.on experience gmbh
GAF GmbH
GeoCart Herten GmbH
GeoContent GmbH
Geoinform. & Photogr. Engin. Dr. Kruck & Co. GbR
geoplana Ingenieurgesellschaft mbH
GEOSYSTEMS GmbH
GGS - Büro für Geotechnik, Geoinformatik, Service
Hansa Luftbild AG
IGI - Ingenieur-Gesellschaft für Interfaces mbH
ILV Ingenieurbüro für Luftbildauswertung und Vermessung
Imetric 3D GmbH
Infoterra GmbH
INVERS - Industrievermessung & Systeme
ITT Visual Information Solutions Germany
J. Linsinger ZT-GmbH
Jena-Optronik GmbH
Leica Geosystems GmbH
Luftbilddatenbank-Würzburg
Messbildstelle GmbH
Microsoft Photogrammetry
MILAN Geoservice GmbH
M.O.S.S. Computer Grafik Systeme GmbH
PHOENICS GmbH
PMS - Photo Mess Systeme AG
RIEGL Laser Measurement Systems GmbH
RWE Power AG, Geobasisdaten/Markscheidewesen
technet GmbH
TRIGIS Vermessung + Geoinformatik GmbH
Trimble Germany GmbH
trimetric 3D Service GmbH
Wichmann, VDE Verlag GmbH
Z/I Imaging Ltd.

Behörden

Amt für Geoinformationswesen der Bundeswehr
Bayerische Landesanstalt für Wald und Forstwirtschaft
Bundesamt für Kartographie und Geodäsie
Bundesmininisterium für Ernährung, Landwirtschaft und Verbraucherschutz
Hessisches LA für Bodenmanagement und Geoinformation
Innenministerium NRW, Gruppe Vermessungswesen
Institut für Umwelt- und Zukunftsforschung
LA für Geoinformation und Landentwicklung, BW
LA für Vermessung und Geoinformation, Bayern
LB Geoinformation und Vermessung, Hamburg
LB für Küstenschutz, Nationalpark und Meeresschutz, SH
Landesvermessung und Geobasisinformation Niedersachsen
Märkischer Kreis, Vermessungs- und Katasteramt
Regierungspräsident Tübingen, Abt. 8 Forstdirektion
Regionalverband Ruhr
Staatsbetrieb Sachsenforst Pirna
Stadt Bocholt, Fachbereich 31
Stadt Düsseldorf, Vermessungs- und Katasteramt
Stadt Köln, Amt für Liegenschaften, Vermessung und Kataster
Stadt Wuppertal, Vermessung, Katasteramt und Geodaten
Thüringer LA für Vermessung und Geoinformation

Hochschulen

BTU Cottbus, Lehrstuhl für Vermessungskunde
FH Frankfurt a.M., FB 1, Studiengang Geoinformation
FH Mainz, Institut für Raumbezogene Informations- und Messtechnik
Jade Hochschule, Institut für Angewandte Photogrammetrie und Geoinformatik
HCU HafenCity Universität Hamburg, Geomatik
HfT Stuttgart, Vermessung und Geoinformatik

HS Bochum, FB Vermessung und Geoinformatik
HS Karlsruhe, Fakultät für Geomatik
HTW Dresden, FB Vermessungswesen/Kartographie
LUH Hannover, Institut für Kartographie und Geoinformatik
LUH Hannover, Institut für Photogrammetrie und Geoinformation
MLU Halle, FG Geofernerkundung
Ruhr-Uni Bochum, Geographisches Institut
RWTH Aachen, Geodätisches Institut
TU Bergak. Freiberg, Institut für Markscheidewesen und Geodäsie
TU Berlin, Computer Vision & Remote Sensing
TU Berlin, Institut für Geodäsie und Geoinformationstechnik
TU Braunschweig, Institut für Geodäsie und Photogrammetrie
TU Clausthal, Institut für Geotechnik und Markscheidewesen
TU Darmstadt, Institut für Photogrammetrie und Kartographie
TU Dresden, Institut für Photogrammetrie und Fernerkundung
TU München, FG Photogrammetrie und Fernerkundung
TU Wien, Institut für Photogrammetrie und Fernerkundung
Uni Bonn, Institut für Photogrammetrie
Uni Göttingen, Institut für Waldinventur und Waldwachstum
Uni Heidelberg, IWR Interdisziplinäres Zentrum für Wissenschaftliches Rechnen
Uni Kassel, FB Ökologische Agrarwissenschaften
Uni Kiel, Geographisches Institut
Uni Stuttgart, Institut für Photogrammetrie
Uni Würzburg, Geographisches Institut
Uni zu Köln, Geographisches Institut